Targeting Epsins by nanotherapy regulates lipid metabolism and promotes ABCG1-mediated cholesterol efflux to fortify atheroma regression

Kui Cui[1]†, Xinlei Gao[2]†, Beibei Wang[1]†, Hao Wu[1], Yunzhou Dong[1], Yuling Xiao[3], Xingya Jiang[3], Marina V. Malovichko[4], Kathryn Li[1], Siu-Lung Chan[1], Dan Shan[1], Qianman Peng[1], Yaowei Lu[1], Bo Zhu[1], Scott Wong[1], Douglas B. Cowan[1], MacRae Linton[5], Sanjay Srivastava[4], Jinjun Shi[3], Kaifu Chen[2*], Hong Chen[1*]

1. Vascular Biology Program, Boston Children's Hospital and Department of Surgery, Harvard Medical School; Boston, MA, 02115, USA.
2. Department of Cardiology, Boston Children's Hospital, Harvard Medical School; Boston, MA, 02115, USA.
3. Center for Nanomedicine and Department of Anesthesiology, Brigham and Women's Hospital, Harvard Medical School; Boston, MA, 02115, USA.
4. Division of Environmental Medicine, University of Louisville; Louisville, KY, 40292, USA.
5. Atherosclerosis Research Unit, Cardiovascular Medicine, Department of Medicine, Vanderbilt University Medical Center; Nashville, TN, 37232, USA.

†These authors contributed equally to this work.

*Corresponding authors. Email: hong.chen@childrens.harvard.edu

kaifu.chen@childrens.harvard.edu

Abstract: Resolving atheromas and hindering their transition into vulnerable atherosclerotic plaques is imperative to prevent deadly episodes such as heart attacks and strokes. Excess cholesterol accumulation in lesional macrophages switches on a complex inflammatory response in atherosclerosis. Despite the development of new cholesterol-lowering therapies, including of the recently approved PCSK9 small interfering RNA (siRNA) antagonists, patients still face a tremendous risk of developing major acute cardiovascular events resulting from chronic inflammation in the plaque. We previously showed that Epsins, a family of endocytic adaptors, fuel inflammation in atherosclerosis; however, the underlying mechanism and the therapeutic potential of targeting Epsins remains largely unknown. Here, we report that Epsins regulate lipid metabolism and transport in atherosclerotic macrophages, and that inhibiting Epsins by nanotherapy halts inflammation and accelerates atheroma resolution. Harnessing lesional macrophage-specific nanoparticle (NP) delivery of Epsin siRNAs, we show that silencing of macrophage Epsins markedly diminishes atherosclerotic plaque size and promotes plaque regression. Mechanistically, we demonstrate that Epsins bind to CD36 to facilitate lipid uptake by enhancing CD36 endocytosis and recycling. Conversely, Epsins promote ABCG1 degradation via lysosomes and hamper ABCG1-mediated cholesterol efflux and reverse cholesterol transport. In a myeloid-specific Epsin double knockout mouse model (LysM-DKO) with a genetic reduction in ABCG1 (LysM-DKO-ABCG1$^{fl/+}$), the enhanced cholesterol efflux and reverse transport due to Epsin deficiency was suppressed. Our findings suggest that targeting Epsins in lesional macrophages may offer therapeutic benefits in treating advanced atherosclerosis.

INTRODUCTION

Atherosclerosis is a complex and chronic condition that results in a buildup of fatty deposits, called plaques, inside the artery. Atherosclerosis is the root cause of coronary heart disease, ischemic stroke, and peripheral arterial disease (Libby, 2012; Weber and Noels, 2011). Despite effective lipid-lowering therapies including new drugs of antibody and siRNA drugs targeting PCSK9, atherosclerosis is still the leading cause of mortality worldwide. Atherosclerotic lesion formation involves interactions between oxidized low-density lipoprotein (oxLDL) and prominent constituents of the arterial wall including monocyte-derived macrophages, immune cells, and vascular smooth muscle cells (Glass and Witztum, 2001; Wang et al., 2020). Amounting evidence support that constituents with the potential to promote macrophage egress from the plaque such as regulatory T cells play a critical role in regulating macrophage pro-resolving functions during atherosclerosis regression (Moore et al., 2013; Sharma et al., 2020). Furthermore, the pro-inflammatory effects of oxLDL lead to endothelial activation and macrophage recruitment (Steinberg, 2009). Invading macrophages in the sub-endothelium ingest modified LDL and transform into lipid-laden foam cells (Glass and Witztum, 2001; Libby, 2012). This escalates arterial inflammation—a prime contributor to the transition from a stable to vulnerable atheroma (Alsheikh-Ali et al., 2010; Doring, 2015; Hansson et al., 2015; Virmani et al., 2006). Accordingly, patients that receive a therapeutic cocktail aimed at alleviating dyslipidemia and hypertension still develop deleterious cardiovascular diseases (Charo and Taub, 2011; Weber and Noels, 2011). This accentuates the urgent need for next-generation therapies geared toward eradicating inflammation in the arterial wall.

Epsins are a family of highly-conserved endocytic adaptor proteins that associate with the plasma membrane through interactions between their N-terminal homology (ENTH) domain and

69 membrane PI (4,5) P2 (De Camilli et al., 2002; Itoh et al., 2001; Rosenthal et al., 1999), where it
70 recognizes and recruits ubiquitinated cell surface receptors to clathrin-coated pits for
71 internalization via its ubiquitin-interacting motif (UIM) and clathrin/AP-2 binding sites,
72 respectively (Chen and De Camilli, 2005; Cui et al., 2020; Polo et al., 2002; Shih et al., 2002).
73 Epsins 1 and 2 are ubiquitously expressed, redundant in function, and essential for embryonic
74 survival (Chen et al., 2009). The embryonic lethality of Epsin 1 and 2 double knockout mice
75 (DKO) prompted us to generate conditional Epsin1$^{fl/fl}$; Epsin2$^{-/-}$ mice. Combining DKO strains
76 with specific Cre deleter mouse strains creates tissue and cell type-specific DKO mice (Chen et
77 al., 2009; Tessneer et al., 2014). Despite their multifaceted functions, our previous work
78 demonstrates that Epsins possess a vast degree of specificity and selectivity in choosing their
79 binding partners. Therefore, the actions of Epsins are cell context-dependent (Brophy et al., 2019;
80 Chang et al., 2015; Chen et al., 2009; Dong et al., 2020; Dong et al., 2021; Liu et al., 2014; Pasula
81 et al., 2012; Tessneer et al., 2014). Notably, we demonstrated that myeloid-specific Epsins loss
82 downregulated inflammation and impeded atheroma formation in an atherogenic mouse model by
83 stabilizing macrophage LRP-1 (Brophy et al., 2019). However, this model failed to address the
84 role of epsins in hindering atheroma regression and promoting plaque rapture and consequent
85 debilitating episodes.

86 Lesional macrophages internalize lipids primarily through scavenger receptor-mediated
87 endocytosis (Moore and Freeman, 2006), which is also responsible for foam cell formation
88 (Febbraio et al., 2000; Kunjathoor et al., 2002; Nozaki et al., 1995; Ouimet et al., 2017; Podrez et
89 al., 2000). Mice lacking both Scavenger Receptor-A (SR-A) and CD36 revealed that CD36 is the
90 major oxLDL receptor required for foam cell formation (Febbraio et al., 2000; Kunjathoor et al.,
91 2002; Nozaki et al., 1995; Podrez et al., 2000). Our previous studies revealed that Epsins 1 and 2

are upregulated in lesional macrophages (Brophy et al., 2019). Epsin-deficient (DKO) macrophages exhibited a striking reduction in foam cell formation (Brophy et al., 2019). As robust lipid uptake by macrophages is one of major responsible factors that drive foam cell formation, we posit a central role Epsins play in regulating lipid uptake in macrophages. However, how Epsins facilitate lipid uptake and whether this is through scavenger receptor-mediated uptake of modified LDL during foam cell formation remains elusive.

Reverse cholesterol transport (RCT) is responsible for removing excess cholesterol from peripheral tissues to the liver, where it is reused or removed from the body (Ohashi et al., 2005). A critical part of RCT is cholesterol efflux, where accumulated cholesterol removed from macrophages in the subintima is mediated by ATP-binding membrane cassette transporters (ABCA1 and ABCG1) and other molecules (Kennedy et al., 2005; Westerterp et al., 2016; Yvan-Charvet et al., 2007). Among the regulators of RCT, ABCG1 plays a prominent role in macrophage cholesterol and phospholipid transport to maintain cellular lipid homeostasis by using high density lipoprotein (HDL) as a cholesterol acceptor (Sag et al., 2015). HDL is thought to facilitate macrophages re-programming to be less inflammatory through an ATF-3-dependent pathway (Moore and Fisher, 2014). Several clinical trials and more recent work suggest that increased HDL-cholesterol concentrations fail to improve cardiovascular disease outcomes (Keene et al., 2014; Nicholls et al., 2018; Tardif et al., 2007); however, new data indicate that rather than the steady-state HDL-cholesterol (HDL-C) levels (Hewing et al., 2012), the ability of HDL particles to transport cholesterol from atherosclerotic plaques to the liver is more important (Josefs et al., 2021; Khera et al., 2011). Consequently, a shift in focus from increasing HDL-cholesterol concentrations to raising RCT function by increasing cholesterol efflux capacity (CEC), the HDL-ABCG1-mediated cholesterol efflux from macrophages, has become a

prospective therapy for coronary artery disease (CAD), especially in severe acute myocardial infarction (AMI) patients (Capodanno et al., 2018; Ouimet et al., 2019; Rohatgi et al., 2014; Silvain et al., 2019). As lack of effective cholesterol efflux in macrophages hinders the reversal of foam cells back to healthy macrophages, we envision a major role macrophage Epsins play in regulating cholesterol efflux. Given the importance of cholesterol efflux and RCT in atheroma resolution and aforementioned risk reduction in AMI patients (Kennedy et al., 2005; Westerterp et al., 2016; Yvan-Charvet et al., 2007), it is crucial to determine whether Epsins inhibit cholesterol efflux and RCT to impede atherosclerotic plaque progression and promote its regression.

In this study, we harnessed novel nanotechnology and are the first to unveil the detrimental role of epsins in prohibiting atheroma regression and promoting plaque rapture using a preclinical atherosclerosis regression model. Mechanistically, we utilized RNA seq analysis of macrophages to identify new targets involved in lipid metabolism during atherosclerosis. Based on these new targets, we employed a novel myeloid-specific-deficient ABCG1 animal model to uncover how epsins regulate lipid metabolism to propel atherosclerosis. Specifically, we show that epsins facilitate CD36-mediated lipid uptake and inhibit ABCG1-mediated cholesterol efflux, which is entirely new in the field of lipid metabolism. Secondary, we employed an originally designed macrophage-specific nanoparticle delivery system to investigate the therapeutic prevention for atherosclerosis. Lastly, an early-stage progression model, an advanced-stage progression model, and a regression model of atherosclerosis have been employed to demonstrate a profound therapeutic benefit in treating atherosclerosis by the aforementioned nanoparticle delivery system. we believe our vigorous and novel mechanistic study on lipid metabolism, and clinically relevant

nanoparticle-mediated RNAi therapies represents an impactful advance for treating this devastating disease.

RESULTS

RNA-Seq analyses reveal that Epsins regulate cholesterol metabolism and efflux pathways

Molecular mechanisms underlying Epsin-mediated regulation of foam cell formation and promotion of lipid uptake by macrophages are poorly understood. As an unbiased and genome wide approach, we performed RNA-seq analysis on macrophages isolated from wild type (WT) and DKO mice. Loss of Epsins 1 and 2 significantly altered the expression of 2208 genes. These include 1138 downregulated and 1070 upregulated genes (Fig. S1A-S1C). Notably, the differential genes are associated with cholesterol efflux and metabolism, suggesting that Epsins play a role in regulating lipid cholesterol metabolism and efflux pathways (Fig. 1A). Consistently, Gene Ontology (GO) enrichment analysis featured pathways including regulation of cholesterol metabolic process, lipid catabolic process, sterol biosynthetic process, macrophage migration, and regulation of immune effector process (Fig. 1B). Furthermore, Gene Set Enrichment Analysis (GSEA) showed that enriched genes that are related to fatty acid metabolism tended to be markedly downregulated in DKO macrophages (Fig. 1C). In contrast, genes associated with cholesterol transport and efflux (Fig. 1D), and negative regulation of macrophage foam cell formation (Fig. 1E), tended to be upregulated by Epsin deficiency.

CD36 is one of the major scavenger receptors responsible for oxLDL uptake in macrophages, and deletion of CD36 in macrophages reduces foam cell formation and atherosclerosis (Kunjathoor et al., 2002; Podrez et al., 2000). Likewise, Epsin deficiency also reduced foam cell formation and lipid uptake in macrophages (Brophy et al., 2019). The similar phenotype shared by Epsin

160 deficiency and CD36 deficiency promoted us to explore the relationship between Epsins and CD36.
161 We compared our DKO macrophage RNA-seq data with a public RNA-seq data from wild type
162 and CD36 knockout (CD36KO) macrophages in the public database (Chen et al., 2019). We
163 observed a significant overlap of differential genes induced by the Epsin-DKO and CD36KO
164 mouse macrophages. There were 169 genes significantly upregulated by both Epsin-DKO and
165 CD36KO (4-fold enrichment compared to the 41 genes expected by random chance, Fisher's exact
166 test p value 9.73×10^{-25}) (Fig. 1F left panels); 29 genes (6-fold enrichment, Fisher's exact test P
167 value 6.15×10^{-9}) were downregulated by both Epsin-DKO and CD36KO (Fig. 1F right panels).
168 Heatmap indicated that the genes significantly regulated only by Epsin-DKO still tends to be
169 regulated by CD36KO in the same direction, although to a non-significant degree (Fig. 1G). These
170 results are consistent with GO analysis that revealed a number of common pathways regulated by
171 Epsin or CD36 deficiency. These include the downregulation of inflammation pathway, lipid
172 biosynthetic process, triglyceride metabolic process, and upregulation of small GTPase mediated
173 signal transduction pathway (Fig. 1H). Examples of differentially regulated genes in Espin-DKO
174 and CD36KO macrophages include the Ccnd2 that is a cell cycle regulator (Fig. S2A) (Meyerson
175 and Harlow, 1994), the Ch25h that is a cholesterol biosynthesis repressor (Fig. S2B) (Lund et al.,
176 1998), and the Ccl9 that is a chemokine (Fig. S2C) (Yu et al., 2002). These results indicate that
177 Epsins and CD36 play superimposing roles in regulating molecular pathways involved in lipid
178 metabolism and inflammation.

179 To further interrogate the molecular mechanisms governing Epsin-mediated lipid uptake, we
180 sought to compare our RNA-seq data to the RNA-seq data obtained from non-foam cell
181 macrophages and macrophage-derived foam cells (Kim et al., 2018). Interestingly, we found an
182 intimate reversal relationship in gene expression patten between DKO macrophages and foam cells.

Specifically, genes downregulated by DKO in macrophages tend to be highly upregulated in foam cells relative to macrophages (Fig. S3A and S3B). Also, genes upregulated by DKO in macrophages tend to be downregulated in foam cells relative to macrophages (Fig. S3C and S3D). These results substantiated our previous findings that Epsin loss prevents foam cell formation.

Epsin promotes CD36-mediated lipid uptake by promoting CD36 endocytosis and recycling

Based on the bioinformatic results, we hypothesized that Epsins regulate CD36 internalization and lipid uptake. We performed qRT-PCR, western blot (WB) and flow cytometry to check the RNA, total protein, and surface protein levels of CD36. Interestingly, RNA (Fig. 2A) and total protein (Fig. 2B) expression of CD36 remained unchanged between WT and DKO macrophages. However, the surface protein level of CD36 significantly decreased with the treatment of oxLDL in WT, but not in DKO macrophages (Fig. 2C and S4). Immunofluorescence staining (IF) revealed oxLDL-induced CD36 trafficking to early endosomes. We observed colocalization of CD36 with EEA1 (early endosome antigen 1, Fig. 2D) and Rab11 (recycling endosome marker, Fig. 2E) in WT macrophages treated with oxLDL, which was not observed in DKO macrophages.

To further study the role of Epsins in regulating macrophage lipid uptake, we stained oxLDL-treated WT and DKO macrophages with BODIPY and Oil Red O (ORO). Deficiency of Epsins impaired oxLDL uptake and foam cell formation (Fig. 2F and S5) and reduced cholesterol and triglyceride levels (Fig. 2G) in DKO macrophages. Flow cytometry confirmed that macrophage lipid uptake was reduced in DKO macrophages using DiI-oxLDL treatment (Fig. 2H and S4). Together, these results indicate that Epsins are crucial for CD36-mediated lipid uptake and cholesterol metabolism.

Epsin ENTH domain is required for CD36-mediated lipid uptake and foam cell formation

206 Next, we investigated how Epsins and CD36 interact to cause the disparity in CD36 surface
207 and total protein levels using immunoprecipitation (IP) and WB. We determined that CD36 binds
208 Epsin1 in WT, but not in DKO macrophages (Fig. 3A). This indicated that Epsin1 and CD36
209 interact endogenously. We then determined which Epsin regions were responsible for this
210 interaction. We created Flag-tagged mammalian Epsin1 wild type full length and ENTH or UIM
211 deleted constructs (FLAG-Epsin1^{WT}, FLAG-Epsin1$^{\triangle ENTH}$ or FLAG-Epsin1$^{\triangle UIM}$) (Fig. 3B). Then
212 we transfected these constructs to HEK 293T cells and performed co-IP with CD36. The
213 interaction between Epsin1 and CD36 was Epsin dependent on the ENTH domain as the binding
214 between Epsin1$^{\triangle ENTH}$ and CD36 was dramatically reduced in FLAG-Epsin1$^{\triangle ENTH}$-expressing cells
215 (Fig. 3B). As expected, we did not detect ubiquitinated CD36 in response to oxLDL treatment in
216 the presence of the proteasome inhibitor MG132 (Fig. 3C). In addition, we transfected the Epsin
217 full length and deletion Epsin constructs into WT and DKO macrophages treated with oxLDL. The
218 transfection of full-length Epsin restored lipid uptake in DKO macrophages, which was not
219 observed in cells expressing FLAG-Epsin1$^{\triangle ENTH}$ (Fig. 3D, 3E and S6).
220

221 **RNA-seq analyses of WT, Epsin-DKO and ABCG1-KO macrophages reveal that Epsins and**
222 **ABCG1 reciprocally regulate inflammation and lipid metabolism pathways**

223 Emerging evidence spotlighted raising RCT function by increasing HDL-cholesterol efflux
224 capacity (CEC) to prominence as a prospective strategy to treat repeat heart attacks. We have
225 generated myeloid-specific ABCG1-knock out (ABCG1-KO) mice. Given intimate relationship of
226 HDL with ABCG1 in regulating cholesterol efflux, and involvement of Epsins in cholesterol efflux
227 regulation, we performed RNA-seq analysis of WT, ABCG1-KO and Epsin-DKO macrophages.
228 The loss of ABCG1 in macrophages significantly altered the expression of 1733 genes, including

986 downregulated and 747 upregulated genes (Fig. S7A-S7C). GSEA indicated that genes associated with the inflammatory response (Fig. 4A) and macrophage activation (Fig. 4B) are upregulated by ABCG1-KO in macrophages. In contrast, genes negatively regulating macrophage-derived foam cell formation are downregulated by ABCG1-KO (Fig. 4C). We further performed GO enrichment analysis for genes up- and down-regulated in ABCG1-KO relative to WT macrophages. Positive regulation of cytokine production, tumor necrosis factor production and acute inflammatory response were upregulated by ABCG1-KO in macrophages (Fig. 4D). Negative regulation of lipid storage and cholesterol biosynthetic process were down regulated in ABCG1-KO compared to WT macrophages (Fig. 4D). Interestingly, GSEA analyses showed that genes associated with cell immune response (Fig. S7D), regulation of leukocyte migration (Fig. S7E) and leukocyte proliferation (Fig. S7F) are markedly upregulated by ABCG1 deficiency in macrophages. In contrast, these genes are drastically downregulated in DKO macrophages (Fig. S7D-S7F), These results suggest that Epsins and ABCG1 reciprocally regulate inflammation pathways. Examination of individual gene expression confirmed common target genes reversely regulated by Epsins and ABCG1. For instance, Itgb3 prevents the differentiation of macrophages and monocytes into foam cells (Antonov et al., 2004) and was up and down regulated by DKO and ABCG1-KO, respectively (Fig. 4E). In addition, GO enrichment analysis revealed pathways reversely regulated by ABCG1-KO and DKO in macrophages (Fig. 4F). Our RNA-seq analyses from ABCG1-KO and Epsin-DKO further support that Epsins and ABCG1 play an opposing role in regulating cholesterol efflux and inflammatory responses and foam cell formation.

Epsin loss augments macrophage cholesterol efflux *in vitro* and RCT *in vivo*

RNA-seq analysis of WT, DKO, and ABCG1-KO macrophages indicated that the loss of Epsins affects cholesterol efflux. At the same time, we wanted to determine if Epsins inhibit cholesterol efflux and RCT to ameliorate atherosclerosis. WT and DKO macrophages were pre-treated with a LXR agonist (T0901317) and incubated with [^{3}H]-cholesterol and ac-LDL. We found that in vitro cholesterol efflux to HDL, but not ApoA-1, was markedly enhanced in DKO versus WT macrophages (Fig. 5A and 5B). Consistently, in vivo RCT (Fig. 5C) was elevated in mice injected with [^{3}H]-cholesterol-loaded DKO macrophages compared to WT macrophages. Our results showed that [^{3}H]-radioactivity in liver, plasma, feces, and intestinal contents all showed significant increases in mice injected with DKO macrophages, but not those injected with WT macrophages (Fig. 5D-5I and S8). These findings suggest that Epsin-deficient macrophages have higher cholesterol efflux and RCT.

Epsin-UIM domain binds ABCG1 to promote degradation via the lysosome

To investigate the molecular mechanisms underlying Epsin-mediated ABCG1 regulation, we sought to test whether Epsins interact with ABCG1 and govern its turnover in macrophages. We first assessed protein levels of surface receptors such as ABCG1, ABCA1, SR-A1, and LDLR in macrophages involved in the progression of atherosclerosis. WB results showed that ABCG1, but not ABCA1, SR-A1 and LDLR, were upregulated in primary macrophages from DKO mice when compared to WT mice (Fig. 6A). The mRNA levels of ABCG1 in both WT and DKO macrophages remain unchanged (Fig. S9). Because ABCG1 is known to mediate cholesterol efflux to HDL (Ouimet et al., 2019), we hypothesized that Epsins bind ABCG1 under atherosclerotic conditions and promote ABCG1 ubiquitin-dependent degradation to inhibit cholesterol efflux in macrophages and facilitate development of atherosclerosis. Indeed, when the isolated peritoneal macrophages

from DKO and WT mice were pretreated with a liver X receptor (LXR) activator followed by a cell surface biotinylation assay, we observed significantly elevated levels of biotinylated ABCG1 in DKO macrophages (Fig. 6B). We also performed flow cytometry and observed that only WT macrophages showed a decreased surface level of ABCG1 with the oxLDL treatment (Fig. 6C and S10). Therefore, decreased total and surface levels of ABCG1 in WT macrophages implies that Epsins promote ABCG1 degradation.

We next sought to determine how Epsins caused increases in total and surface protein levels of ABCG1 in macrophages from DKO mice. When peritoneal or bone marrow-derived macrophages from WT and DKO mice were lysed and processed for IP with anti-Epsin1 antibodies, we observed ABCG1 in WT macrophages, but not in DKO macrophages (Fig. 6D). This suggested that Epsins bind to ABCG1. Accordingly, we determined that Epsin interacted with ABCG1 via Epsin UIM domain, which was confirmed by transfection of Flag-tagged mammalian Epsin wild type full length, ENTH, or UIM deletion constructs as well as ABCG1 plasmid to HEK 293T cells (Fig. 6E). We showed that ABCG1 is ubiquitinated in response to oxLDL, allowing Epsins to interact with ABCG1 through their UIM, which promotes ABCG1 lysosomal degradation (Fig. 6F). In addition, we observed oxLDL-induced ABCG1 trafficking to early endosomes (Fig. 6G) and lysosomes (Fig. 6H) in WT macrophages, but not DKO cells.

To substantiate that elevated cholesterol efflux and RCT were a result of increased total and surface levels of ABCG1 in ApoE$^{-/-}$/LysM-DKO macrophages, we created ApoE$^{-/-}$/LysM-DKO-ABCG1$^{fl/+}$ mice by crossing the ApoE$^{-/-}$/LysM-DKO mouse strain with ABCG1 (flox/+) heterozygous mice to generate a novel mouse model (ApoE$^{-/-}$/LysM-DKO/ABCG1$^{myeloid\text{-}het}$) with genetically-reduced ABCG1 levels in Epsin-deficient macrophages (Fig. 5J). We observed reduced gene (Fig. 5K) and protein (Fig. 5L) expression of ABCG1 in ApoE$^{-/-}$/LysM-DKO-

297 ABCG1$^{fl/+}$ macrophages. The LysM-DKO-ABCG1$^{fl/+}$ macrophages showed less cholesterol efflux
298 to HDL and RCT compared to ApoE$^{-/-}$/LysM-DKO macrophages (Fig. 5A, 5B and 5D-5I). These
299 studies demonstrate that the deficiency of Epsins in macrophages specifically enhanced ABCG1-
300 mediated cholesterol efflux to HDL and RCT, which is inversely related to the risk of atherosclerotic
301 cardiovascular disease. In accordance, immunostaining of human patient aortic arch (Fig. S11A) and
302 mouse aortic root (Fig. S11B) sections revealed that ABCG1 expression is inversely associated
303 with atherosclerotic plaque severity, i.e., there is considerably reduction in ABCG1 expression in
304 more severe atheroma compared to that in less severe atherosclerotic plaques in both human and
305 mouse atheromas.
306
307 **S2PNP-siEpsin1/2 hinders progression of early and advanced stages of atherosclerosis**
308 Since we found that Epsins facilitate internalization of CD36-mediated lipid uptake and
309 promotes ABCG1 degradation to inhibit ABCG1-mediated cholesterol efflux, we sought to
310 determine whether targeting Epsins could prevent the progression of atherosclerosis. We used a
311 targeted NP platform (Tao et al., 2020) modified with a lesional macrophage-specific targeting
312 peptide (S2P) for systemic delivery of Epsins 1 and 2 siRNA combinations (S2PNP-siEpsin1/2)
313 (Fig. S12A).
314 Isolated macrophages from WT mice were treated with S2PNP-siControl (S2PNP-siCtrl) or
315 S2PNP-siEpsin1/2. Then, RNA and protein were isolated to check the *in vitro* silencing efficacy
316 of the NPs (Fig. S12B and S12C). To assess the effect of NPs on *in vitro* peritoneal macrophage
317 lipid loading, cells isolated from ApoE$^{-/-}$ mice were treated with S2PNP-siCtrl or S2PNP-
318 siEpsin1/2 for 24h followed by treatment with oxLDL or plasma isolated from ApoE$^{-/-}$ mice fed a
319 WD for 8 weeks. The treatment of oxLDL or plasma demonstrated decreased lipid uptake by

S2PNP-siEpsin1/2-treated macrophages compared to S2PNP-siCtrl treated cells (Fig. S13A and S13B).

ApoE$^{-/-}$ mice fed a WD for 8 weeks (early stage, Fig. S14) or 17 weeks (advanced stage, Fig. 7) were divided into three groups including baseline (before NP injection), S2PNP-siCtrl, and S2PNP-siEpsin1/2. The baseline group was sacrificed before the injection of NPs.

S2PNP-siCtrl or S2PNP-siEpsin1/2 was intravenously injected twice a week for 3 weeks (Fig. S14A and 7A). Digested lesions from S2PNP-siCtrl or S2PNP-siEpsin1/2 treated mice were used for WB to check *in vivo* silencing of Epsins 1 and 2 (Fig. S14B). Additionally, the administration of S2PNP-siEpsin1/2 resulted in not only a decrease in lesional macrophage accumulation, but also a significant reduction of Epsins 1 and 2 expressions within the atherosclerotic plaques as showed by diminished CD68 and Epsins 1 and 2 staining in the aortic root sections (Fig. S14C and S14D). *En face* ORO staining in aortas, aortic roots, and brachiocephalic artery (BCA) sections (Fig. S14E, 7B and 7C) showed reduced lesion size, lesion number, and retarded progression of both early (11 weeks on WD) and advanced (20 weeks on WD) stages atherosclerosis in ApoE$^{-/-}$ mice treated with S2PNP-siEpsin1/2 opposed to the S2PNP-siCtrl group.

Inhibiting the transition of atheroma from stable lesion to vulnerable plaque is paramount in preventing heart attacks and strokes. We observed elevated smooth muscle cell contents and reduced macrophage accumulation (Fig. 7D), increased elastic fibers and collagen content (Fig. S15), and reduced necrotic core area (Fig. 7E) within the atherosclerotic lesions in S2PNP-siEpsin1/2 treated mice compared to S2PNP-siCtrl group. In addition, we observed no changes in plasma total cholesterol, triglycerides, or HDL and non-HDL cholesterol levels between S2PNP-siCtrl and S2PNP-siEpsin1/2 treated mice (Fig. S16). These features suggest that the

administration of lesion macrophage-specific targeting NPs containing Epsin1/2 siRNA can stabilize the atherosclerotic plaques without affecting the plasma cholesterol levels.

S2PNP-siEpsin1/2 promotes atheroma resolution by diminishing inflammation and enhancing lesion stability

Given the critical role of macrophage cholesterol efflux and RCT in atheroma resolution, we also wanted to assess the therapeutic effects of S2PNP-siEpsin1/2 on atheroma resolution. We established another mouse model by injecting proprotein convertase subtilisin kexin type 9-adeno-associated virus-8 (AAV8-PCSK9D377Y) into C57BL/6 mice. This generated an atherosclerosis mouse model harboring a gain-of-function PCSK9 mutant (Oppi et al., 2019). This model mimics LDLR null mice (Brophy et al., 2019) and requires no genetic modification (Oppi et al., 2019). Another advantage of this mouse line is that a single AAV injection is sufficient to generate atherosclerotic mice by WD feeding compared to long-term crossbreeding with $ApoE^{-/-}$ or $LDLR^{-/-}$ mice.

To test if S2PNP-siEpsin1/2 treatment can promote atheroma resolution, PCSK9-AAV8 mice fed a WD for 16 weeks followed by 4 weeks of a normal diet with S2PNP-siCtrl or S2PNP-siEpsin1/2 treatment (Fig. 8A). The latter group showed a significant reduction of lesion size and rapid lesion regression as evidenced in the IF and ORO staining of the whole aorta, aortic root and BCA sections (Fig. 8B, 8C, 8D and S17A). Van Gieson's trichrome staining of BCA sections showed increased collagen content and elastic fibers in the S2PNP-siEpsin1/2 group compared to S2PNP-siCtrl or baseline group (Fig. S17B). In addition, the IF co-staining of CD68 and α-SMA showed reduced macrophage accumulation in the fibrous cap, reduced size of atheromatous cores,

and increased smooth muscle cell content within the atheroma cap in the S2PNP-siEpsin1/2 group (Fig. 8C).

Adhesion molecules play a crucial role in attaching monocytes to activated endothelial cells (EC) as well as recruiting monocytes to the sub-endothelial layer. Co-staining of CD31 with vascular cell adhesion molecule-1 (VCAM-1, Fig. 8E), intercellular adhesion molecule-1 (ICAM-1, Fig. 8F), P-selectin (Fig. 8G) or E-selectin (Fig. 8H) was performed using aortic root sections. Administration of S2PNP-siEpsin1/2 significantly suppressed these adhesion molecules when compared to S2PNP-siCtrl group. In addition, the expression of the macrophage egressing gene CCR7 was significant increased, while the retention genes Sema3a and Netrin1 were decreased in DKO macrophages (Fig. S17C). This is consistent with our RNA-seq analysis that showed the deficiency of macrophage Epsins facilitates immune cell migration. Furthermore, macrophages treated with S2PNP-siEpsin1/2 showed decreased expression of pro-inflammatory genes (iNOS, IL-6, IL-1β, and TNF-α) and increased expression of anti-inflammatory markers (IL-10 and Arg1) compared to the S2P-siCtrl group (Fig. 8J). These decreased pro-inflammatory cytokines lead to reduced ICAM-1, VCAM-1, P- and E-selectins expression in ECs (Fig. 8E-8H), hindering recruitment of additional macrophages to the lesion. Taken together, these results indicate that specific silencing of Epsins in lesional macrophages may offer therapeutic benefits in preventing or treating advanced atherosclerosis.

DISCUSSION

In this study, we discover that the Epsins 1 and 2 endocytic adaptor proteins govern lipid metabolism and cholesterol transport (Fig. S18) in atherosclerotic macrophages by regulating CD36-mediated lipid uptake (Fig. 1-3 and S1-S6) and ABCG1-dependent cholesterol efflux (Fig.

387 4-6 and S7-S11). Importantly, we demonstrate that targeting lesional macrophage Epsins using a
388 newly developed nanotechnology-based siRNA-mediated therapy halts inflammation, impedes
389 early and late atherogenesis (Fig. 7 and S12-S16), and accelerates atheroma resolution (Fig. 8 and
390 S17). By silencing lesional macrophage Epsins, we observed a reduction in necrotic core area in
391 atherosclerotic lesions and marked attenuation in inflammation (Fig. 7 and Fig. 8). Together, our
392 studies point toward a promising new strategy for the treatment of atherosclerosis.

393 The advent of next generation therapies targeting PCSK9, including monoclonal anti-PCSK9
394 antibodies and PCSK9 siRNA, is considered to be game-changing (Feingold, 2000; Fitzgerald et al.,
395 2017; German and Shapiro, 2020); however, these and other therapies largely ignore the rampant
396 inflammation that occurs in atherosclerotic arteries. Arterial inflammation is a prime contributor
397 to the transition from a stable to vulnerable atheroma (Alsheikh-Ali et al., 2010; Doring, 2015;
398 Hansson et al., 2015; Virmani et al., 2006). While anti-inflammatory medicines such as anti-
399 Interleukin-1β antibodies potently diminish the risk of recurrent myocardial infarction, these
400 treatments may come with some severe side effects (De Benedetti et al., 2018; Ridker et al., 2017).
401 In addition, the inability to reduce lipid ingestion while concomitantly reinforce cholesterol efflux
402 in lesional macrophages has impeded the battle against atherosclerosis. Our mechanistic studies
403 show that Epsins bind to CD36 to facilitate lipid uptake by enhancing CD36 endocytosis and
404 recycling. Conversely, Epsins promote ABCG1 degradation via lysosomes and hamper ABCG1-
405 mediated cholesterol efflux and reverse cholesterol transport. Excitingly, by harnessing the latest
406 development in nanomedicine and developing S2P-NPs carrying Epsin1/2 siRNAs (S2PNP-
407 siEpsin1/2), we show a reduction in plaque formation in both early and advanced atherosclerosis
408 (Fig. S14 and 7). Furthermore, in a pre-clinical atheroma resolution model, this potent approach
409 reduced lesional macrophage accumulation, decreased pro-inflammatory cytokine and adhesion

molecule expression, and accelerated plaque regression (Fig. 8). Taken together, our study uncovers a novel and critical role for Epsin in regulating lipid metabolism and cholesterol efflux as well as offers a potential new nanotherapy for treating atherosclerosis by targeting Epsins in macrophages.

As we show that silencing of lesional macrophage Epsins reduces necrotic core size, we reasoned that inhibiting Epsins may reinforce efferocytosis in macrophages, analogous to our observations in DKO macrophages (Brophy et al., 2019) given that efferocytosis plays a central role in regulating necrotic core formation (Gerlach et al., 2021; Kojima et al., 2017; Thorp et al., 2008). Despite the fact that S2P-NPs have been shown to only negligibly target the endothelium (Tao et al., 2020), whether S2PNP-siEpsin1/2 prohibits endothelial Epsins to synergistically curb atherosclerosis may require further investigation as deletion of endothelial Epsins also reduces inflammation and atherogenesis (Dong et al., 2020; Dong et al., 2021). Interestingly, we did not observe significant changes of the lipid profiles in the plasma from S2PNP-siCtrl and S2PNP-siEpsin1/2 treated ApoE$^{-/-}$ mice, suggesting either a minor liver targeting by S2PNP-siEpsin1/2 or that S2PNP-siEpsin1/2-mediated silencing of Epsins in liver could be inconsequential. Nevertheless, whether S2PNP-siEpsin1/2 targets liver epsins warrants further investigation.

While autophagy can eliminate excess lipid droplet-associated cholesterol esters taken up by macrophages (Evans et al., 2017; Le Guezennec et al., 2012; Ouimet et al., 2011; Sergin et al., 2017), this process is attenuated during atheroma progression, leading to defective lipolysis, impaired efferocytosis, and escalated inflammation, which increases the likelihood of vulnerable lesion rupture (Butcher et al., 2011; Evans et al., 2017; Le Guezennec et al., 2012; Ouimet et al., 2011; Purcell-Huynh et al., 1995; Razani et al., 2012; Sergin et al., 2017). A recent report suggests that macrophage SR-B1 modulates autophagy through the VPS34 complex and PPARα

transcription of Tfeb in atherosclerosis (Tao et al., 2021). SR-B1 is a multifunctional membrane receptor, which is not only responsible for selective uptake of HDL- derived cholesteryl esters into cells, but also for transferring HDL-cholesterol efflux from peripheral tissues to back to liver (Van Eck et al., 2004). Given that Epsins are implicated in autophagy function in *Drosophila* (Csikos et al., 2009), the question of whether these proteins suppress autophagic activity by binding to SR-B1 and inhibiting SR-B1-regulated function in macrophages remains unanswered.

Our studies also revealed that LXR-activated macrophage surface expression of ABCG1 was significantly reduced with oxLDL treatment in WT, but not in DKO macrophages owing to their internalization and degradation mediated by the Epsins (Fig. 6). It is thought that basal macrophage ABCG1 is largely located at an intracellular location (Tarling and Edwards, 2011) and then redistributed to the cell surface following LXR activation (Wang et al., 2006). Our immunostaining and biotinylation studies (Fig. 6) are consistent with these observations. More importantly, staining of ABCG1, in both human patient aortic arch and mouse aortic root sections, exhibits a reduction in ABCG1 expression in severe atherosclerotic lesions (Fig. S11), suggesting a pivotal role of loss of Epsins in maintaining the abundance of ABCG1 and limiting plaque buildup. Recent clinical trials suggest that enhanced cholesterol efflux capacity (CEC) considerably reduces the risk of repeat heart attacks and severe acute myocardial infarction (MI) (Keene et al., 2014; Nicholls et al., 2018; Tardif et al., 2007). In addition, cholesterol efflux capacity has minimal links to various risk factors and metabolic issues in contrast to HDL cholesterol level (Rohatgi et al., 2014). Our results show that targeting Epsins augments cholesterol efflux (Fig. 5 and S16) and consequently, may potentially enhance CEC, suggesting that inhibiting Epsins represents a promising new strategy for treating patients suffering from recurrent MI and severe CAD.

In conclusion, our results provide a powerful proof-of-concept for the therapeutic potential of Epsin siRNA-containing NPs to precisely target lesional macrophages to abolish inflammation and resolve atheroma. By illustrating that targeting Epsins expression in macrophages restricts lipid ingestion in foam cells and concomitantly enhances cholesterol efflux, we believe this study provides a foundation for the renewed quest seeking innovative therapies that precisely resolve lesional inflammation in advanced atherosclerosis.

Limitations of the study

In this study, we employed an originally designed macrophage-specific nanoparticle delivery system to investigate the therapeutic prevention for atherosclerosis. A major technical limitation is that mouse is not the ideal preclinical model to study atherosclerosis and plaque rupture as mouse does not express CEPT and contains mainly circulating HDL vs LDL in humans. Larger animal models such as pigs, rabbits and non-human primates more closely replicate atherosclerotic disease conditions in humans. However, these experiments will require enormous resources to complete as they demand the nanotherapy production in an industrial scale and the most appropriate large animal model that requires years to establish. Most challengingly, critical reagents such as commercially available antibodies may fail to recognize the antigens present in these large animals. Despite effective lipid-lowering statin therapies and anti-PCSK9 agents, many patients exhibit resistance to statin therapies and/or intolerance to anti-PCSK9 regime. Nevertheless, how the efficacy of our nanotherapy in preventing the atherosclerotic plaque from transitioning to a vulnerable one or promoting the regression of atherosclerosis is compared to that of statins and anti-PCSK9 remains to be determined.

STAR★METHODS

Detailed methods are provided in the online version of this paper.

ACKNOWLEDGMENTS: We thank researchers for providing their GEO database information online. We thank the Flow Cytometry Core at Boston Children's Hospital for the use of the LSRII, the Viral Core at Boston Children's Hospital for providing viral stocks, and the Biopolymers Facility at Harvard Medical School for quality control analysis of RNA samples.

FUNDING: This work was supported by R01HL146134 (H.C., S.S., M.F.L.) and American Heart Association Established Investigator Award and Transformational Project Award (H.C.), and in part by NIH grants R01HL137229, R01HL141853, R01HL156362, R01HL158097, R01HL162367, (H.C.), AHA 17SDG33410868 (H.W.), and P01 HL116263 (M.F.L.).

AUTHOR CONTRIBUTIONS: K.C. J.S., K.F.C. and H.C. conceived and designed the study. K.C. primarily contributed to the identification of the in vitro molecular mechanism. K. C. and B.W. primarily contributed to the in vivo data in atherosclerosis analysis. X.G., K.C. and K.F.C. conducted the RNA-seq data analysis and interpretation. H.W. and Y. D worked on part of the molecular mechanism investigation and provided biochemistry insights. Y.X. and X.J. synthesized, characterized the nanoparticles. M.M. performed the cholesterol and triglyceride analysis. S.C., Y.L, and B.Z. provided technical support in RNA-seq experiment. K.C., D.S. and Q.P. analyzed the data and provided comments. S.W. provided technical support with mouse genotyping and colony maintenance. K.C. and H.C. wrote the manuscript. K.C., D.B.C., K.L., S.S., M.F.L., J.S., K.F.C., and H.C. edited the manuscript. All the authors reviewed and provided feedback on the manuscript.

DECLARATION OF INTERESTS: All authors declare that they have no competing interests.

DATA AND MATERIALS AVAILABILITY: The authors declare that all data, code, and materials used in the analysis are available in the main text or the supplementary materials.

REFERRENCES

Alsheikh-Ali, A.A., Kitsios, G.D., Balk, E.M., Lau, J., and Ip, S. (2010). The vulnerable atherosclerotic plaque: scope of the literature. Ann Intern Med *153*, 387-395.

Anders, S., Pyl, P.T., and Huber, W. (2015). HTSeq--a Python framework to work with high-throughput sequencing data. Bioinformatics *31*, 166-169.

Antonov, A.S., Kolodgie, F.D., Munn, D.H., and Gerrity, R.G. (2004). Regulation of macrophage foam cell formation by alphaVbeta3 integrin: potential role in human atherosclerosis. Am J Pathol *165*, 247-258.

Brophy, M.L., Dong, Y., Tao, H., Yancey, P.G., Song, K., Zhang, K., Wen, A., Wu, H., Lee, Y., Malovichko, M.V., et al. (2019). Myeloid-Specific Deletion of Epsins 1 and 2 Reduces Atherosclerosis by Preventing LRP-1 Downregulation. Circ Res *124*, e6-e19.

Butcher, M.J., Herre, M., Ley, K., and Galkina, E. (2011). Flow cytometry analysis of immune cells within murine aortas. J Vis Exp.

Capodanno, D., Mehran, R., Gibson, C.M., and Angiolillo, D.J. (2018). CSL112, a reconstituted, infusible, plasma-derived apolipoprotein A-I: safety and tolerability profiles and implications for management in patients with myocardial infarction. Expert Opin Investig Drugs *27*, 997-1005.

Chang, B., Tessneer, K.L., McManus, J., Liu, X., Hahn, S., Pasula, S., Wu, H., Song, H., Chen, Y., Cai, X., et al. (2015). Epsin is required for Dishevelled stability and Wnt signalling activation in colon cancer development. Nat Commun *6*, 6380.

Charo, I.F., and Taub, R. (2011). Anti-inflammatory therapeutics for the treatment of atherosclerosis. Nat Rev Drug Discov *10*, 365-376.

Chen, H., and Boutros, P.C. (2011). VennDiagram: a package for the generation of highly-customizable Venn and Euler diagrams in R. BMC Bioinformatics *12*, 35.

Chen, H., and De Camilli, P. (2005). The association of epsin with ubiquitinated cargo along the endocytic pathway is negatively regulated by its interaction with clathrin. Proc Natl Acad Sci U S A *102*, 2766-2771.

Chen, H., Ko, G., Zatti, A., Di Giacomo, G., Liu, L., Raiteri, E., Perucco, E., Collesi, C., Min, W., Zeiss, C., et al. (2009). Embryonic arrest at midgestation and disruption of Notch signaling produced by the absence of both epsin 1 and epsin 2 in mice. Proc Natl Acad Sci U S A *106*, 13838-13843.

Chen, Y., Yang, M., Huang, W., Chen, W., Zhao, Y., Schulte, M.L., Volberding, P., Gerbec, Z., Zimmermann, M.T., Zeighami, A., et al. (2019). Mitochondrial Metabolic Reprogramming by CD36 Signaling Drives Macrophage Inflammatory Responses. Circ Res *125*, 1087-1102.

Csikos, G., Lippai, M., Lukacsovich, T., Juhasz, G., Henn, L., Erdelyi, M., Maroy, P., and Sass, M. (2009). A novel role for the Drosophila epsin (lqf): involvement in autophagy. Autophagy *5*, 636-648.

Cui, K., Dong, Y., Wang, B., Cowan, D.B., Chan, S.L., Shyy, J., and Chen, H. (2020). Endocytic Adaptors in Cardiovascular Disease. Front Cell Dev Biol *8*, 624159.

Cui, K., Podolnikova, N.P., Bailey, W., Szmuc, E., Podrez, E.A., Byzova, T.V., and Yakubenko, V.P. (2019). Inhibition of integrin alphaDbeta2-mediated macrophage adhesion to end product of docosahexaenoic acid (DHA) oxidation prevents macrophage accumulation during inflammation. J Biol Chem *294*, 14370-14382.

De Benedetti, F., Gattorno, M., Anton, J., Ben-Chetrit, E., Frenkel, J., Hoffman, H.M., Kone-Paut, I., Lachmann, H.J., Ozen, S., Simon, A., et al. (2018). Canakinumab for the Treatment of Autoinflammatory Recurrent Fever Syndromes. N Engl J Med *378*, 1908-1919.

De Camilli, P., Chen, H., Hyman, J., Panepucci, E., Bateman, A., and Brunger, A.T. (2002). The ENTH domain. FEBS Lett *513*, 11-18.
Dobin, A., Davis, C.A., Schlesinger, F., Drenkow, J., Zaleski, C., Jha, S., Batut, P., Chaisson, M., and Gingeras, T.R. (2013). STAR: ultrafast universal RNA-seq aligner. Bioinformatics *29*, 15-21.
Dong, Y., Lee, Y., Cui, K., He, M., Wang, B., Bhattacharjee, S., Zhu, B., Yago, T., Zhang, K., Deng, L., et al. (2020). Epsin-mediated degradation of IP3R1 fuels atherosclerosis. Nat Commun *11*, 3984.
Dong, Y., Wang, B., Cui, K., Cai, X., Bhattacharjee, S., Wong, S., Cowan, D.B., and Chen, H. (2021). Epsins Negatively Regulate Aortic Endothelial Cell Function by Augmenting Inflammatory Signaling. Cells *10*.
Doring, Y. (2015). Not growth but death: GM-CSF/IL-23 axis drives atherosclerotic plaque vulnerability by enhancing macrophage and DC apoptosis. Circ Res *116*, 222-224.
Edgar, R., Domrachev, M., and Lash, A.E. (2002). Gene Expression Omnibus: NCBI gene expression and hybridization array data repository. Nucleic Acids Res *30*, 207-210.
Escola-Gil, J.C., Lee-Rueckert, M., Santos, D., Cedo, L., Blanco-Vaca, F., and Julve, J. (2015). Quantification of In Vitro Macrophage Cholesterol Efflux and In Vivo Macrophage-Specific Reverse Cholesterol Transport. Methods Mol Biol *1339*, 211-233.
Evans, T.D., Sergin, I., Zhang, X., and Razani, B. (2017). Target acquired: Selective autophagy in cardiometabolic disease. Sci Signal *10*.
Febbraio, M., Podrez, E.A., Smith, J.D., Hajjar, D.P., Hazen, S.L., Hoff, H.F., Sharma, K., and Silverstein, R.L. (2000). Targeted disruption of the class B scavenger receptor CD36 protects against atherosclerotic lesion development in mice. J Clin Invest *105*, 1049-1056.
Feingold, K.R. (2000). Cholesterol Lowering Drugs. In Endotext. K.R. Feingold, B. Anawalt, A. Boyce, G. Chrousos, W.W. de Herder, K. Dhatariya, K. Dungan, J.M. Hershman, J. Hofland, S. Kalra, et al., eds. (South Dartmouth (MA)).
Fitzgerald, K., White, S., Borodovsky, A., Bettencourt, B.R., Strahs, A., Clausen, V., Wijngaard, P., Horton, J.D., Taubel, J., Brooks, A., et al. (2017). A Highly Durable RNAi Therapeutic Inhibitor of PCSK9. N Engl J Med *376*, 41-51.
Gerlach, B.D., Ampomah, P.B., Yurdagul, A., Jr., Liu, C., Lauring, M.C., Wang, X., Kasikara, C., Kong, N., Shi, J., Tao, W., et al. (2021). Efferocytosis induces macrophage proliferation to help resolve tissue injury. Cell Metab *33*, 2445-2463 e2448.
German, C.A., and Shapiro, M.D. (2020). Small Interfering RNA Therapeutic Inclisiran: A New Approach to Targeting PCSK9. BioDrugs *34*, 1-9.
Glass, C.K., and Witztum, J.L. (2001). Atherosclerosis. the road ahead. Cell *104*, 503-516.
Hansson, G.K., Libby, P., and Tabas, I. (2015). Inflammation and plaque vulnerability. J Intern Med *278*, 483-493.
Hewing, B., Moore, K.J., and Fisher, E.A. (2012). HDL and cardiovascular risk: time to call the plumber? Circ Res *111*, 1117-1120.
Itoh, T., Koshiba, S., Kigawa, T., Kikuchi, A., Yokoyama, S., and Takenawa, T. (2001). Role of the ENTH domain in phosphatidylinositol-4,5-bisphosphate binding and endocytosis. Science *291*, 1047-1051.
Johnson, W.E., Li, C., and Rabinovic, A. (2007). Adjusting batch effects in microarray expression data using empirical Bayes methods. Biostatistics *8*, 118-127.
Josefs, T., Basu, D., Vaisar, T., Arets, B., Kanter, J.E., Huggins, L.A., Hu, Y., Liu, J., Clouet-Foraison, N., Heinecke, J.W., et al. (2021). Atherosclerosis Regression and Cholesterol Efflux in Hypertriglyceridemic Mice. Circ Res *128*, 690-705.
Keene, D., Price, C., Shun-Shin, M.J., and Francis, D.P. (2014). Effect on cardiovascular risk of high density lipoprotein targeted drug treatments niacin, fibrates, and CETP inhibitors: meta-analysis of randomised controlled trials including 117,411 patients. BMJ *349*, g4379.
Kennedy, M.A., Barrera, G.C., Nakamura, K., Baldan, A., Tarr, P., Fishbein, M.C., Frank, J., Francone, O.L., and Edwards, P.A. (2005). ABCG1 has a critical role in mediating cholesterol efflux to HDL and preventing cellular lipid accumulation. Cell Metab *1*, 121-131.
Khera, A.V., Cuchel, M., de la Llera-Moya, M., Rodrigues, A., Burke, M.F., Jafri, K., French, B.C., Phillips, J.A., Mucksavage, M.L., Wilensky, R.L., et al. (2011). Cholesterol efflux capacity, high-density lipoprotein function, and atherosclerosis. N Engl J Med *364*, 127-135.
Kim, D., Pertea, G., Trapnell, C., Pimentel, H., Kelley, R., and Salzberg, S.L. (2013). TopHat2: accurate alignment of transcriptomes in the presence of insertions, deletions and gene fusions. Genome Biol *14*, R36.
Kim, K., Shim, D., Lee, J.S., Zaitsev, K., Williams, J.W., Kim, K.W., Jang, M.Y., Seok Jang, H., Yun, T.J., Lee, S.H., et al. (2018). Transcriptome Analysis Reveals Nonfoamy Rather Than Foamy Plaque Macrophages Are Proinflammatory in Atherosclerotic Murine Models. Circ Res *123*, 1127-1142.

Kojima, Y., Weissman, I.L., and Leeper, N.J. (2017). The Role of Efferocytosis in Atherosclerosis. Circulation *135*, 476-489.
Kunjathoor, V.V., Febbraio, M., Podrez, E.A., Moore, K.J., Andersson, L., Koehn, S., Rhee, J.S., Silverstein, R., Hoff, H.F., and Freeman, M.W. (2002). Scavenger receptors class A-I/II and CD36 are the principal receptors responsible for the uptake of modified low density lipoprotein leading to lipid loading in macrophages. J Biol Chem *277*, 49982-49988.
Le Guezennec, X., Brichkina, A., Huang, Y.F., Kostromina, E., Han, W., and Bulavin, D.V. (2012). Wip1-dependent regulation of autophagy, obesity, and atherosclerosis. Cell Metab *16*, 68-80.
Libby, P. (2012). Inflammation in atherosclerosis. Arterioscler Thromb Vasc Biol *32*, 2045-2051.
Liu, X., Pasula, S., Song, H., Tessneer, K.L., Dong, Y., Hahn, S., Yago, T., Brophy, M.L., Chang, B., Cai, X., et al. (2014). Temporal and spatial regulation of epsin abundance and VEGFR3 signaling are required for lymphatic valve formation and function. Sci Signal *7*, ra97.
Love, M.I., Huber, W., and Anders, S. (2014). Moderated estimation of fold change and dispersion for RNA-seq data with DESeq2. Genome Biol *15*, 550.
Lund, E.G., Kerr, T.A., Sakai, J., Li, W.P., and Russell, D.W. (1998). cDNA cloning of mouse and human cholesterol 25-hydroxylases, polytopic membrane proteins that synthesize a potent oxysterol regulator of lipid metabolism. J Biol Chem *273*, 34316-34327.
Meyerson, M., and Harlow, E. (1994). Identification of G1 kinase activity for cdk6, a novel cyclin D partner. Mol Cell Biol *14*, 2077-2086.
Moore, K.J., and Fisher, E.A. (2014). High-density lipoproteins put out the fire. Cell Metab *19*, 175-176.
Moore, K.J., and Freeman, M.W. (2006). Scavenger receptors in atherosclerosis: beyond lipid uptake. Arterioscler Thromb Vasc Biol *26*, 1702-1711.
Moore, K.J., Sheedy, F.J., and Fisher, E.A. (2013). Macrophages in atherosclerosis: a dynamic balance. Nat Rev Immunol *13*, 709-721.
Mootha, V.K., Lindgren, C.M., Eriksson, K.F., Subramanian, A., Sihag, S., Lehar, J., Puigserver, P., Carlsson, E., Ridderstrale, M., Laurila, E., et al. (2003). PGC-1alpha-responsive genes involved in oxidative phosphorylation are coordinately downregulated in human diabetes. Nat Genet *34*, 267-273.
Nicholls, S.J., Puri, R., Ballantyne, C.M., Jukema, J.W., Kastelein, J.J.P., Koenig, W., Wright, R.S., Kallend, D., Wijngaard, P., Borgman, M., et al. (2018). Effect of Infusion of High-Density Lipoprotein Mimetic Containing Recombinant Apolipoprotein A-I Milano on Coronary Disease in Patients With an Acute Coronary Syndrome in the MILANO-PILOT Trial: A Randomized Clinical Trial. JAMA Cardiol *3*, 806-814.
Nozaki, S., Kashiwagi, H., Yamashita, S., Nakagawa, T., Kostner, B., Tomiyama, Y., Nakata, A., Ishigami, M., Miyagawa, J., Kameda-Takemura, K., et al. (1995). Reduced uptake of oxidized low density lipoproteins in monocyte-derived macrophages from CD36-deficient subjects. J Clin Invest *96*, 1859-1865.
Ohashi, R., Mu, H., Wang, X., Yao, Q., and Chen, C. (2005). Reverse cholesterol transport and cholesterol efflux in atherosclerosis. QJM *98*, 845-856.
Oppi, S., Luscher, T.F., and Stein, S. (2019). Mouse Models for Atherosclerosis Research-Which Is My Line? Front Cardiovasc Med *6*, 46.
Ouimet, M., Barrett, T.J., and Fisher, E.A. (2019). HDL and Reverse Cholesterol Transport. Circ Res *124*, 1505-1518.
Ouimet, M., Ediriweera, H., Afonso, M.S., Ramkhelawon, B., Singaravelu, R., Liao, X., Bandler, R.C., Rahman, K., Fisher, E.A., Rayner, K.J., et al. (2017). microRNA-33 Regulates Macrophage Autophagy in Atherosclerosis. Arterioscler Thromb Vasc Biol *37*, 1058-1067.
Ouimet, M., Franklin, V., Mak, E., Liao, X., Tabas, I., and Marcel, Y.L. (2011). Autophagy regulates cholesterol efflux from macrophage foam cells via lysosomal acid lipase. Cell Metab *13*, 655-667.
Pasula, S., Cai, X., Dong, Y., Messa, M., McManus, J., Chang, B., Liu, X., Zhu, H., Mansat, R.S., Yoon, S.J., et al. (2012). Endothelial epsin deficiency decreases tumor growth by enhancing VEGF signaling. J Clin Invest *122*, 4424-4438.
Podrez, E.A., Febbraio, M., Sheibani, N., Schmitt, D., Silverstein, R.L., Hajjar, D.P., Cohen, P.A., Frazier, W.A., Hoff, H.F., and Hazen, S.L. (2000). Macrophage scavenger receptor CD36 is the major receptor for LDL modified by monocyte-generated reactive nitrogen species. J Clin Invest *105*, 1095-1108.
Polo, S., Sigismund, S., Faretta, M., Guidi, M., Capua, M.R., Bossi, G., Chen, H., De Camilli, P., and Di Fiore, P.P. (2002). A single motif responsible for ubiquitin recognition and monoubiquitination in endocytic proteins. Nature *416*, 451-455.

Purcell-Huynh, D.A., Farese, R.V., Jr., Johnson, D.F., Flynn, L.M., Pierotti, V., Newland, D.L., Linton, M.F., Sanan, D.A., and Young, S.G. (1995). Transgenic mice expressing high levels of human apolipoprotein B develop severe atherosclerotic lesions in response to a high-fat diet. J Clin Invest *95*, 2246-2257.

Razani, B., Feng, C., Coleman, T., Emanuel, R., Wen, H., Hwang, S., Ting, J.P., Virgin, H.W., Kastan, M.B., and Semenkovich, C.F. (2012). Autophagy links inflammasomes to atherosclerotic progression. Cell Metab *15*, 534-544.

Ridker, P.M., Everett, B.M., Thuren, T., MacFadyen, J.G., Chang, W.H., Ballantyne, C., Fonseca, F., Nicolau, J., Koenig, W., Anker, S.D., et al. (2017). Antiinflammatory Therapy with Canakinumab for Atherosclerotic Disease. N Engl J Med *377*, 1119-1131.

Robinet, P., Wang, Z., Hazen, S.L., and Smith, J.D. (2010). A simple and sensitive enzymatic method for cholesterol quantification in macrophages and foam cells. J Lipid Res *51*, 3364-3369.

Robinson, M.D., McCarthy, D.J., and Smyth, G.K. (2010). edgeR: a Bioconductor package for differential expression analysis of digital gene expression data. Bioinformatics *26*, 139-140.

Rohatgi, A., Khera, A., Berry, J.D., Givens, E.G., Ayers, C.R., Wedin, K.E., Neeland, I.J., Yuhanna, I.S., Rader, D.R., de Lemos, J.A., et al. (2014). HDL cholesterol efflux capacity and incident cardiovascular events. N Engl J Med *371*, 2383-2393.

Rosenthal, J.A., Chen, H., Slepnev, V.I., Pellegrini, L., Salcini, A.E., Di Fiore, P.P., and De Camilli, P. (1999). The epsins define a family of proteins that interact with components of the clathrin coat and contain a new protein module. J Biol Chem *274*, 33959-33965.

Sag, D., Cekic, C., Wu, R., Linden, J., and Hedrick, C.C. (2015). The cholesterol transporter ABCG1 links cholesterol homeostasis and tumour immunity. Nat Commun *6*, 6354.

Sankaranarayanan, S., Kellner-Weibel, G., de la Llera-Moya, M., Phillips, M.C., Asztalos, B.F., Bittman, R., and Rothblat, G.H. (2011). A sensitive assay for ABCA1-mediated cholesterol efflux using BODIPY-cholesterol. J Lipid Res *52*, 2332-2340.

Sergin, I., Evans, T.D., Zhang, X., Bhattacharya, S., Stokes, C.J., Song, E., Ali, S., Dehestani, B., Holloway, K.B., Micevych, P.S., et al. (2017). Exploiting macrophage autophagy-lysosomal biogenesis as a therapy for atherosclerosis. Nat Commun *8*, 15750.

Sharma, M., Schlegel, M.P., Afonso, M.S., Brown, E.J., Rahman, K., Weinstock, A., Sansbury, B.E., Corr, E.M., van Solingen, C., Koelwyn, G.J., et al. (2020). Regulatory T Cells License Macrophage Pro-Resolving Functions During Atherosclerosis Regression. Circ Res *127*, 335-353.

Shih, S.C., Katzmann, D.J., Schnell, J.D., Sutanto, M., Emr, S.D., and Hicke, L. (2002). Epsins and Vps27p/Hrs contain ubiquitin-binding domains that function in receptor endocytosis. Nat Cell Biol *4*, 389-393.

Silvain, J., Kerneis, M., Guerin, M., and Montalescot, G. (2019). Modulation of cholesterol efflux capacity in patients with myocardial infarction. Curr Opin Cardiol *34*, 714-720.

Spangenburg, E.E., Pratt, S.J.P., Wohlers, L.M., and Lovering, R.M. (2011). Use of BODIPY (493/503) to visualize intramuscular lipid droplets in skeletal muscle. J Biomed Biotechnol *2011*, 598358.

Steinberg, D. (2009). The LDL modification hypothesis of atherogenesis: an update. J Lipid Res *50 Suppl*, S376-381.

Subramanian, A., Tamayo, P., Mootha, V.K., Mukherjee, S., Ebert, B.L., Gillette, M.A., Paulovich, A., Pomeroy, S.L., Golub, T.R., Lander, E.S., et al. (2005). Gene set enrichment analysis: a knowledge-based approach for interpreting genome-wide expression profiles. Proc Natl Acad Sci U S A *102*, 15545-15550.

Tao, H., Yancey, P.G., Blakemore, J.L., Zhang, Y., Ding, L., Jerome, W.G., Brown, J.D., Vickers, K.C., and Linton, M.F. (2021). Macrophage SR-BI modulates autophagy via VPS34 complex and PPARalpha transcription of Tfeb in atherosclerosis. J Clin Invest *131*.

Tao, W., Yurdagul, A., Jr., Kong, N., Li, W., Wang, X., Doran, A.C., Feng, C., Wang, J., Islam, M.A., Farokhzad, O.C., et al. (2020). siRNA nanoparticles targeting CaMKIIgamma in lesional macrophages improve atherosclerotic plaque stability in mice. Sci Transl Med *12*.

Tardif, J.C., Gregoire, J., L'Allier, P.L., Ibrahim, R., Lesperance, J., Heinonen, T.M., Kouz, S., Berry, C., Basser, R., Lavoie, M.A., et al. (2007). Effects of reconstituted high-density lipoprotein infusions on coronary atherosclerosis: a randomized controlled trial. JAMA *297*, 1675-1682.

Tarling, E.J., and Edwards, P.A. (2011). ATP binding cassette transporter G1 (ABCG1) is an intracellular sterol transporter. Proc Natl Acad Sci U S A *108*, 19719-19724.

Tessneer, K.L., Pasula, S., Cai, X., Dong, Y., McManus, J., Liu, X., Yu, L., Hahn, S., Chang, B., Chen, Y., et al. (2014). Genetic reduction of vascular endothelial growth factor receptor 2 rescues aberrant angiogenesis caused by epsin deficiency. Arterioscler Thromb Vasc Biol *34*, 331-337.

Thorp, E., Cui, D., Schrijvers, D.M., Kuriakose, G., and Tabas, I. (2008). Mertk receptor mutation reduces efferocytosis efficiency and promotes apoptotic cell accumulation and plaque necrosis in atherosclerotic lesions of apoe-/- mice. Arterioscler Thromb Vasc Biol *28*, 1421-1428.

Van Eck, M., Bos, I.S., Hildebrand, R.B., Van Rij, B.T., and Van Berkel, T.J. (2004). Dual role for scavenger receptor class B, type I on bone marrow-derived cells in atherosclerotic lesion development. Am J Pathol *165*, 785-794.

Virmani, R., Burke, A.P., Farb, A., and Kolodgie, F.D. (2006). Pathology of the vulnerable plaque. J Am Coll Cardiol *47*, C13-18.

Wang, N., Ranalletta, M., Matsuura, F., Peng, F., and Tall, A.R. (2006). LXR-induced redistribution of ABCG1 to plasma membrane in macrophages enhances cholesterol mass efflux to HDL. Arterioscler Thromb Vasc Biol *26*, 1310-1316.

Wang, Y., Nanda, V., Direnzo, D., Ye, J., Xiao, S., Kojima, Y., Howe, K.L., Jarr, K.U., Flores, A.M., Tsantilas, P., et al. (2020). Clonally expanding smooth muscle cells promote atherosclerosis by escaping efferocytosis and activating the complement cascade. Proc Natl Acad Sci U S A *117*, 15818-15826.

Weber, C., and Noels, H. (2011). Atherosclerosis: current pathogenesis and therapeutic options. Nat Med *17*, 1410-1422.

Westerterp, M., Tsuchiya, K., Tattersall, I.W., Fotakis, P., Bochem, A.E., Molusky, M.M., Ntonga, V., Abramowicz, S., Parks, J.S., Welch, C.L., et al. (2016). Deficiency of ATP-Binding Cassette Transporters A1 and G1 in Endothelial Cells Accelerates Atherosclerosis in Mice. Arterioscler Thromb Vasc Biol *36*, 1328-1337.

Yu, G., Wang, L.G., Han, Y., and He, Q.Y. (2012). clusterProfiler: an R package for comparing biological themes among gene clusters. OMICS *16*, 284-287.

Yu, R., Park, J.S., Kawada, T., and Kwon, B.S. (2002). Alteration of a macrophages inflammatory protein-related protein-2 (MRP-2) response by high fat and cholesterol diet in mice. Life Sci *70*, 2535-2545.

Yvan-Charvet, L., Ranalletta, M., Wang, N., Han, S., Terasaka, N., Li, R., Welch, C., and Tall, A.R. (2007). Combined deficiency of ABCA1 and ABCG1 promotes foam cell accumulation and accelerates atherosclerosis in mice. J Clin Invest *117*, 3900-3908.

Zhu, X., Xu, Y., Solis, L.M., Tao, W., Wang, L., Behrens, C., Xu, X., Zhao, L., Liu, D., Wu, J., et al. (2015). Long-circulating siRNA nanoparticles for validating Prohibitin1-targeted non-small cell lung cancer treatment. Proc Natl Acad Sci U S A *112*, 7779-7784.

Figure 1

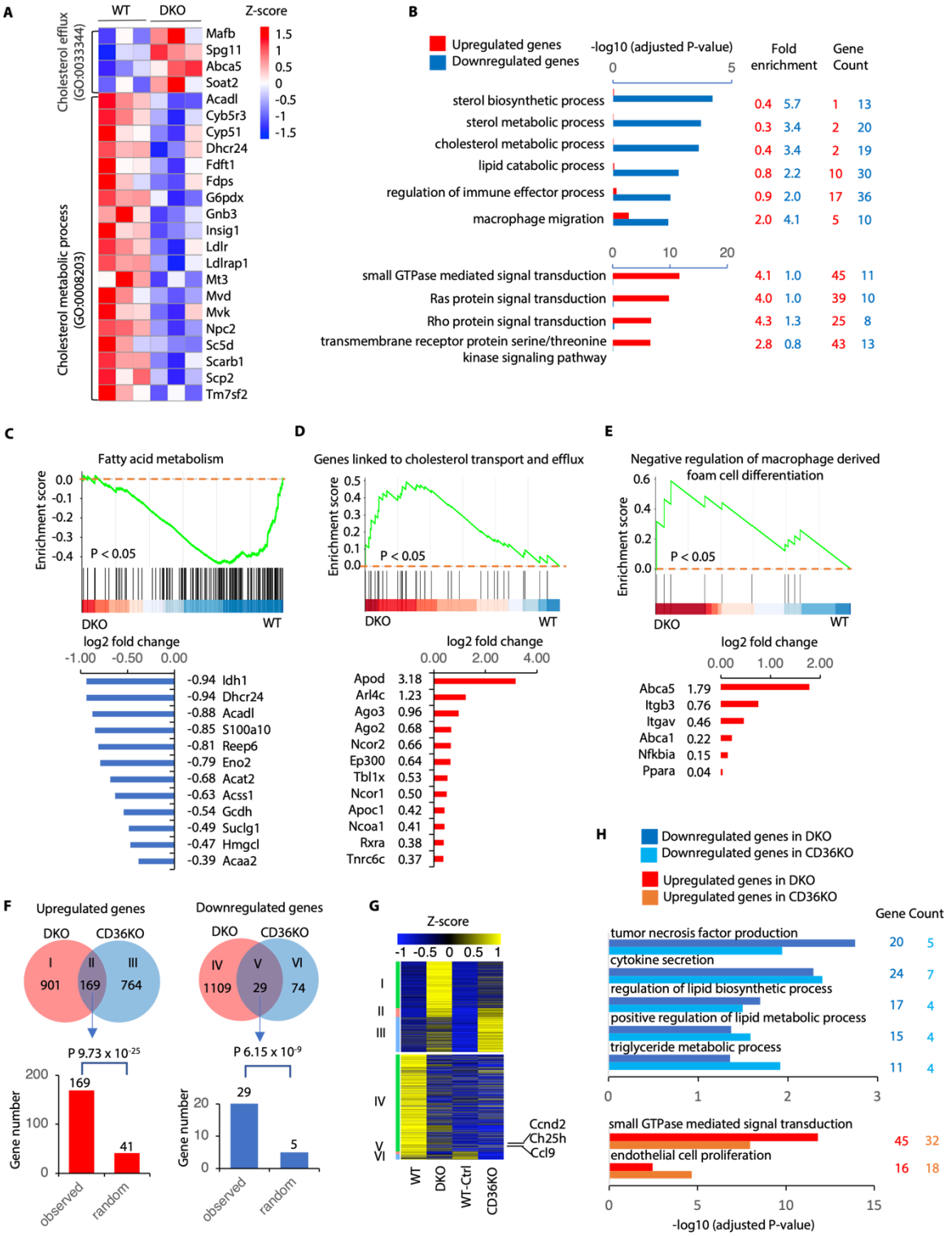
A
WT
DKO
Z-score
Cholesterol efflux (GO:0033344)
Cholesterol metabolic process (GO:0008203)
Mafb
Spg11
Abca5
Soat2
Acadl
Cyb5r3
Cyp51
Dhcr24
Fdft1
Fdps
G6pdx
Gnb3
Insig1
Ldlr
Ldlrap1
Mt3
Mvd
Mvk
Npc2
Sc5d
Scarb1
Scp2
Tm7sf2
B
Upregulated genes
Downregulated genes
-log10 (adjusted P-value)
Fold enrichment
Gene Count
sterol biosynthetic process
sterol metabolic process
cholesterol metabolic process
lipid catabolic process
regulation of immune effector process
macrophage migration
small GTPase mediated signal transduction
Ras protein signal transduction
Rho protein signal transduction
transmembrane receptor protein serine/threonine kinase signaling pathway
C
Fatty acid metabolism
Enrichment score
P < 0.05
DKO
WT
log2 fold change
-0.94 Idh1
-0.94 Dhcr24
-0.88 Acadl
-0.85 S100a10
-0.81 Reep6
-0.79 Eno2
-0.68 Acat2
-0.63 Acss1
-0.54 Gcdh
-0.49 Suclg1
-0.47 Hmgcl
-0.39 Acaa2
D
Genes linked to cholesterol transport and efflux
Apod 3.18
Arl4c 1.23
Ago3 0.96
Ago2 0.68
Ncor2 0.66
Ep300 0.64
Tbl1x 0.53
Ncor1 0.50
Apoc1 0.42
Ncoa1 0.41
Rxra 0.38
Tnrc6c 0.37
E
Negative regulation of macrophage derived foam cell differentiation
Abca5 1.79
Itgb3 0.76
Itgav 0.46
Abca1 0.22
Nfkbia 0.15
Ppara 0.04
F
Upregulated genes
Downregulated genes
DKO
CD36KO
I 901
II 169
III 764
IV 1109
V 29
VI 74
P 9.73 x 10-25
P 6.15 x 10-9
Gene number
observed
random
G
Z-score
Ccnd2
Ch25h
Ccl9
WT
DKO
WT-Ctrl
CD36KO
H
Downregulated genes in DKO
Downregulated genes in CD36KO
Upregulated genes in DKO
Upregulated genes in CD36KO
Gene Count
tumor necrosis factor production
cytokine secretion
regulation of lipid biosynthetic process
positive regulation of lipid metabolic process
triglyceride metabolic process
small GTPase mediated signal transduction
endothelial cell proliferation
-log10 (adjusted P-value)

739

Fig. 1. RNA-seq analysis of WT and DKO macrophages reveals that Epsins regulate lipid cholesterol metabolism and efflux pathways. (**A**) A heatmap showing the expression of genes involved in the cholesterol metabolic process (GO:0008203) and cholesterol efflux (GO:0033344). (**B)** Gene Ontology (GO) enrichment analysis for up- and down-regulated genes in Epsin deficient (DKO) macrophages relative to WT. (**C-E**) GSEA demonstrated the tendency of individual pathways to be up- or down- regulated in Epsin deficient macrophages compared to wild type (top panels). The bar plots (bottom panels) showing log2 fold change of altered genes in these pathways. (**F**) Venn diagrams (top panels) showing the number of overlapping up- and down-regulated genes in DKO and CD36 knockout (CD36KO) samples. Bar plots (bottom panels) showing the observed numbers of overlapped genes versus numbers expected by random chance. The P-value was calculated using two tail Fisher exact test. (**G**) Heatmap of expression values of up and down regulated genes in DKO and CD36KO macrophages. Genes were grouped as indicated in the Venn diagrams. WT, wild type for DKO; WT-Ctrl, wild type for CD36KO. (**H**) The Gene Ontology (GO) enrichment analysis for shared down regulated (top) and up regulated genes (bottom) between DKO and CD36KO macrophages. Benjamini corrected P-values are indicated on the x-axis (B, H).

Figure 2

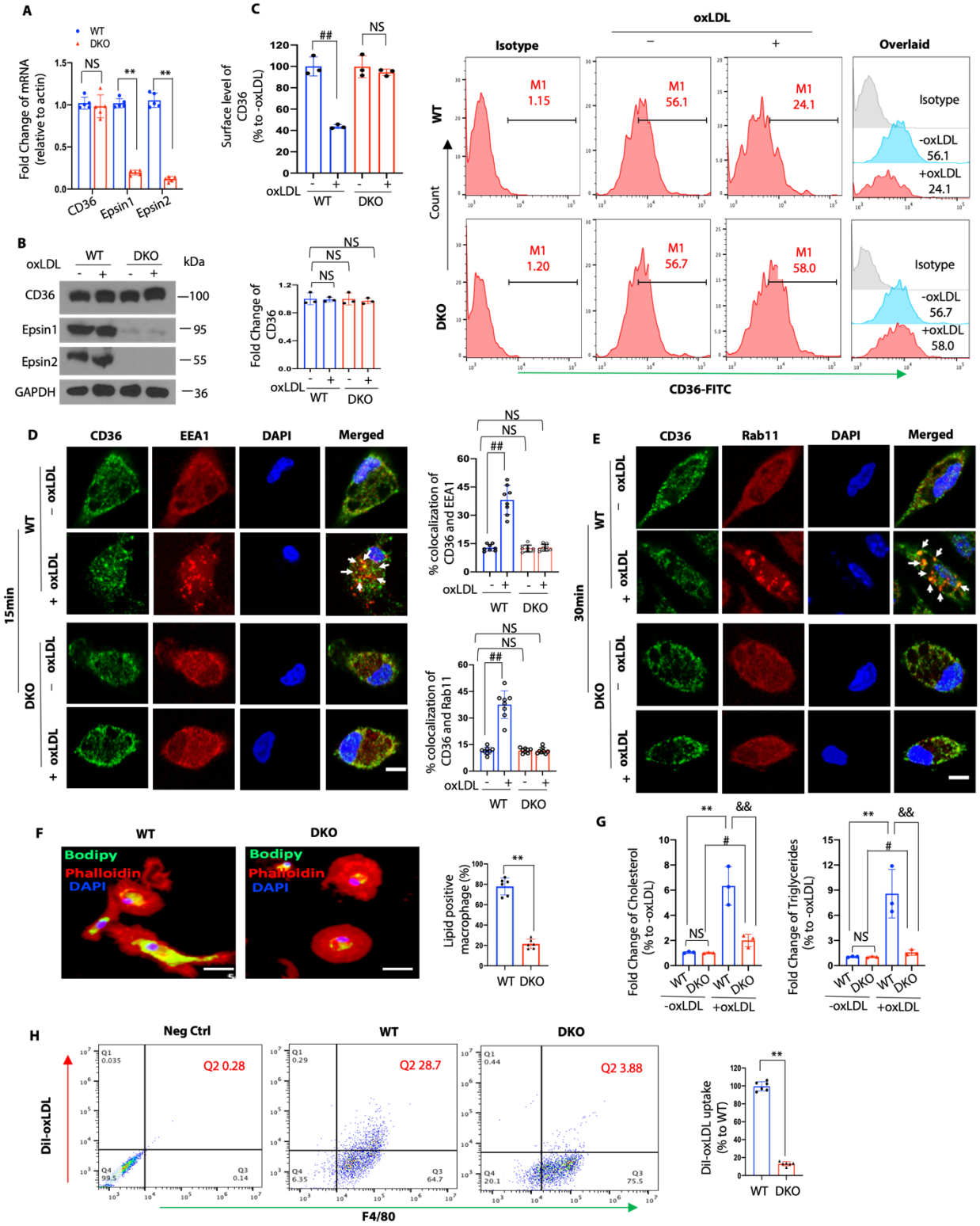
A
WT
DKO
Fold Change of mRNA (relative to actin)
NS
**
**
CD36
Epsin1
Epsin2
B
oxLDL
WT
DKO
kDa
CD36
Epsin1
Epsin2
GAPDH
100
95
55
36
C
Surface level of CD36 (% to -oxLDL)
##
NS
oxLDL
WT
DKO
Fold Change of CD36
NS
NS
NS
oxLDL
WT
DKO
oxLDL
Isotype
Overlaid
M1 1.15
M1 56.1
M1 24.1
M1 1.20
M1 56.7
M1 58.0
Isotype
-oxLDL 56.1
+oxLDL 24.1
Isotype
-oxLDL 56.7
+oxLDL 58.0
Count
CD36-FITC
D
CD36
EEA1
DAPI
Merged
15min
WT
DKO
– oxLDL
+ oxLDL
% colocalization of CD36 and EEA1
% colocalization of CD36 and Rab11
E
CD36
Rab11
DAPI
Merged
30min
F
WT
DKO
Bodipy
Phalloidin
DAPI
Lipid positive macrophage (%)
G
Fold Change of Cholesterol (% to -oxLDL)
Fold Change of Triglycerides (% to -oxLDL)
-oxLDL
+oxLDL
H
Neg Ctrl
WT
DKO
Dil-oxLDL
F4/80
Q2 0.28
Q2 28.7
Q2 3.88
Dil-oxLDL uptake (% to WT)

759

Fig. 2. Epsin facilitates CD36-mediated lipid uptake by promoting CD36 endocytosis and recycling. (**A-C**) Bone marrow derived macrophages (BMDM) or thioglycolate induced peritoneal macrophages from WT (n=5) and DKO (n=5) mice were incubated in lipid-deficient medium for 24h and treated with or without 100μg/mL oxLDL for 1h at 37^0C. qRT-PCR analysis of CD36 expression (A), western blot (WB) analysis for total protein level of CD36 (B) and flow cytometry for surface level of CD36 (C). NS, no significant difference; **WT vs DKO group, P<0.01; $^{\#\#}$-oxLDL vs +oxLDL group, P<0.01. (**D-E**) Elicited WT and DKO macrophages were incubated in lipid-deficient medium for 24h and treated with or without 100μg/mL oxLDL for 15min (D) or 30min (E) at 37^0C. Macrophages were co-stained with CD36 (green), the early endosome marker EEA1 (red) or the recycling endosome marker Rab11 (Red) and DAPI (bule), and imaged using confocal microscope. White arrows indicate the endocytic vesicles, scale bar=5μm, $^{\#\#}$-oxLDL vs +oxLDL group (n=8), P<0.01. (**F**) BODIPY staining of peritoneal macrophages pre-incubated with 25μg/mL oxLDL for 24h in lipid-deficient medium, **WT vs DKO group (n=6), P<0.01, scale bar=10μm. (**G**) Cholesterol and triglycerides levels in WT and DKO macrophages treated with 25μg/mL oxLDL for 24h in lipid-deficient medium (n=3). **-oxLDL (WT) vs +oxLDL (WT), P<0.01; $^{\#}$-oxLDL (DKO) vs +oxLDL (DKO), P<0.05; $^{\&\&}$ +oxLDL (WT) vs +oxLDL (DKO), P<0.01. (**H**) Macrophages isolated from WT and DKO mice were incubated in lipid-deficient medium for 24h followed by the treatment with DiI-oxLDL for 2h at 37^0C to assess the lipoprotein uptake by flow cytometry, **WT vs DKO group (n=6), P<0.01. Data from A-H are presented as mean ± SD and were analyzed using either unpaired Student's t-test (two groups) or one-way ANOVA (multiple comparisons).

Figure 3

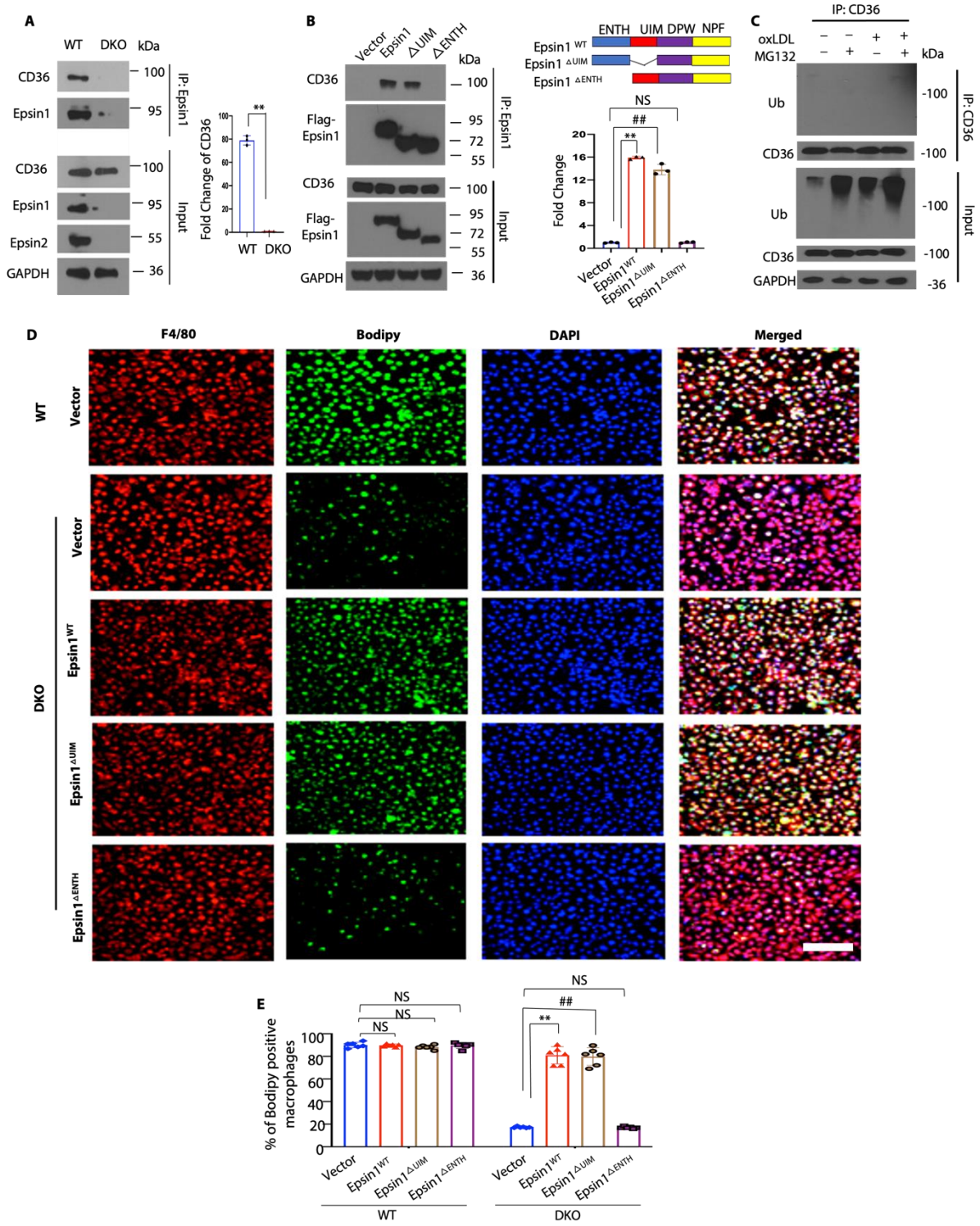
A
WT DKO kDa
CD36
Epsin1
Epsin2
GAPDH
IP: Epsin1
Input
Fold Change of CD36
B
Vector Epsin1 ΔUIM ΔENTH
Flag-Epsin1
ENTH UIM DPW NPF
Epsin1 WT
Epsin1 ΔUIM
Epsin1 ΔENTH
Fold Change
C
IP: CD36
oxLDL
MG132
Ub
D
F4/80
Bodipy
DAPI
Merged
WT
DKO
Vector
Epsin1WT
Epsin1ΔUIM
Epsin1ΔENTH
E
% of Bodipy positive macrophages
NS
##
**

Fig. 3. Epsin interacts with CD36 via Epsin-ENTH domain which is critical for CD36-mediated lipid uptake and foam cell formation. (**A**) BMDM or peritoneal macrophages isolated from WT and DKO mice were incubated in lipid-deficient medium for 24h followed by the treatment with 100μg/mL oxLDL for 1h, IP and WB analysis of Epsin1 and CD36 (n=3, **WT vs DKO, P<0.01). (**B**) CD36 plasmids and full length (FLAG-Epsin1^{WT}) or domain-deletion constructs (FLAG-Epsin1$^{\triangle ENTH}$ or FLAG-Epsin1$^{\triangle UIM}$) in the pcDNA3 vector were transfected into HEK 293T cells for 48 h and then treated with 100μg/mL oxLDL for 1h, followed by immunoprecipitation (IP) and WB analysis using antibodies against FLAG tags and CD36 (n=3, **Epsin1^{WT} vs vector group, P<0.01; $^{\#\#}$Epsin1$^{\triangle UIM}$ vs vector group, P<0.01). (**C**) Peritoneal macrophages isolated from WT mice were incubated in lipid-deficient medium for 24h followed by treatment with 5 μM MG132 for 3h. Cells were subsequently treated with 100 μg/mL oxLDL for 1h followed by IP and WB for ubiquitin and CD36. (**D**) FLAG-Epsin1^{WT}, FLAG-Epsin1$^{\triangle ENTH}$, and FLAG-Epsin1$^{\triangle UIM}$ constructs were transfected into DKO macrophages for 48 h and treated with 100μg/mL oxLDL for 1 h, followed by staining with F4/80 (red), BODIPY (green) and DAPI (blue). Scale bar= 200μm. (**E**) Statistics for (D and Fig. S6), n=6, **Epsin1 ^{WT} vs vector group, P<0.01; $^{\#\#}$Epsin1$^{\triangle UIM}$ vs vector group, P<0.01. Data from A-D are presented as mean ± SD and were analyzed using either unpaired Student's t-test (two groups) or one-way ANOVA (multiple comparisons).

Figure 4

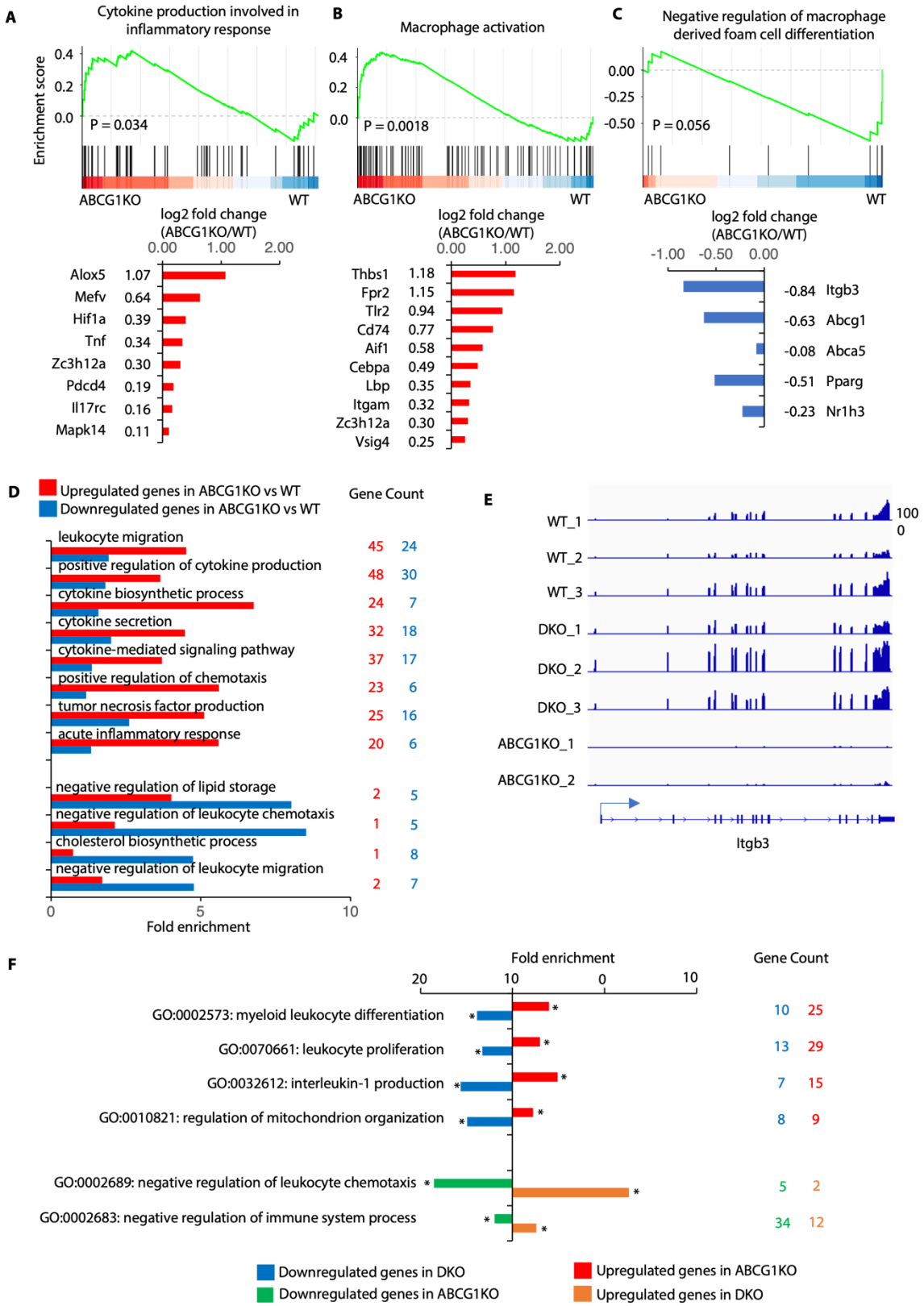
A
Cytokine production involved in inflammatory response
Enrichment score
P = 0.034
ABCG1KO
WT
log2 fold change (ABCG1KO/WT)
Alox5 1.07
Mefv 0.64
Hif1a 0.39
Tnf 0.34
Zc3h12a 0.30
Pdcd4 0.19
Il17rc 0.16
Mapk14 0.11
B
Macrophage activation
P = 0.0018
Thbs1 1.18
Fpr2 1.15
Tlr2 0.94
Cd74 0.77
Aif1 0.58
Cebpa 0.49
Lbp 0.35
Itgam 0.32
Zc3h12a 0.30
Vsig4 0.25
C
Negative regulation of macrophage derived foam cell differentiation
P = 0.056
-0.84 Itgb3
-0.63 Abcg1
-0.08 Abca5
-0.51 Pparg
-0.23 Nr1h3
D
Upregulated genes in ABCG1KO vs WT
Downregulated genes in ABCG1KO vs WT
Gene Count
leukocyte migration 45 24
positive regulation of cytokine production 48 30
cytokine biosynthetic process 24 7
cytokine secretion 32 18
cytokine-mediated signaling pathway 37 17
positive regulation of chemotaxis 23 6
tumor necrosis factor production 25 16
acute inflammatory response 20 6
negative regulation of lipid storage 2 5
negative regulation of leukocyte chemotaxis 1 5
cholesterol biosynthetic process 1 8
negative regulation of leukocyte migration 2 7
Fold enrichment
E
WT_1
WT_2
WT_3
DKO_1
DKO_2
DKO_3
ABCG1KO_1
ABCG1KO_2
Itgb3
F
Fold enrichment
Gene Count
GO:0002573: myeloid leukocyte differentiation 10 25
GO:0070661: leukocyte proliferation 13 29
GO:0032612: interleukin-1 production 7 15
GO:0010821: regulation of mitochondrion organization 8 9
GO:0002689: negative regulation of leukocyte chemotaxis 5 2
GO:0002683: negative regulation of immune system process 34 12
Downregulated genes in DKO
Downregulated genes in ABCG1KO
Upregulated genes in ABCG1KO
Upregulated genes in DKO

804

Fig. 4. RNA-seq analyses of WT, DKO and ABCG1 knockout (ABCG1KO) in macrophages indicate inversely regulation of lipid metabolism and inflammatory response. (**A-C**) The Gene Set Enrichment Analysis (GSEA) (top panels) indicates the tendency of individual pathways to be up or down regulated in ABCG1KO macrophages compared to wild type. Genes associated with cytokine production involved in the inflammatory response (A), macrophage activation (B), and negatively regulating macrophage derived foam cell differentiation (C) are analyzed. The Barplots (bottom panels) showing log2 fold changes of expression of altered genes. (**D**) GO enrichment analysis for up- and down- regulated genes in ABCG1KO relative to WT. (**E**) Genome browser tracks to show expression of Itgb3 in individual samples. (**F**) The GO enrichment analysis revealed pathways reversely regulated in ABCG1 knock out and Epsin deficient macrophages, compared to wild type. *P<0.05.

Figure 5

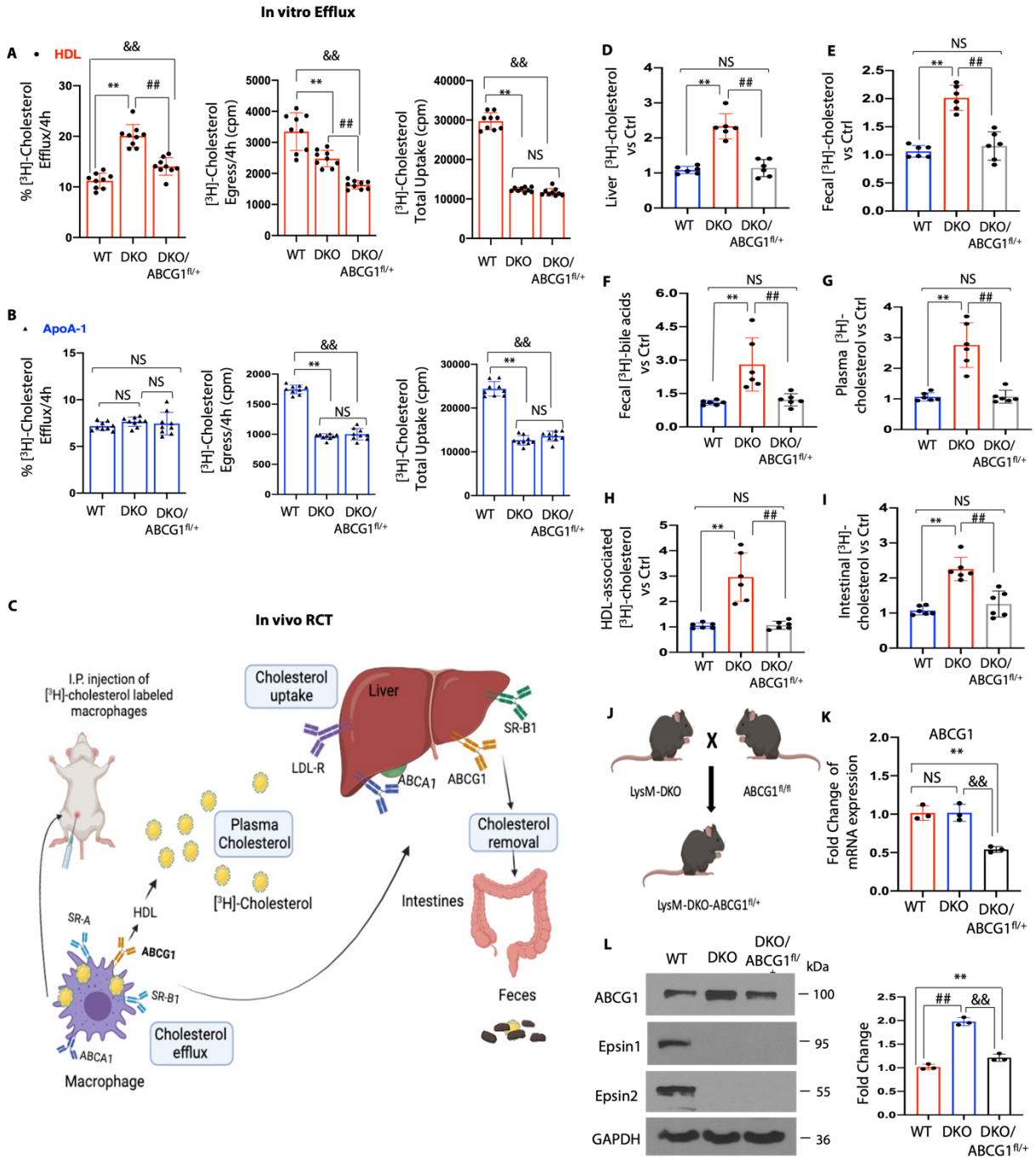
In vitro Efflux
A
HDL
% [3H]-Cholesterol Efflux/4h
[3H]-Cholesterol Egress/4h (cpm)
[3H]-Cholesterol Total Uptake (cpm)
WT
DKO
DKO/ABCG1fl/+
B
ApoA-1
C
In vivo RCT
I.P. injection of [3H]-cholesterol labeled macrophages
Cholesterol uptake
Liver
LDL-R
ABCA1
ABCG1
SR-B1
Plasma Cholesterol
[3H]-Cholesterol
HDL
SR-A
Cholesterol efflux
Macrophage
Cholesterol removal
Intestines
Feces
D
Liver [3H]-cholesterol vs Ctrl
E
Fecal [3H]-cholesterol vs Ctrl
F
Fecal [3H]-bile acids vs Ctrl
G
Plasma [3H]-cholesterol vs Ctrl
H
HDL-associated [3H]-cholesterol vs Ctrl
I
Intestinal [3H]-cholesterol vs Ctrl
J
LysM-DKO
ABCG1fl/fl
LysM-DKO-ABCG1fl/+
K
ABCG1
Fold Change of mRNA expression
L
kDa
ABCG1
Epsin1
Epsin2
GAPDH
Fold Change

Fig. 5. Epsins deficiency in macrophages shows increased cholesterol efflux *in vitro* and reverse cholesterol transport (RCT) *in vivo*. (**A-B**) Peritoneal macrophages were isolated from WT, DKO) and DKO/ABCG1$^{fl/+}$ mice. *In vitro* [^{3}H]-cholesterol labeled WT, DKO or DKO/ABCG1$^{fl/+}$ macrophages cholesterol efflux to 25μg/mL HDL and 10μg/mL ApoA-1 in the presence of 3μmol/L LXR agonist T0901317 were determined (n=9). **WT vs DKO, P<0.01; $^{\#\#}$DKO vs DKO/ABCG1$^{fl/+}$, P<0.01; $^{\&\&}$WT vs DKO/ABCG1$^{fl/+}$, P<0.01. (**C**) Schematic of [^{3}H]-cholesterol loaded macrophage-RCT pathway. WT, DKO or DKO/ABCG1$^{fl/+}$ macrophages were treated with 4μCi/mL [^{3}H]-cholesterol and 50μg/mL ac-LDL for 48h followed by the injection of radiolabeled foam cells to C57BL/6/WT mice. After 48h, blood, liver and feces were collected and measured using a scintillation counter. (**D-I**) Distribution of [^{3}H]-radioactivity counts in serum, HDL, liver feces and intestinal contents were determined by scintillation counter (n=6). **WT vs DKO, P<0.01; $^{\#\#}$DKO vs DKO/ABCG1$^{fl/+}$, P<0.01. (**J**) LysM-DKO mice were crossed with ABCG1$^{fl/fl}$ mice to generate LysM-DKO-ABCG1$^{fl/+}$ mice. (**K-L**) Peritoneal macrophages isolated from WT, LysM-DKO and LysM-DKO/ABCG1$^{fl/+}$ mice (n=6) were analyzed by qRT-PCR (K) and WB (L) (n≥3). **WT vs DKO/ABCG1$^{fl/+}$ group, P<0.01; $^{\#\#}$WT vs DKO group, P<0.01; $^{\&\&}$DKO vs DKO/ABCG1$^{fl/+}$ group, P<0.01. Data from A-L are presented as mean ± SD and were analyzed using one-way ANOVA (multiple comparisons).

Figure 6

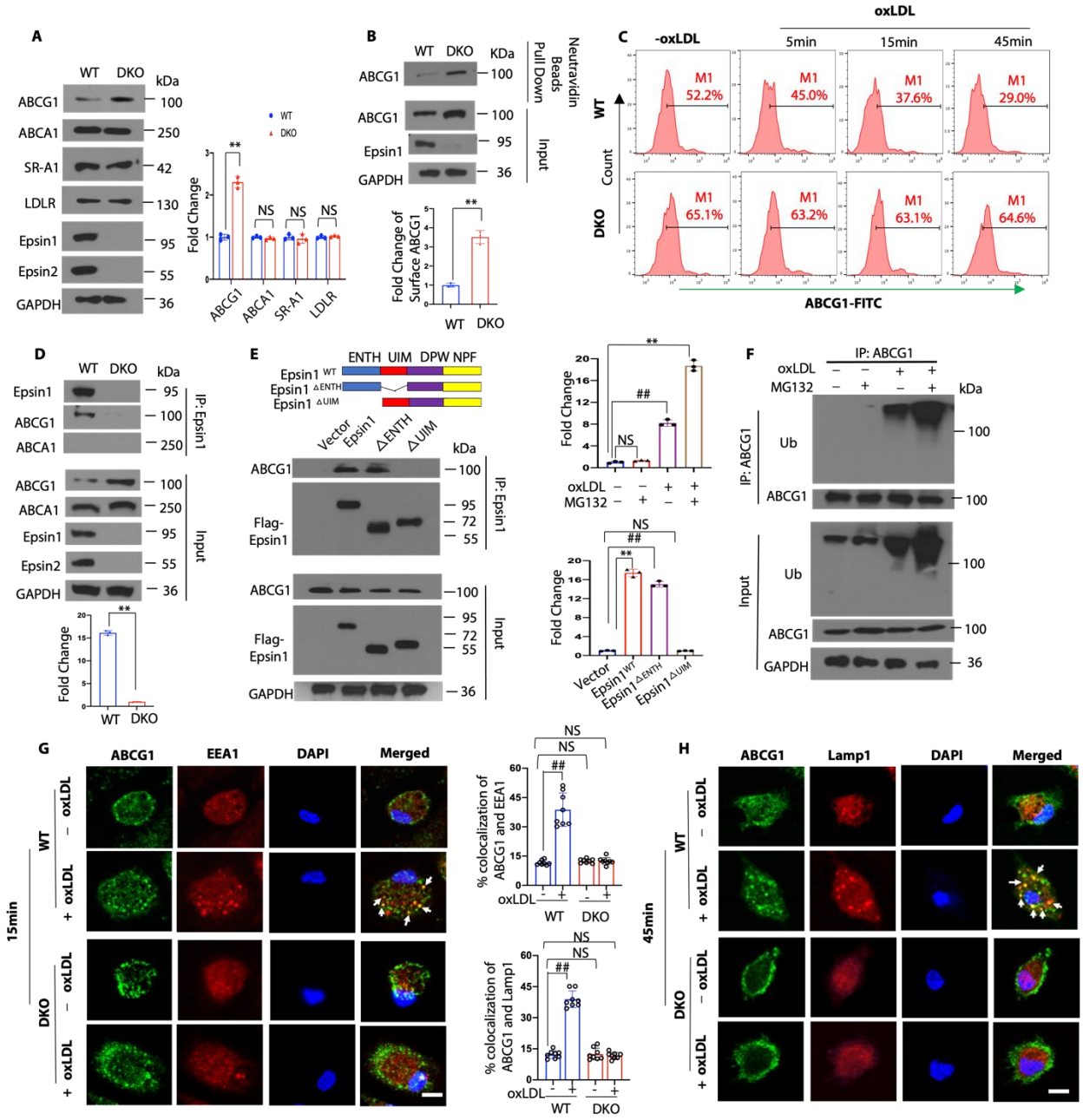

Fig. 6. Epsins bind to ABCG1 and facilitate the internalization and degradation of ABCG1 via lysosomes. (**A**) Macrophages from WT (n=3) and DKO (n=3) mice were lysed for WB analysis (**WT vs DKO, P<0.01). (**B**) Macrophages from WT (n=3) and DKO (n=3) mice were pretreated with a liver X receptor (LXR) activator and followed by a cell surface biotinylation assay to

evaluate the cell surface ABCG1 levels (**WT vs DKO, P<0.01). (**C**) LXR activated WT and DKO macrophages were incubated in lipid-deficient medium for 24h and treated with or without 100μg/mL oxLDL for 5, 15 and 45 min followed by staining with anti-ABCG1 and analyzed by flow cytometry. (**D**) LXR pretreated macrophages isolated from WT and DKO mice were treated with 100μg/mL oxLDL for 1h followed by IP and WB for Epsin1 and ABCG1 or ABCA1 (n=3, **WT vs DKO, P<0.01). (**E**) ABCG1 plasmids and full length (FLAG-Epsin1^{WT}) or domain-deletion constructs (FLAG-Epsin1$^{\triangle ENTH}$ or FLAG-Epsin1$^{\triangle UIM}$) in the pcDNA3 vector were transfected into HEK 293T cells for 24 h in the presence of LXR agonist. Cells were then treated with 100μg/mL oxLDL for 1h, followed by IP and WB analysis using antibodies against FLAG tags and ABCG1 (n=3, **Epsin1 ^{WT} vs vector group, P<0.01; $^{\#\#}$ Epsin1$^{\triangle ENTH}$ vs vector group, P<0.01). (**F**) Peritoneal macrophages isolated from WT mice were cultured in serum-free media for 24h followed by treatment with 5 μM MG132 for 3h. Cells were then treated with 100μg/mL oxLDL for 1h followed by IP and WB for ubiquitin and ABCG1. (**G-H**) WT and DKO macrophages were incubated in lipid-deficient medium for 24h followed by incubation with or without 100μg/mL oxLDL for 15min **(**G**)** or 45min **(**H**)** at 37^{0}C. Macrophages were stained with ABCG1 (green), early endosome marker EEA1 (red) or lysosome marker Lamp1 (red) and DAPI (blue), then assessed by confocal microscopy. White arrows indicate the endocytic vesicles, scale bar=5μm, $^{\#\#}$-oxLDL vs +oxLDL group (n=8), P<0.01. Data from A-H are presented as mean ± SD and were analyzed using either an unpaired Student's t-test (two groups) or one-way ANOVA (multiple comparisons).

Figure 7

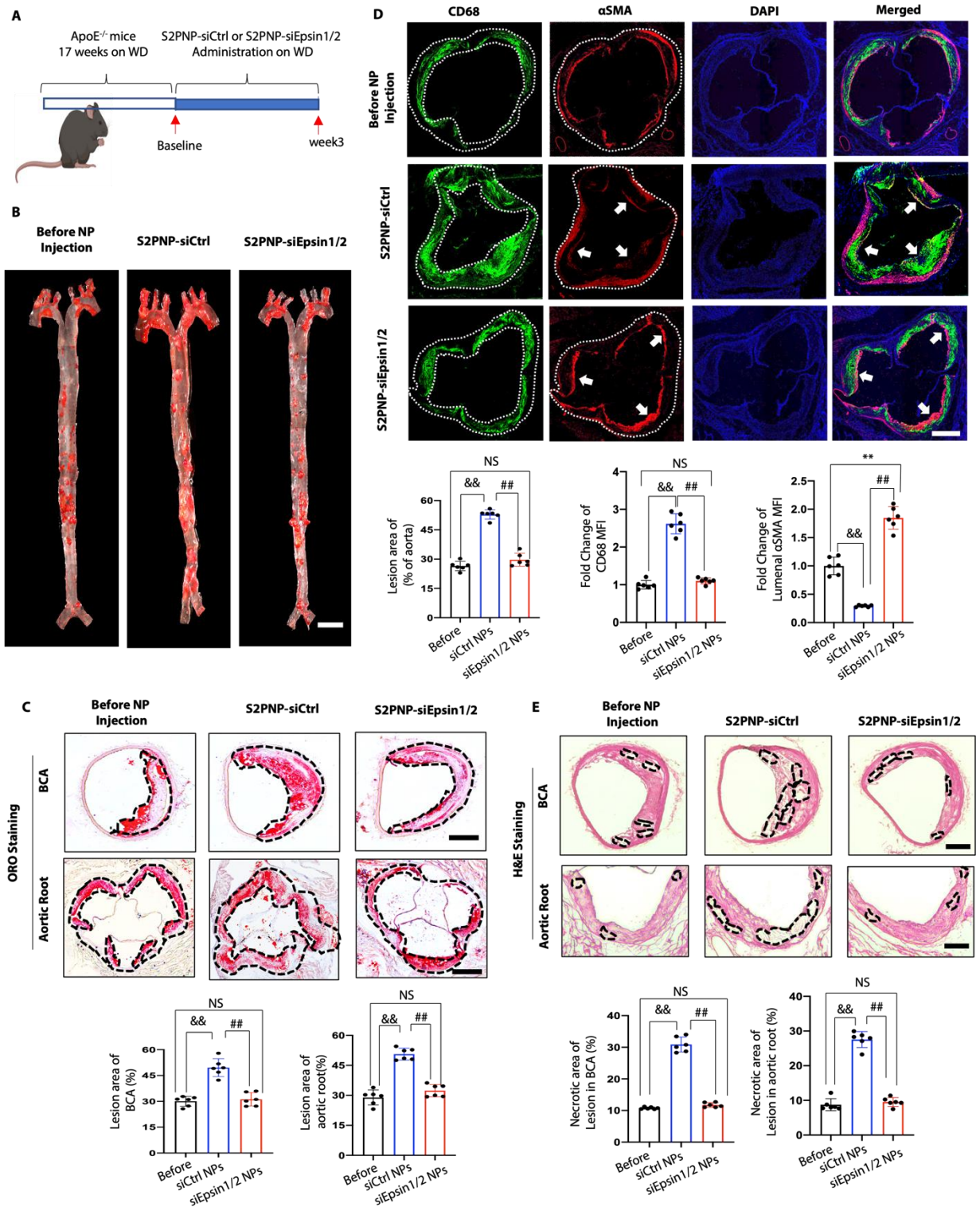

869

870

Fig. 7. S2PNP-siEpsin1/2 delivery inhibits atheroma progression, decreases necrotic core content, and increases smooth muscle cell content in advanced stage of atherosclerosis. (**A**) ApoE$^{-/-}$ mice fed a Western Diet (WD) for 17 weeks followed by treatment of S2PNP-siCtrl or S2PNP-siEpsin1/2 for 3 weeks (2 doses per week). (**B**) *En face* ORO staining of aortas from baseline, control siRNA NP-treated ApoE$^{-/-}$ or Epsin1/2 siRNA NP treated ApoE$^{-/-}$ mice fed a WD. lesion areas were analyzed with NIH ImageJ, scale bar=5mm. (**C**) ORO staining of brachiocephalic artery (BCA) and aortic root sections of above three groups. Lesional area (black dash line outlined) were analyzed by NIH ImageJ. (**D**) Aortic roots from S2PNP-siCtrl-treated ApoE$^{-/-}$ or S2PNP-siEpsin1/2 treated ApoE$^{-/-}$ mice were stained with the macrophage marker CD68 (dashed white line outlined) and αSMA (white arrow). (**E**) H&E staining of BCA and aortic root sections of the above three groups. Necrotic areas (black dash line outlined) were analyzed by NIH ImageJ. Data from B-E (n=6) are presented as mean ± SD and were analyzed using one-way ANOVA. $^{\&\&}$S2PNP-siCtrl vs baseline, $P<0.01$; $^{\#\#}$S2PNP-siCtrl vs S2PNP-siEpsin1/2 group, $P<0.01$, scale bar: B=5mm; C, D, E=500μm.

Figure 8

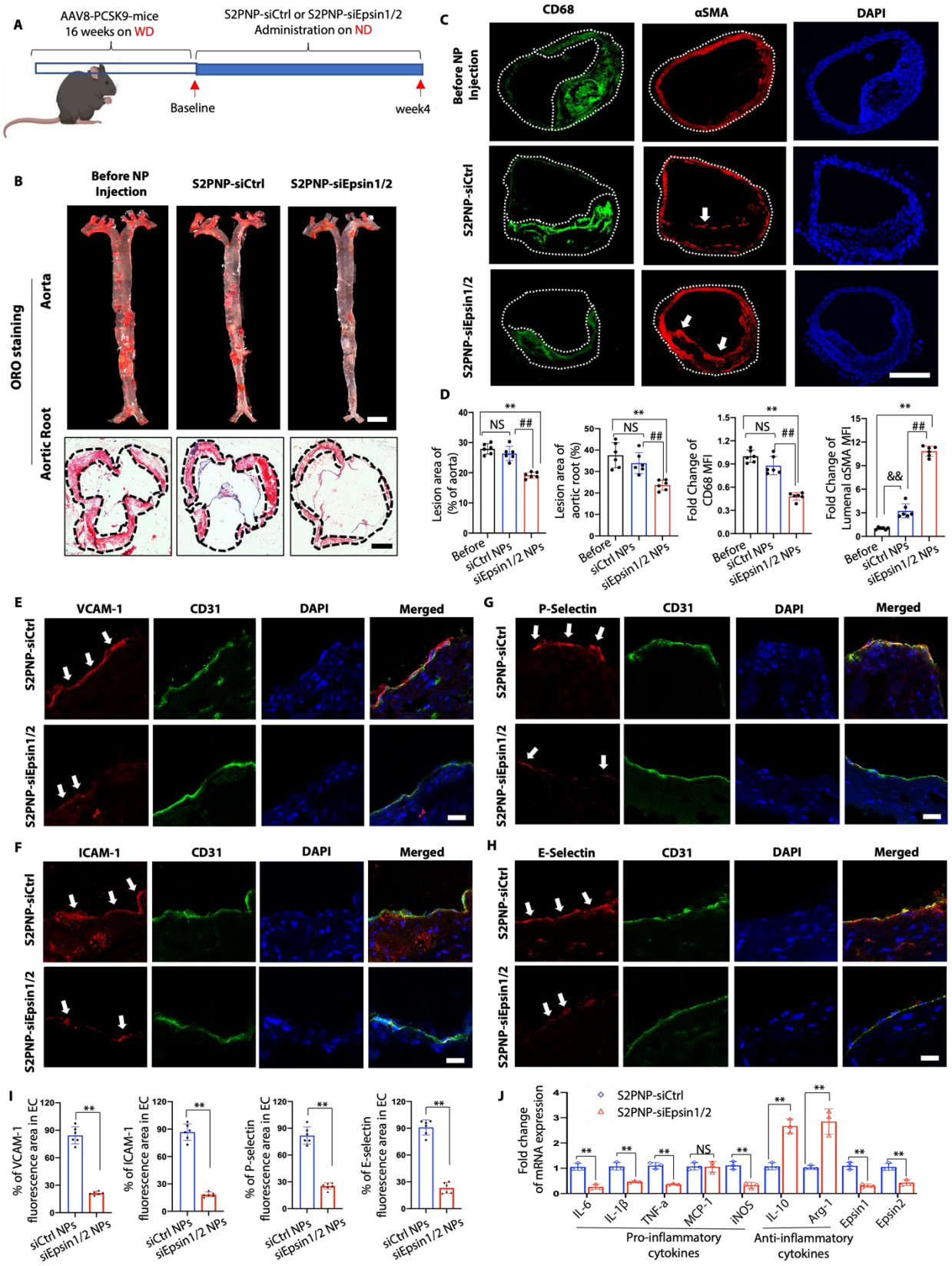
A
AAV8-PCSK9-mice
16 weeks on WD
S2PNP-siCtrl or S2PNP-siEpsin1/2
Administration on ND
Baseline
week4
B
Before NP Injection
S2PNP-siCtrl
S2PNP-siEpsin1/2
ORO staining
Aorta
Aortic Root
C
CD68
αSMA
DAPI
Before NP Injection
S2PNP-siCtrl
S2PNP-siEpsin1/2
D
Lesion area of (% of aorta)
Lesion area of aortic root (%)
Fold Change of CD68 MFI
Fold Change of Lumenal αSMA MFI
NS
##
&&
**
Before
siCtrl NPs
siEpsin1/2 NPs
E
VCAM-1
CD31
DAPI
Merged
F
ICAM-1
G
P-Selectin
H
E-Selectin
I
% of VCAM-1 fluorescence area in EC
% of ICAM-1 fluorescence area in EC
% of P-selectin fluorescence area in EC
% of E-selectin fluorescence area in EC
J
S2PNP-siCtrl
S2PNP-siEpsin1/2
Fold change of mRNA expression
IL-6
IL-1β
TNF-a
MCP-1
iNOS
IL-10
Arg-1
Epsin1
Epsin2
Pro-inflammatory cytokines
Anti-inflammatory cytokines

886

Fig. 8. S2PNP-siEpsin1/2 promotes the resolution of atheroma, reduces inflammation, and stabilizes atherosclerotic plaques. (**A**) C57BL/6 WT mice were injected twice with PCSK9-AAV8 (D377Y) virus and fed a WD for 16 weeks and followed by normal diet feeding with the treatment of S2PNP-siCtrl or S2PNP-siEpsin1/2 for 4 weeks (2 doses per week). (**B**) *En face* ORO staining of aortas from above mice. Lesion area was analyzed using NIH ImageJ, scale bar=5mm. (**C**) Immunostaining of CD68 (green) and αSMA (red) in the above groups. White arrows indicate the luminal αSMA. For (B) and (C), n=6, scale bar: B (aorta)=5mm, B (aortic root)=500μm, C=500μm. (**D**) Statistics for ORO staining (B) and IF staining (C), **S2PNP-siEpsin1/2 vs baseline, P<0.01, ##S2PNP-siCtrl vs S2PNP-siEpsin1/2 group, P<0.01. (**E-H**) Co-staining of CD31 (endothelial cell marker, green) with vascular cell adhesion molecule-1 (VCAM-1, red, E), intercellular adhesion molecule-1 (ICAM-1, red, F), P-selectin (red, G) or E-selectin (red, H) and DAPI on the luminal surface of aortic root sections. White arrows indicate CD31/ICAM-1, CD31/VCAM-1, CD31/E-selectin or CD31/P-selectin colocalization. Scale bars=20μm. (**I**) Statistical analysis of E-H, n=6, **S2PNP-siCtrl vs S2PNP-siEpsin1/2 group, P<0.01. (**J**) Isolated macrophages from PCSK9-mice were treated with S2PNP-siCtrl or S2PNP-siEpsin1/2 for 24h, RNA was isolated, and qRT-PCR was performed (n=3, **S2PNP-siCtrl vs S2PNP-siEpsin1/2 group, P<0.01). B-J are presented as mean ± SD and were analyzed using one-way ANOVA (B and C) and the unpaired Student's t-test (E-J).

Online Supplementary Materials

Targeting Epsins by nanotherapy regulates lipid metabolism and promotes ABCG1-mediated cholesterol efflux to fortify atheroma regression

Kui Cui[1]†, Xinlei Gao[2]†, Beibei Wang[1]†, Hao Wu[1], Yunzhou Dong[1], Yuling Xiao[3], Xingya Jiang[3], Marina V. Malovichko[4], Kathryn Li[1], Siu-Lung Chan[1], Dan Shan[1], Qianman Peng[1], Yaowei Lu[1], Bo Zhu[1], Scott Wong[1], Douglas B. Cowan[1], MacRae Linton[5], Sanjay Srivastava[4], Jinjun Shi[3], Kaifu Chen[2*], Hong Chen[1*]

†These authors contributed equally to this work.

*Corresponding authors. Email: hong.chen@childrens.harvard.edu

kaifu.chen@childrens.harvard.edu

The supplementary materials include:

Materials and Methods

Fig. S1. Differentially expressed genes between WT and DKO macrophages.

Fig. S2. Representative shared differentially expressed genes in DKO and CD36 knock out macrophage.

Fig. S3. Foam cell genes are downregulated in Epsin-deficient macrophages.

Fig. S4. Gating strategy used in the flow cytometric evaluation for Fig. 2C and 2H.

Fig. S5. The loss of Epsins reduced oxLDL uptake by macrophages.

Fig. S6. Transfection of full-length Epsin1 and constructs with the ENTH and UIM domains deleted into WT macrophages did not affect lipid uptake.

Fig. S7. Differentially expressed genes between WT and ABCG1 knockout (ABCG1KO) macrophages.

Fig. S8. Schematic of the quantification for radiolabeled cholesterol.

Fig. S9. Gene expression levels of indicated gene in WT and DKO macrophage.

Fig. S10. Gating strategy used in the flow cytometric evaluation for Fig. 6C.

Fig. S11. The expression of ABCG1 decreased with atherosclerotic progress in humans and mice.

Fig. S12. Characterization and silencing efficacy of S2P-conjugated siEpsin1/2 NPs.

Fig. S13. S2PNP-siEpsin1/2 treated macrophages show reduced foam cell formation.

Fig. S14. S2PNP-siEpsin1/2 inhibits lesion formation and macrophage accumulation in early stage of atherosclerosis.

Fig. S15. Silencing lesional macrophage Epsin1/2 by S2PNP-siEpsin1/2 NP-treatment stabilized plaques in a progression model of atherosclerosis.

Fig. S16. Delivery of S2PNP-siEpsin1/2 does not change cholesterol and triglyceride levels of $ApoE^{-/-}$ mice fed a WD.

Fig. S17. Silencing macrophage Epsin1/2 by S2PNP-siEpsin1/2 NPs reduces lesion size in a regression model of atherosclerosis.

Fig. S18. Summary schematic diagram of the study.

Table S1. List of reagents and animal models.

Data file S1. Differentially expressed genes in DKO compared to wild type.

Data file S2. Gene Ontology enrichment analysis for DEGs in DKO compared to wild type.

Data file S3. Gene expression data for heatmap showing overlapping between DKO and CD36KO.

Data file S4. Gene Ontology enrichment analysis for DEGs shared by DKO and CD36KO.

Data file S5. Gene differential expression analysis between foam and macrophage cells.

Data file S6. Gene differential expression analysis between ABCG1KO and wild type macrophages.

Data file S7. Gene Ontology enrichment analysis for DEGs in ABCG1KO compared to wild type.

Data file S8. Gene Ontology enrichment analysis for pathways reversely regulated by ABCG1KO and DKO.

Data file S9. Uncropped Western Blot.

Data file S10. Primary data of statistical analysis.

Materials and Methods

Methods, reagents, and antibodies

Parts of the methods and materials are available in the Supplementary Materials. Antibodies, primers, and reagents are listed in Supplementary Table S1.

Animal models

In this study, all animal procedures were performed in compliance with institutional guidelines and mouse protocols were approved by the Institutional Animal Care and Use Committee (IACUC) of Boston Children's Hospital, MA, USA. Both male and female mice were used. C57BL/6 mice (stock #00664), ApoE$^{-/-}$ mice (stock #008525), LysM-Cre deleter mice (stock #004781), and ABCG1^{flox} mice (C57BL/6-Abcg1^{tm1Ched}/J, stock #027954) were purchased from Jackson Research Laboratory. As double knockout of Epsins 1 and 2 in mice lead to embryonic lethality, we generated Epsin1$^{fl/fl}$;Epsin2$^{-/-}$ mice. These mice were subsequently combined with LysM-Cre deleter mouse strains to create myeloid-specific Epsins deficient (LysM-DKO) mice and bred them to the C57BL/6 background (Brophy et al., 2019). As proper controls, we also generated wild type C57BL/6 mice bearing LysM Cre. These mice only have one copy of LysM Cre as homozygous LysM Cre mice are susceptible to atherosclerosis. Furthermore, these mice were crossed to the ApoE$^{-/-}$ (C57BL/6) background to obtain ApoE$^{-/-}$/WT and ApoE$^{-/-}$/LysM-DKO mice (Brophy et al., 2019). We used macrophages from WT and LysM-DKO on either normal background or ApoE$^{-/-}$ background. We have not seen significant differences in the results with these backgrounds. ***For simplicity, we referred to the macrophages from WT or ApoE$^{-/-}$/WT as WT macrophages and macrophage from LysM-DKO and AopE$^{-/-}$/LysM-DKO as DKO macrophages.*** We used these mice (male and female) and primary macrophages (peritoneal and bone marrow derived) isolated from them for this study.

995 In addition, to generate myeloid-specific ABCG1-KO mice, we crossed the LysM-cre^{+} mice
996 with ABCG1$^{fl/fl}$ mice. We then bred the obtained LysM-cre^{+}; ABCG1$^{fl/fl}$ mice with ApoE$^{-/-}$ mice
997 and backcrossed them on to the C57BL/6 background.

998 To induce atherosclerosis, mice were fed Western diet (WD, Protein 17% kcal, Fat 40% kcal,
999 Carbohydrate 43% kcal; D12079B, Research Diets, New Brunswick, USA) starting at the age of
1000 6-8 weeks for 8-20 weeks. Mice were sacrificed at different time points based on the experimental
1001 design and peritoneal macrophages, blood, heart, aorta and bone marrow monocytes were
1002 harvested. For control mice, in addition to ApoE$^{-/-}$;Epsin1$^{+/+}$;Epsin2$^{+/+}$ mice, we also used ApoE^{-}
1003 $^{/-}$;Epsin1$^{+/+}$;Epsin2$^{+/+}$ mice with a single copy of LysM-cre, and ApoE$^{-/-}$;Epsin1$^{fl/fl}$;Epsin2$^{-/-}$
1004 littermates lacking the single copy of LysM-cre. To simplify the terminology, we refer to these
1005 control mice as ApoE$^{-/-}$, as results were not different in any of the analyses we performed. For the
1006 study of atheroma resolution, WT mice (both male and female) at the age of 8 weeks were
1007 intravenously injected with $2x10^{11}$ genomes of PCSK9 adeno-associated virus (rAAV8-D377Y-
1008 mPCSK9 purchased from Boston Children's Hospital Viral Core Facility) followed by 17 weeks
1009 of WD feeding. For each experimental model and time point, 6-10 mice were analyzed and both
1010 male and female mice were used in separate groups.

1011 **Human samples**

1012 Human healthy control (n=3) and diseased aortic arch samples (n=3) from atherosclerosis
1013 patients were purchased from Maine Medical Center Biobank. The medical information of the
1014 atherosclerotic patient samples is in Data file S10. The paraffin sections were de-paraffinized and
1015 performed antigen retrieval to unmask the antigenic epitope with 10mM Sodium Citrate, pH 6.0,
1016 with 0.5% Tween 20 at 90°C for 10 minutes. Immunofluorescence staining of the slides was
1017 performed with the standard protocol described below.

1018 **Isolation of primary mouse macrophage and macrophage culture**

1019 The isolation of peritoneal macrophages was performed as described previously (Cui et al.,
1020 2019). Briefly, mice were intraperitoneally injected with 1mL of 4% thioglycolate (TG), and 3
1021 days post-injection, mice were sacrificed, and peritoneal cells were harvested with 7mL of sterile
1022 PBS by lavage of peritoneal cavity. Cells were spun down (1000xg, 5 minutes), washed with PBS,
1023 resuspended, and plated in RPMI (containing 10% FBS and 1% PennStrep) at 37 °C in humidified
1024 air containing 5% CO_2 atmosphere. After 3 hours, non-macrophages were washed with PBS. For
1025 bone marrow-derived macrophages, mice were sacrificed, and both femurs and tibias were
1026 dissected and flushed with sterile 1X PBS, followed by passing through a 70μM cell strainer. Cells
1027 were spun down (1000xg, 5 minutes), washed with PBS, and seeded in RPMI (containing 10%
1028 FBS and 1% PennStrep) with macrophage colony stimulating factor (M-CSF, 10ng/mL) to
1029 differentiate into macrophages for 5 days. After which, the macrophages were harvested and used
1030 in experiments. Both bone marrow-derived and isolated peritoneal primary macrophages were
1031 used to confirm knock out of Epsin1 and Epsin2. Isolated peritoneal macrophages were mainly
1032 used for western blots, flow cytometry and immunoprecipitations due to higher yields.

1033 **RNA isolation, quantitative real-time PCR and RNA sequencing**

1034 Total RNA was extracted from primary macrophages with Qiagen RNeasy Mini Kit based on
1035 manufacturer's instruction including the optional step to eliminate genomic DNA. The extracted
1036 RNA was either used for qRT-PCR or RNA sequencing according to the experimental designs.

1037 For qRT-PCR, mRNA was reverse transcribed to cDNA with the iScript cDNA Synthesis Kit
1038 (Bio-Rad Laboratories, Inc., Hercules, CA, United States). 2 μl of the product was subjected to
1039 qRT-PCR in StepOnePlus Real-Time PCR System (Applied Biosystems) using SYBR Green PCR

Master Mix reagent as the detector. PCR amplification was performed in triplicate on 96-well optical reaction plates and replicated in at least three independent experiments. The ΔΔCt method was used to analyze qPCR data. The Ct of β-actin cDNA was used to normalize all samples. Primers are listed in Supplementary Table S1. For RNA sequencing, extracted RNA from primary macrophages with Qiagen RNeasy Mini Kit based on manufacturer's instruction were sent to BGI Genomics Company (San Jose, USA) for RNA sequencing.

RNA sequencing data processing and differential expression analysis

The raw reads of RNA sequencing data were mapped to the mouse genome (version mm10) using STAR (version 2.7.9a) (Dobin et al., 2013) or TopHat (version v2.1.1) (Kim et al., 2013). The read count was calculated for each gene by htseq-count (version 0.11.2) (Anders et al., 2015) and further normalized to TPM (transcripts per million) and FPKM (fragments per kilobase of transcript per million fragments mapped). For differential expression analysis of Epsin deficient and wild type macrophage dataset, the read count matrix produced by htseq-count was imported into the R package DESeq2 (version 1.30.1) (Love et al., 2014). For the ABCG1 knock out dataset, we first performed a batch effect removal on the log10 transformed TPM expression matrix using ComBat in the R package sva (version 3.38.0) (Johnson et al., 2007). Then, the R package limma was used to do differential expression analysis for the batch effect removed expression matrix. Genes with fold change larger than 1.2-fold and p-value less than 0.05 were identified as differentially expressed genes (DEGs). Principal component analysis (PCA) was conducted by the plotPCA function of DESeq2. Heatmap of gene expression values was generated using the R package pheatmap (version 1.0.12). Gene Ontology (GO) functional enrichment analysis was performed by the R package clusterProfiler (version 3.18.1) (Yu et al., 2012).

For the comparison of DEGs between DKO and CD36 knockout macrophages in mice, we

utilized the published bulk RNA-seq data from Chen et. al. (Chen et al., 2019), with the accession number GSE139439, downloaded from NCBI GEO database (Edgar et al., 2002). The overlapping DEGs co-regulated in DKO and CD36 knockout macrophages were analyzed by the R package VennDiagram (version 1.6.20) (Chen and Boutros, 2011). The statistical significance of overlapping genes was calculated by Fisher exact test.

Foam cell and macrophage bulk RNA-Seq data is from the publicly available dataset GSE116271 reported by Kim et. al. (Kim et al., 2018). Foam and non-foam cell RNA-Seq data was mapped onto mouse mm10 genome using Tophat2 (version v2.1.1) (Kim et al., 2013). Read counts were assigned to genes by htseq-count. Gene expression levels were calculated by the R package edgeR (version 3.32.1) (Robinson et al., 2010). Gene set enrichment analysis (GSEA) (Mootha et al., 2003; Subramanian et al., 2005) was used to investigate if the DEGs in DKO show statistically significant differences between foam cells and macrophages. All the data are available in Data files (S1-S8).

Cell culture and plasmids transfection

The HEK 293T cell line (ATCC no. CRL-11268) were used for plasmid transfection to map the binding sites of Epsin to CD36 or ABCG1. Flag-tagged Epsin1^{WT}, Epsin1$^{\Delta UIM}$, Epsin1$^{\Delta ENTH}$ truncation constructs, and pcDNA vector were prepared previously in our lab(Dong et al., 2020). CD36 (lot:52025) and ABCG1 (lot:53952) plasmids were purchased from Addgene. HEK 293T cells were cultured in DMEM (10% FBS and 1% PennStrep) at 37°C in humidified air containing 5% CO_2 atmosphere and transfected using Lipofectamine 2000 as instructed by the manufacturer. Transfection of Epsin domains to macrophage: Isolated WT and DKO peritoneal macrophages were cultured in RPMI media (containing 10% lipid-depleted serum and 1% PennStrep). Epsin1^{WT}, Epsin1$^{\Delta UIM}$, Epsin1$^{\Delta ENTH}$ truncation constructs, and pcDNA vector were transfected to

macrophages using lipofectamine LTX transfection reagent or using Nucleofector II apparatus (Amaxa, Germany) with mouse macrophage nucleofector kit (Lot: VPA-1009, Lonza) as instructed by the manufacturer.

Immunoprecipitation (IP) and western blotting (WB)

For total protein levels, primary macrophages were washed with ice cold PBS, lysed in RIPA buffer (50 mM Tris HCl, 150 mM NaCl, 1.0% NP-40, 0.5% Sodium Deoxycholate, 1.0 mM EDTA, 0.1% SDS and 0.01% sodium azide at a pH of 7.4.), added 4X Laemmli buffer (1:3 dilution in lysis buffer) was added and WB was perfomed for the proteins indicated in this study. For IP, cells were washed with ice cold PBS, lysed with lysis buffer (1% Triton X-100, 5mM Na_3VO_4, 10mM N-ethylmaleimide, and protease inhibitor cocktail), spun down (12000xg, 5 min at 4°C) to remove the debris. Cell lysates were pre-cleared with appropriate species of IgG and protein A/G Sepharose beads for 1h at 4°C with rotation followed by incubation with A/G Sepharose beads and indicated antibodies for 12 hours at 4°C with rotation. For negative controls, equal concentrations of mouse IgG were added instead of specific antibodies. Precipitated proteins were washed with ice cold lysis buffer for 3 time and eluted from protein A/G beads using 2X Laemmli buffer (1:1 in lysis buffer) followed by WB as described previously (Brophy et al., 2019). WB were repeated for at least 3 times with different mice and bands were quantified using NIH ImageJ software. The protein expression levels were normalized to GAPDH levels. For IPs in macrophages involving oxLDL treatment, cells were pre-treated with 1 μM MG132 in serum-free media for 4 hours, followed by the treatment with or without oxLDL (100μg/ml) for 30 minutes at 37°C and processed for immunoprecipitation. For the transfection of Epsin1 constructs and CD36 or ABCG1 constructs, transfected HEK 293T cells were cultured in lipid-depleted DMEM media for 24 hours followed by stimulation with 100μg/mL oxLDL for 30 minutes at 37°C and performed for

immunoprecipitation.

Atherosclerosis analysis

Mice were anesthetized with isoflurane. Blood was collected from the right atrium followed by left ventricle perfusion with cold PBS. Whole aortas, brachiocephalic artery (BCA) and hearts of the mice were isolated. Whole aortas were dissected symmetrically, pinned to parafilm and fixed in 4% PFA to allow the *en face* analysis. Heart and BCA were embedded in OCT mounting medium and immediately frozen. The aortic sinus and BCA in the heart were sectioned at 10 microns (at least 9 sections of each sample were collected). The internal elastic lamina and luminal boundary of the lesion was manually traced and the lesion sizes of the *en face* aortas and aortic roots were quantified by NIH ImageJ software. The methods for Oil red O (ORO) staining, immunofluorescent (IF) staining, Hematoxylin and Eosin (H&E) staining, and Van Gieson's staining are described in supplementary materials (Brophy et al., 2019).

Oil Red O (ORO) staining and immunofluorescent (IF) staining of primary macrophages or cryosections were performed as described below. Oil Red O imaging was taken by a Zeiss Axio Scope.A1, AxioCam ICc5, and analyzed by ZEN-Lite 2012 software. Imaging of *en face* aortas was performed using a Nikon SMZ1500 stereomicroscope, SPOT Insight 2Mp Firewire digital camera, and SPOT Software 5.1. Imaging of IF staining was taken by Zeiss confocal microscope and quantification areas were performed by manually tracing the aortas, BCA, and aortic root lesion areas with NIH ImageJ software. Statistical analysis of samples including Oil Red O, Van Gieson, H and E, and IF staining were performed by blinding in which each animal was assigned a number and data was collected based on the assigned number with genotype and experimental condition unknown to the data collector.

Oil Red O staining. For cryostat sections: cryostat sections 10 microns were fixed in 4% paraformaldehyde. Slides were washed with PBS (3 times, 5min each time), and rinsed with 100% propylene glycol followed by staining with freshly prepared 0.5% Oil Red O solution for 10 minutes at 60°C. Slides were then put in 85% propylene glycol for 2 minutes, followed by 3 washes in water. Slides were next incubated with hematoxylin for 1-2 min, rinsed 3 times in water, and mounted with aqueous mounting media. For foam cells: coverslips were washed with PBS, fixed in 4% paraformaldehyde for 10 minutes and stained with freshly prepared 0.5% Oil Red O solution for 10 minutes at 65°C. Slides were then washed in PBS (3 times, 5min each time), incubated with hematoxylin for 1min, washed with PBS 3 times, and mounted on coverslips with aqueous mounting media. Imaging was processed with a Zeiss LSM880 confocal microscope and analyzed with ZEN-Lite 2012 software and HIH ImageJ software. Quantification of lesion was performed as described above. Quantification of foam cells was performed as described below.

Hematoxylin and Eosin (H&E) staining. Frozen aortic root and BCA sections: slides were fixed in 10% buffered formalin for 15 minutes and washed in water. Next, slides were stained with 0.1% hematoxylin for 3min followed by ddH_2O washes, 95% ethyl alcohol and water. Slides were then dipped in 0.5% Eosin for 3 min, quickly rinsed with ddH_2O, dipped in 95% and 100% ethanol, incubated in 50:50 Xylenes:100% ethanol and incubated in 100% Xylenes. Slides were mounted using Permount with coverslips.

Van Gieson's staining. Sections were fixed in 10% buffered formalin for 15 minutes and washed in water. Slides were stained with hematoxylin for 10 min, washed in ddH_2O, stained 1-3 min in Van Gieson's solution, dehydrated in 95% alcohol and 100% alcohol two times. Then, slides were cleared in xylene for two times and mounted with Permount. Staining results were presented as: Elastic fibers and nuclei–Black, Collagen fibers–Red and Other tissue elements–

Yellow. Lesion area was traced using NIH ImageJ software. The percentage of necrotic area was determined by necrotic areas within the lesion. Collagen content was determined by the percentage of lesion areas.

Immunofluorescent staining. Human samples: human healthy and atherosclerotic aorta paraffin sections were deparaffinized in xylene for 15min, immersed in graded ethanol (100%, 100%, 95%, 90%, 80%, and 70%, each for 3 min), washed with running tap water and processed antigen retrieval with 10mM Sodium Citrate, pH 6.0, with 0.05% Tween 20 at 90°C for 10 minutes. Samples were blocked in PBS with 3% donkey serum, 3% BSA, and 0.3% Triton X-100 and incubated with primary antibodies ABCG1 or CD68 (1:70 dilution) at 4°C overnight. The sections were washed three times and respective secondary antibodies conjugated to fluorescent labels (Alexa Flour 594, 488, or 647; 1:200 to 1:500) were added for 2 h at room temperature. The sections were mounted with mounting media containing DAPI (1:100).

Mouse aortic root and BCA cryosections: Sections were fixed by 4% paraformaldehyde for 30 min at room temperature and blocked in PBS solution containing 3% donkey and/or goat serum, 3% BSA, and 0.3% Triton X-100 for 1hour. Samples were then incubated with primary antibody at 4°C overnight, followed by incubation with the respective secondary antibodies conjugated to fluorescent labels (Alexa Flour 594, 488, or 647; 1:200 to 1:500) for 2 hours at room temperature. The sections were mounted with mounting media containing DAPI (1:100).

Staining of peritoneal macrophages: macrophages plated on the 18-mm coverslips were washed with PBS, fixed by 4% paraformaldehyde for 15 min at room temperature and blocked in PBS solution containing 3% donkey and/or goat serum, 3% BSA, and 0.3% Triton X-100 for 1hour. Coverslips were then incubated with primary antibody (CD36, ABCG1, EEA1, Rab11, or Lamp1; 1:100-1:300) at 4°C overnight, followed by incubation with the respective secondary antibodies

conjugated to fluorescent labels (Alexa Flour 594, 488, or 647; 1:200 to 1:500) for 1 hour at room temperature. The sections were mounted with mounting media containing DAPI (1:100). BODIPY™ 493/503 staining of macrophages was performed following F4/80-fluorescent conjugated antibody incubation for 2 hours at room temperature (Spangenburg et al., 2011). Slides were washed with PBS, stained with DAPI and mounted. Immunofluorescent images were captured using a Zeiss LSM880 confocal microscope and analyzed with ZEN-Lite 2012 software and HIH ImageJ software. Samples stained without the primary antibody were obtained using the same settings as negative controls. Mean fluorescence intensity (MFI) of antibody staining was determined via NIH ImageJ software with n=3 or more.

Flow cytometry assay

Flow cytometry of elicited primary macrophages: peritoneal macrophages from WT and DKO mice were isolated as described above and plated in 6 well plates in lipid-deficient medium for 24 hours followed by the treatment with or without 100µg/mL oxLDL for 1h at 37^0C. Macrophages were washed with 1XPBS, dissociated with 1mL non-enzymatic cell dissociation buffer, centrifuged (300xg, 5 minutes), and resuspended in 100µl FACS buffer (1X PBS, 2% FBS, 2mM EDTA) containing the following: FcR Blocking Reagent, fluorochrome conjugated anti-F4/80, primary antibodies against CD36 or ABCG1. Cells were incubated with the primary antibodies (1:100) on ice for 30min, washed with 100µl FACS buffer, spun down and resuspended with 100µl FACS buffer containing the fluorescent secondary antibodies (1:100). After 30 min, cells were washed with FACS buffer, fixed with 4% paraformaldehyde (PFA), and resuspended in FACS buffer for analysis. Single color and no color controls were prepared using elicited macrophages, which were treated the same as experimental groups. Expression of cell markers was analyzed using a FlowJo version 10 software. Gating strategies were performed as described in

1200 Supplementary Figures S4 and S10. Flow cytometry of DiI-oxLDL treated macrophages:
1201 peritoneal macrophages elicited from WT and DKO mice were incubated in lipid-deficient
1202 medium for 24 hours followed by the treatment of DiI-oxLDL for 2h at 37^0C and macrophages
1203 were washed with 1XPBS, dissociated with 1mL non-enzymatic cell dissociation buffer,
1204 centrifuged (300xg, 5 minutes), resuspended in 100µl FACS buffer (1X PBS, 2% FBS, 2mM
1205 EDTA) containing the following: FcR Blocking Reagent, fluorochrome conjugated anti-F4/80
1206 antibody staining, fixed and assessed the uptake of lipoproteins by flow cytometry as described
1207 above.

1208 **Foam cell formation**

1209 TG (4%) induced peritoneal macrophages were isolated and plated on 18mm glass coverslips.
1210 Cells were cultured in RPM media (containing 10% lipid-depleted serum and 1% PennStrep) for
1211 24 hours and then treated with 10-100 µg/mL oxLDL for 24 hours (Brophy et al., 2019). Cells
1212 were fixed in 4% PFA for 10 minutes at room temperature and washed with PBS. For Oil Red O
1213 staining, coverslips were stained with Oil Red O, washed with PBS, counterstained with
1214 hematoxylin, washed with PBS, and then mounted on slides. For Bodipy staining, coverslips were
1215 immunofluorescently stained BodipyTM 493/503 and phalloidin-iFluor 555 reagent for 1 hour at
1216 37°C, counterstaining with DAPI, and mounting on slides. Negative controls were not treated with
1217 oxLDL. Foam cells were determined as the number of lipid positive cells (Oil Red O positive or
1218 Bodipy positive) as a percentage of total cells. At least 6 fields per cover slip and 6 mice per
1219 genotype were used for quantification.

1220 **Cell surface biotinylation**

1221 Cell surface biotinylation was performed as described previously (Brophy et al., 2019). Isolated

1222 peritoneal macrophages in the plate were washed with cold PBS, suspended at a concentration of
1223 $25x10^6$ cells/mL and treated with 2mM EZ-Link Sulfo-NHS-LC-Biotin reagent on ice for 30
1224 minutes followed by 3 washes with 100mM Glycine to remove excess biotin and then 3 washes
1225 with cold PBS (5min each time). Cells were lysed and pulled down by streptavidin bead: cell
1226 lysates were incubated with neutravidin beads for at least 12 hours at 4°C with rotation, and
1227 proteins were eluted from beads using 4X Laemmli buffer diluted 1:3 in lysis buffer. Cell surface
1228 biotinylated proteins were analyzed by western blotting and quantified using NIH Image J
1229 software.

1230 **Plasma collection, triglyceride, and cholesterol analysis**

1231 For each mouse, 1mL syringe were rinsed with 1mL 0.5M EDTA to coat the inside of the
1232 syringe with EDTA to prevent clotting during blood collection. Blood was collected from the right
1233 atrium of the mouse heart after sacrifice with isoflurane and added to each 1.7mL tube containing
1234 50µl 0.5M EDTA. Blood was centrifuged at 2000xg for 10 minutes at 4°C. Plasma was transferred
1235 to a new tube and stored at -20°C. Plasma cholesterol and triglyceride levels were determined as
1236 described below.

1237 Total cholesterol, high-density lipoprotein (HDL) cholesterol and triglycerides in mouse serum
1238 were determined on Ace Axcel® Clinical Chemistry System (Alfa Wassermann, West Caldwell,
1239 NJ). Non-HDL cholesterol is calculated as Total Cholesterol – HDL and gives a measure of the
1240 cholesterol carried by all of the atherogenic lipoproteins.

1241 Quantification of total cholesterol, HDL and triglycerides in macrophages. Lipids were
1242 extracted from macrophages with hexane:isopropanol (3:2, v:v) as described in Robinet et al
1243 (Robinet et al., 2010). Solvents were removed by drying with nitrogen gas. Extracts were
1244 resolubilized in 5% bovine serum solution by bath sonication (10 minutes at 37°C), freeze/thaw

1245 treatment (1 hour at -80°C) and followed by probe sonication for 10 seconds. Reconstituted
1246 samples were analyzed on Ace Axcel® Clinical Chemistry System for total cholesterol, HDL and
1247 triglycerides as described above for measurements in mouse serum. Obtained values were
1248 normalized to total protein measured in the cell lysates by Bradford Protein Assay (Bio-Rad).

1249 **Macrophage cholesterol efflux assay**

1250 Thioglycolate induced peritoneal macrophages from WT, DKO and DKO/ABCG1$^{fl/+}$ mice
1251 were plated in RPMI medium for 2-4 hours. Non-adherent cells were removed by washing with
1252 PBS and cells were incubated with radiolabeled medium supplemented with 4 μCi/mL of [^{3}H]-
1253 cholesterol (Perkin-Elmer, Waltham, MA, USA), 5% FBS,1% P/S and 50μg/mL acetyl-LDL for
1254 24 hours. Macrophages were washed twice with warm PBS and incubated with serum-free RPMI
1255 1640 medium supplemented with 0.2% BSA, 2μg/mL acyl-CoA cholesterol acyltransferase
1256 (ACAT) inhibitor and 4μmol/L LXR agonist T0901317 for 18 hours equilibration (Wang et al.,
1257 2006). After this equilibration period, cells were washed twice with warm PBS and incubated in
1258 serum free RPMI medium supplemented with cholesterol acceptors (10 μg/mL ApoA-1 or 25
1259 μg/mL HDL) and 2μg/mL ACAT inhibitor for 4 hours (Sankaranarayanan et al., 2011). At the end
1260 of the incubation, the efflux media was collected and filtered through a 0.45-μm filter to remove
1261 the detached cells. Then, transfer the efflux medium was transferred to a scintillation vial. The
1262 macrophages in the plates were added to 500 μl of 0.2N NaOH and incubated on shaker at 4 °C
1263 overnight. Cell extract from each well was transferred to a scintillation vial. 4 mL of scintillation
1264 liquid were added to each scintillation vial and radioactivity was measured by liquid-scintillation
1265 counting (Escola-Gil et al., 2015). The cholesterol efflux to acceptors was expressed as a
1266 percentage of total cholesterol using the following formula: % cholesterol efflux = (medium [^{3}H]-
1267 radioactivity [cpm]) / [(medium [^{3}H]-radioactivity [cpm] + [^{3}H]-radioactivity from cell extract

1268 [cpm])] x 100, where cpm = counts per minute.

1269 **Reverse cholesterol transport (RCT) assay**

1270 In vivo RCT experiment is based on the method detailed by Joan Carles Escolà-Gil et al
1271 (Escola-Gil et al., 2015). Briefly, macrophages were radiolabeled with [^{3}H]-cholesterol (5 µCi/mL)
1272 in 10% lipoprotein-depleted serum, 1% P/S and 50µg/mL acetyl-LDL RPMI media for 48h. Foam
1273 cells were washed with serum-free media supplemented with 0.2% BSA and equilibrated for 4h
1274 (37 °C, 5 % CO_2). Then, [^{3}H]-cholesterol-labeled macrophages were detached, spun down and
1275 resuspended in PBS. The injection dose was 0.5 mL per mouse (4x10^6 cpm/mL) administered
1276 intraperitoneally into C57BL/6 WT mice fed on normal diet as indicated in Figure 5C. Mice were
1277 then individually housed in metabolic cages and feces in the cage floor were collected for 2 days.
1278 At 48h, mice were sacrificed and blood, liver, intestinal contents were collected in Figure S8.
1279 Serum [^{3}H]-cholesterol was measured by liquid scintillation counting. [^{3}H]-HDL cholesterol was
1280 determined after precipitation of ApoB-containing lipoproteins with 0.44mM phosphotungstic
1281 acid and 20mM $MgCl_2$. Liver, fecal and intestinal lipids were extracted with hexane- isopropanol
1282 (3:2, v:v) and partitioned against Na_2SO_4. The lipid layer was collected and dried for 48h using
1283 nitrogen gas in a fume hood, and [^{3}H]-cholesterol radioactivity was measured by liquid
1284 scintillation counting (4mL scintillation fluid for 4 min). The [^{3}H]-radioactivity observed in fecal
1285 biliary acids was determined in the remaining aqueous phase of fecal material extracts. The amount
1286 of [^{3}H]-radioactivity was expressed as a percentage of the total injected dose, which was taken as
1287 100%.

1288 **Synthesis of DSPE-PEG-S2P, preparation and characterization of S2PNP-siRNA**

1289 To construct the lesional macrophage-targeted siRNA NPs, S2P peptide-conjugated DSPE-
1290 PEG (DSPE-PEG-S2P) was first synthesized via a thiol-maleimide Michael addition click reaction

between S2P peptide (CRTLTVRKC, GLS Biochem Systems Inc.) and DSPE-PEG-Mal [PEG molecular weight, 3.4 kDa; Nanocs Inc.], as reported previously (Tao et al., 2020). Then, a robust self-assembly method was used to prepare the targeted polymer-lipid hybrid NPs for siRNA delivery (Tao et al., 2020; Zhu et al., 2015). In brief, G0-C14 and PLGA were dissolved separately in anhydrous dimethylformamide (DMF) to form a homogeneous solution at the concentration of 2.5 mg/mL and 5 mg/ml, respectively. DSPE-PEG-OCH3 (DSPE-mPEG) and DSPE-PEG-S2P were dissolved in HyPure water (GE Healthcare Life Sciences, catalog no. SH30538) at the concentration of 0.1 mg/mL. 1 nmol Epsin1 siRNA and 1 nmol Epsin2 siRNA were gently mixed with 100 μl of the G0-C14 solution. The mixture of siRNA and G0-C14 was incubated at room temperature for 15 min to ensure the full electrostatic complexation. Next, 500 μl of PLGA polymers were added and mixed gently. The resultant solution was subsequently added dropwise into 10 mL of HyPure water containing 1 mg lipid-PEGs (i.e., 50% DSPE-PEG-S2P and 50% DSPE-mPEG hybrids for the S2P-targeted siRNA NPs, or 100% DSPE-mPEG for the non-targeted siRNA NPs) under magnetic stirring (1,000 rpm) for 30 min. The siRNA NPs were purified by an ultrafiltration device (EMD Millipore, MWCO 100 kDa) to remove the organic solvent and free excess compounds via centrifugation at 4 °C. After washing 3 times with HyPure water, the siRNA NPs were collected and finally resuspended in pH 7.4 PBS buffer. The NPs were used freshly or stored at -80 °C for further use. The physicochemical properties (particle size and surface charge) of S2PNP-siEpsin1/2 were characterized by dynamic light scattering (DLS, Brookhaven Instruments Corporation). The S2PNP-siEpsin1/2 was ~89 nm in size as measured by DLS, and their surface charge was determined to be ~ -5.3 mV.

Statistical analysis

Statistical analysis was processed using GraphPad Prism 8.4. Data are shown as mean ±

standard deviation (mean $\pm$ SD). Normality was determinedusing D'Agostino-Pearson normality testing for experiments with $n \geq 8$ and Kolmogorov-Smirnovnormality testing for experiments with $n < 8$. Data were analyzed by the unpaired Student's t-test or Mann-Whitney U test where appropriate for two groups. Data for multiple groups were analyzed with ANOVA with Bonferroni test or Dunn'smultiple comparison test where appropriate. P value less than 0.05 was considered significant.

Fig. S1

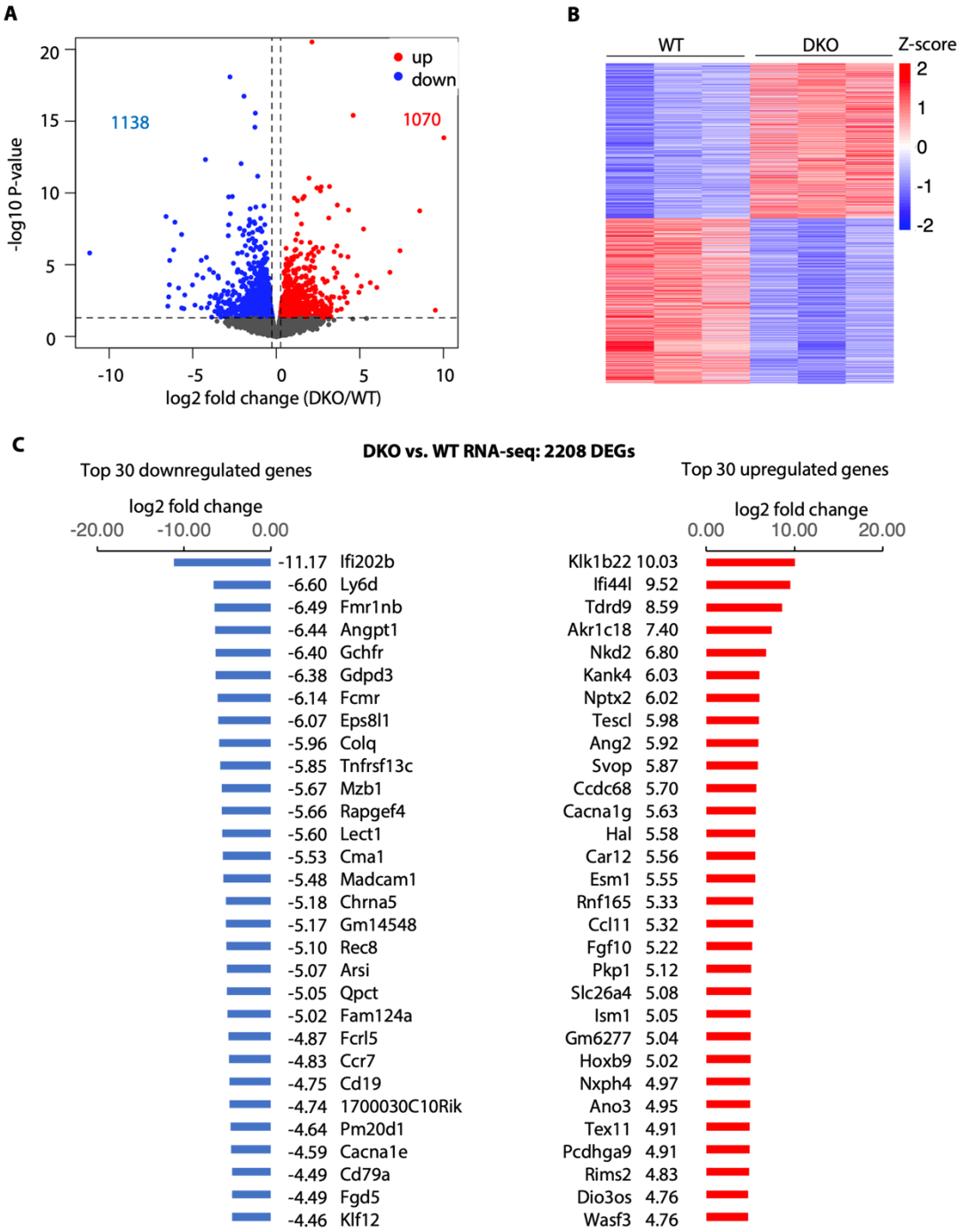
A
up
down
1138
1070
-log10 P-value
log2 fold change (DKO/WT)
B
WT
DKO
Z-score
C
DKO vs. WT RNA-seq: 2208 DEGs
Top 30 downregulated genes
log2 fold change
-11.17 Ifi202b
-6.60 Ly6d
-6.49 Fmr1nb
-6.44 Angpt1
-6.40 Gchfr
-6.38 Gdpd3
-6.14 Fcmr
-6.07 Eps8l1
-5.96 Colq
-5.85 Tnfrsf13c
-5.67 Mzb1
-5.66 Rapgef4
-5.60 Lect1
-5.53 Cma1
-5.48 Madcam1
-5.18 Chrna5
-5.17 Gm14548
-5.10 Rec8
-5.07 Arsi
-5.05 Qpct
-5.02 Fam124a
-4.87 Fcrl5
-4.83 Ccr7
-4.75 Cd19
-4.74 1700030C10Rik
-4.64 Pm20d1
-4.59 Cacna1e
-4.49 Cd79a
-4.49 Fgd5
-4.46 Klf12
Top 30 upregulated genes
log2 fold change
Klk1b22 10.03
Ifi44l 9.52
Tdrd9 8.59
Akr1c18 7.40
Nkd2 6.80
Kank4 6.03
Nptx2 6.02
Tescl 5.98
Ang2 5.92
Svop 5.87
Ccdc68 5.70
Cacna1g 5.63
Hal 5.58
Car12 5.56
Esm1 5.55
Rnf165 5.33
Ccl11 5.32
Fgf10 5.22
Pkp1 5.12
Slc26a4 5.08
Ism1 5.05
Gm6277 5.04
Hoxb9 5.02
Nxph4 4.97
Ano3 4.95
Tex11 4.91
Pcdhga9 4.91
Rims2 4.83
Dio3os 4.76
Wasf3 4.76

Fig. S1. Differentially expressed genes between WT and DKO macrophages. (**A**) A volcano plot showing differential gene expression in Epsin deficient (DKO) and wild type (WT) macrophages. Red and blue indicate up- and down-regulated genes, respectively. (**B**) A heatmap exhibits the expression values of up- and down-regulated genes in each sample. (**C**) Bar plots showing log2 fold changes of the top 30 up- and down-regulated genes between DKO and WT macrophages. Up- (red) and down-regulated (blue) genes are indicated.

Fig. S2

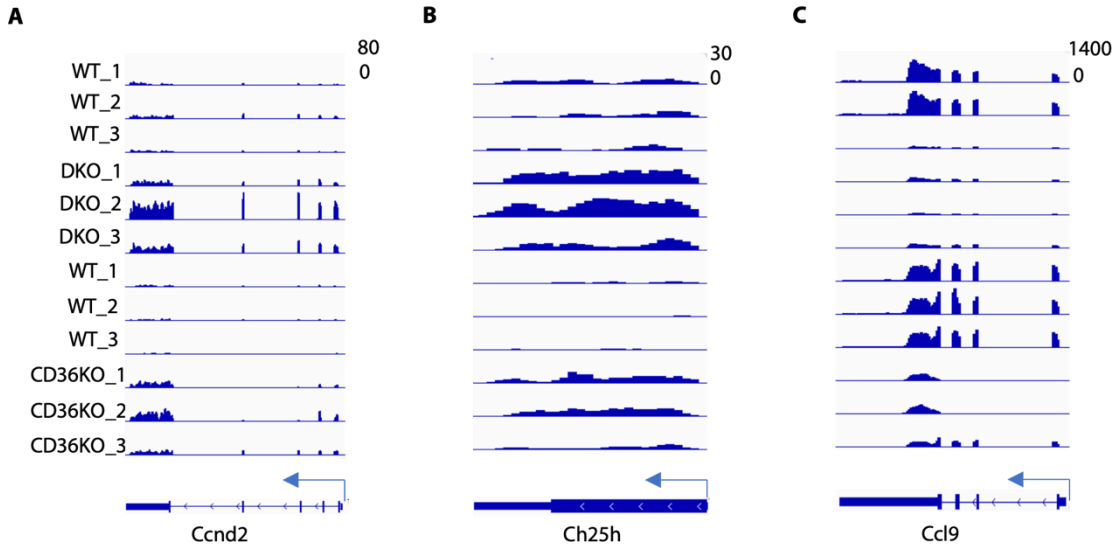

Fig. S2. Representative shared differentially expressed genes in DKO and CD36 knock out macrophage. (**A-C**) Genome browser tracks to show expression values of three representative genes. The arrows on the gene model indicate the direction of transcription.

Fig. S3

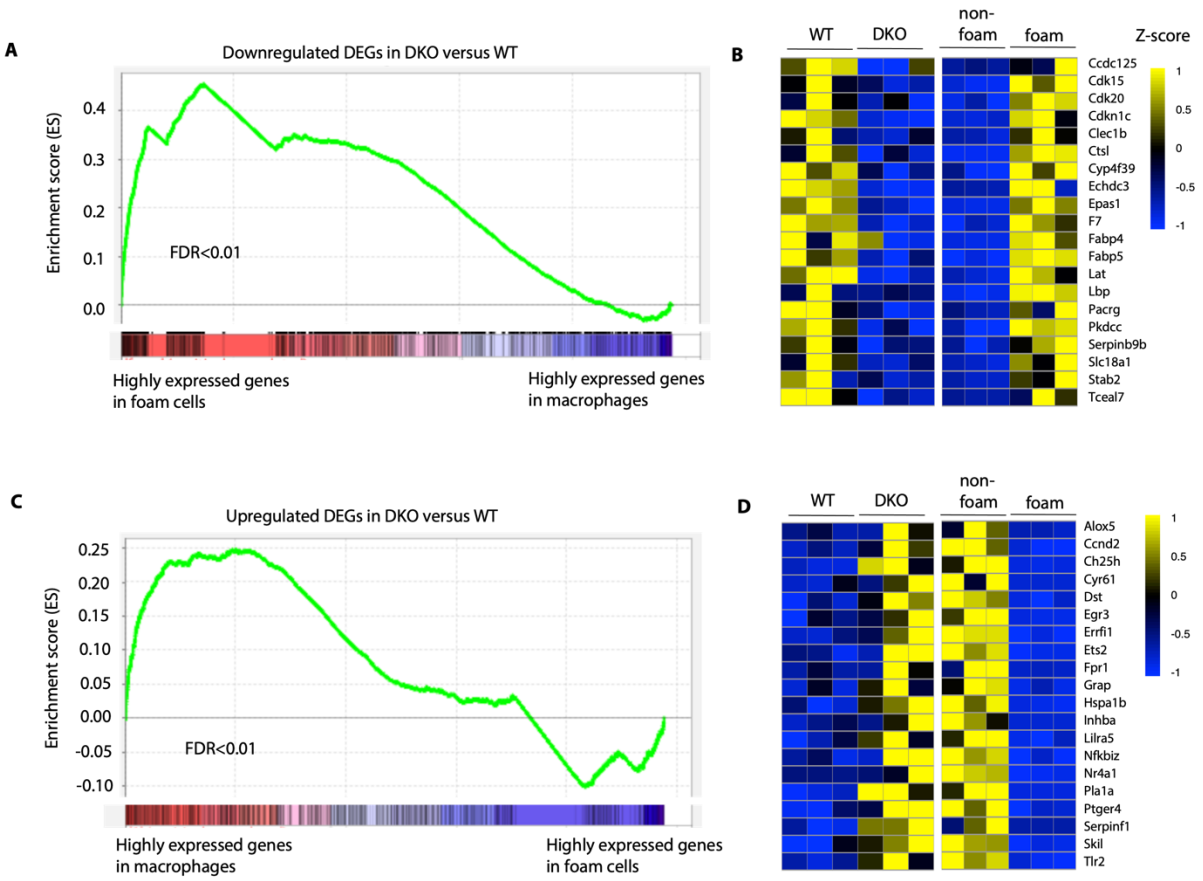

Fig. S3. Foam cell genes are downregulated in Epsin-deficient macrophages. (**A**) GSEA shows that downregulated genes in DKO versus WT tend to be expressed at higher levels in foam cells relative to normal macrophages (non-foam cells). (**B**) Genes downregulated in DKO compared to WT: The top 20 genes that were highly expressed in foam cells relative to normal macrophages were selected to plot expression values in the heatmap. (**C**) GSEA shows that the genes upregulated in DKO vs WT tend to be expressed at higher levels in macrophages relative to foam cells. (**D**) Among the genes upregulated in DKO compared to WT macrophages, the top 20 genes expressed at higher levels in macrophages relative to foam cells were selected to plot expression values in the heatmap.

Fig. S4

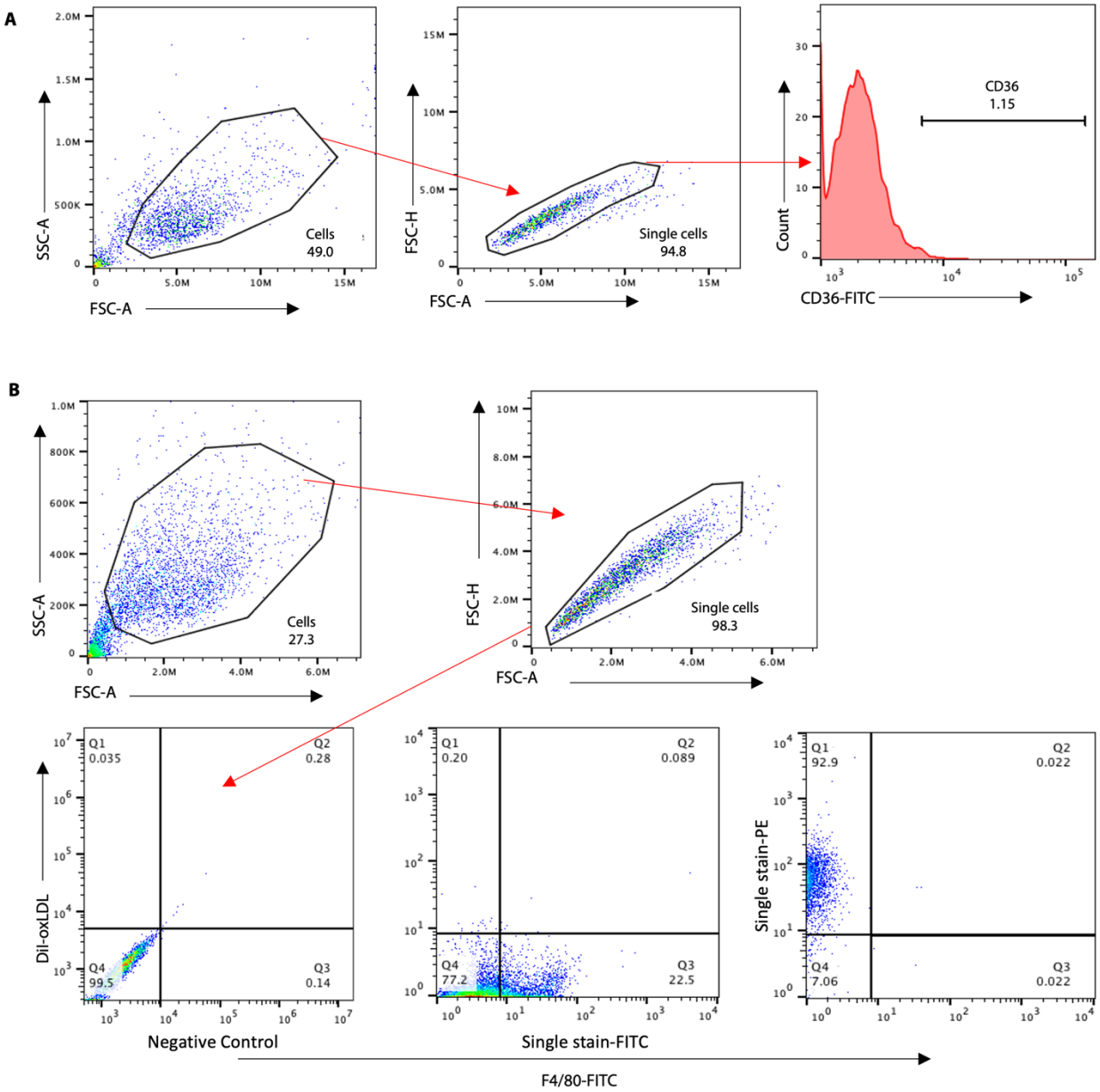
A
SSC-A
FSC-A
Cells
49.0
FSC-H
FSC-A
Single cells
94.8
Count
CD36-FITC
CD36
1.15
B
SSC-A
FSC-A
Cells
27.3
FSC-H
FSC-A
Single cells
98.3
Dil-oxLDL
Negative Control
Q1
0.035
Q2
0.28
Q4
99.5
Q3
0.14
Single stain-FITC
Q1
0.20
Q2
0.089
Q4
77.2
Q3
22.5
Single stain-PE
Q1
92.9
Q2
0.022
Q4
7.06
Q3
0.022
F4/80-FITC

Fig. S4. Gating strategy used in the flow cytometric evaluation for Fig. 2C and 2H. (**A**) Macrophages isolated from WT (n=6) and DKO (n=6) mice were incubated in lipid-deficient medium for 24h followed by treatment with oxLDL for 2h, then staining with CD36-Alex488 and cytometric analyses. (**B**) Macrophages isolated from WT (n=6) and DKO (n=6) mice were incubated in lipid-deficient medium for 24h followed by the treatment of 10 μg/mL Dil-oxLDL for 2h at 37^0C and assessed the uptake of lipoproteins by flow cytometry. The major macrophage population was selected in forward vs side scatter plots and single cell determination was performed by FSC-H vs FSC-A. CD36 (A) or DiI-oxLDL (B) positive macrophages were presented in Fig. 2C and 2H, respectively.

Fig. S5

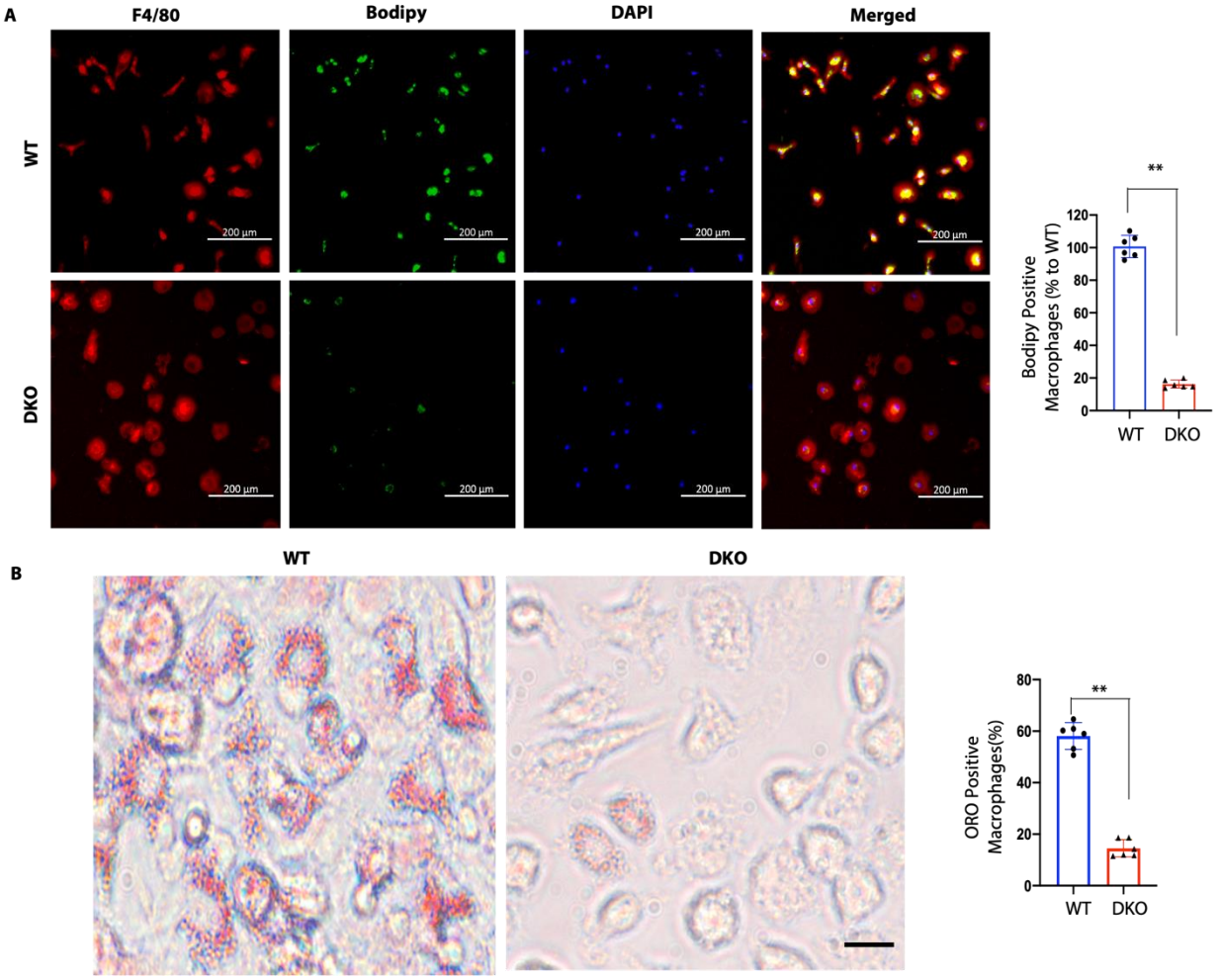

Fig. S5. The loss of Epsins reduced oxLDL uptake by macrophages. (**A**) Isolated peritoneal macrophages from WT (n=6) and DKO (n=6) mice were pre-incubated with 25μg/mL oxLDL for 24h in lipid-deficient medium and stained with BODIPY (lipids, green), F4/80 (macrophage, red), and DAPI (blue), **WT vs DKO group, n=6, P<0.01, scale bar=200μm. (**B**) ORO staining of peritoneal macrophages, which were pre-incubated with 25μg/mL oxLDL for 24h in lipid-deficient medium, **WT vs DKO group, n=6, P<0.01, scale bar=20μm. Data are presented as mean ± SD and were analyzed using an unpaired Student's t-test.

Fig. S6

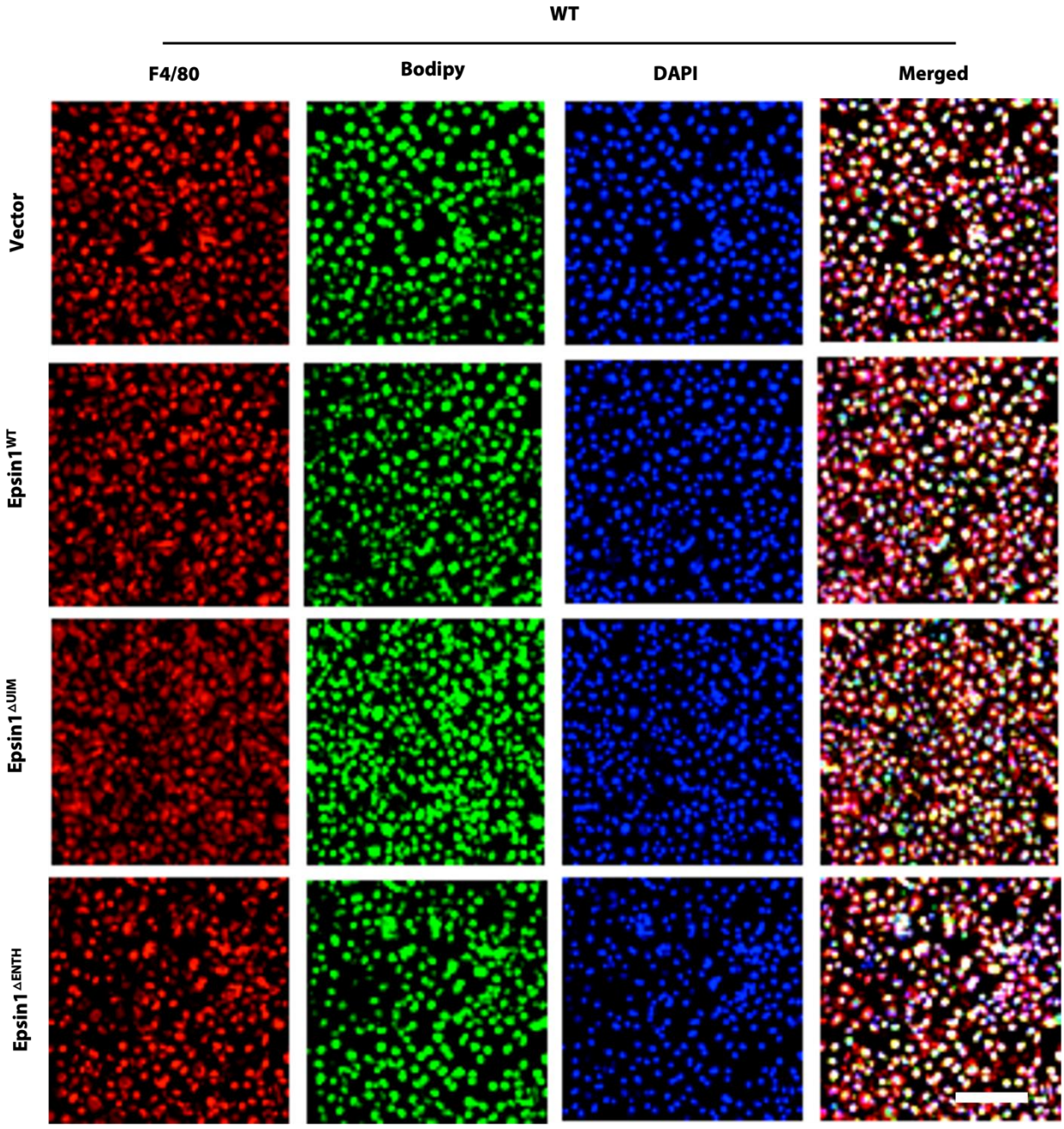
WT
F4/80
Bodipy
DAPI
Merged
Vector
Epsin1WT
Epsin1ΔUIM
Epsin1ΔENTH

Fig. S6. Transfection of full-length Epsin1 and constructs with the ENTH and UIM domains deleted into WT macrophages did not affect lipid uptake. Constructs of FLAG-Epsin1 WT, △ENTH, and △UIM were transfected into ApoE$^{-/-}$/WT macrophages for 48h and treated with 100 μg/mL oxLDL for 1h, followed by staining with F4/80 (red), BODIPY (green) and DAPI (blue). Scale bars=200μm. Statistical analyses are presented in Fig. 3E.

Fig. S7

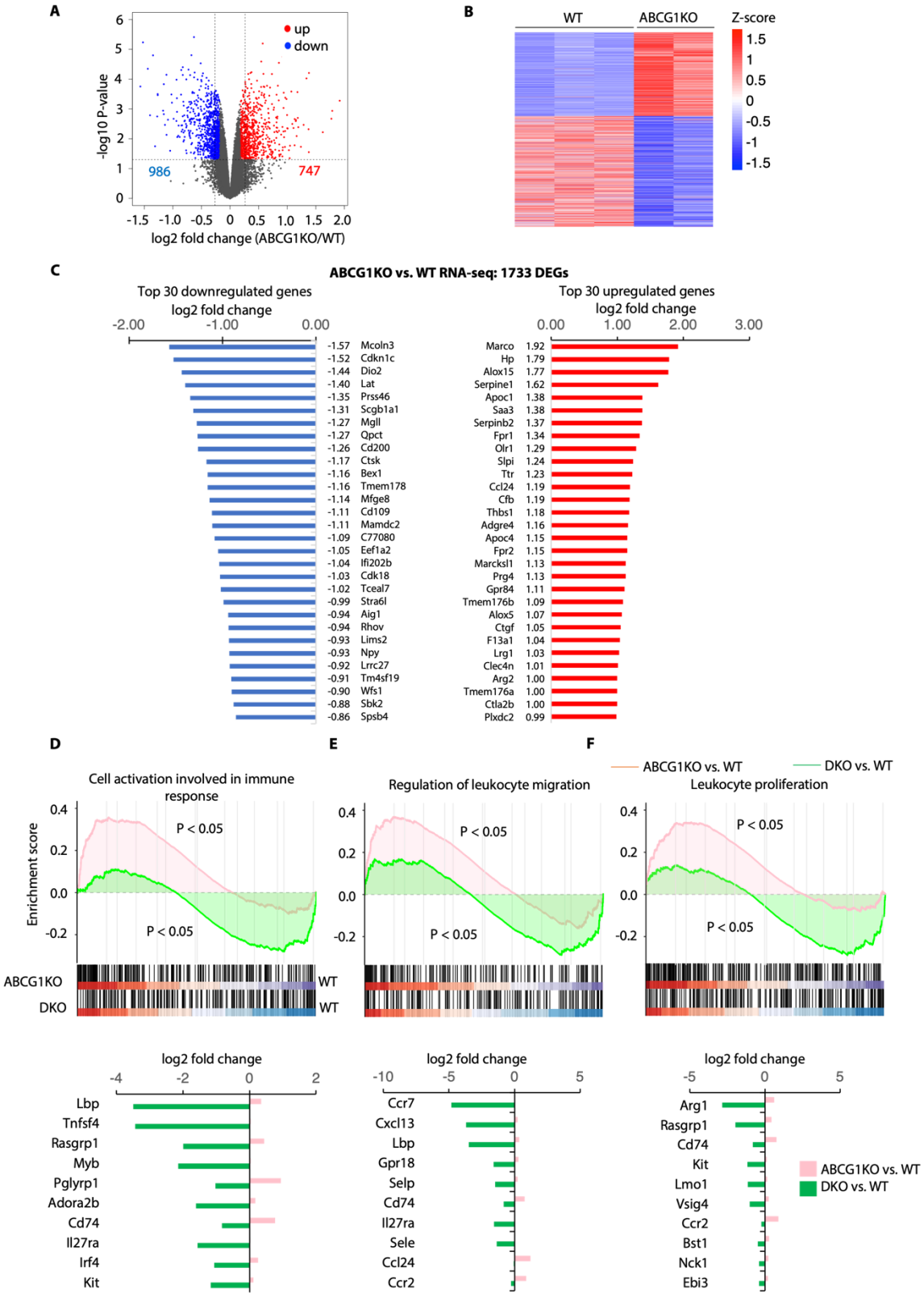
A
up
down
-log10 P-value
986
747
log2 fold change (ABCG1KO/WT)
B
WT
ABCG1KO
Z-score
C
ABCG1KO vs. WT RNA-seq: 1733 DEGs
Top 30 downregulated genes
log2 fold change
Top 30 upregulated genes
log2 fold change
D
Cell activation involved in immune response
E
Regulation of leukocyte migration
F
Leukocyte proliferation
ABCG1KO vs. WT
DKO vs. WT
Enrichment score
P < 0.05
ABCG1KO
DKO
WT
log2 fold change
Lbp
Tnfsf4
Rasgrp1
Myb
Pglyrp1
Adora2b
Cd74
Il27ra
Irf4
Kit
Ccr7
Cxcl13
Lbp
Gpr18
Selp
Cd74
Il27ra
Sele
Ccl24
Ccr2
Arg1
Rasgrp1
Cd74
Kit
Lmo1
Vsig4
Ccr2
Bst1
Nck1
Ebi3
ABCG1KO vs. WT
DKO vs. WT

1381

Fig. S7. Differentially expressed genes between WT and ABCG1 knockout (ABCG1KO) macrophages. (**A**) A volcano plot showing differential gene expression in ABCG1KO and WT macrophages. Red and blue indicate up- and down-regulated genes, respectively. (**B**) A heatmap exhibiting the expression values of up- and down-regulated genes in each sample. (**C**) Bar plots showing log2 fold changes of the top 30 up- and down-regulated genes between ABCG1KO and WT macrophages. Up- (red) and down-regulated (blue) genes are indicated. (**D-F**) GSEA (top panels) indicated the tendency of individual pathways to be up- or down-regulated in response to DKO or ABCG1KO compared to WT cells. Genes associated with cell activation involved in immune response (GO:0002263) (D), regulation of leukocyte migration (GO:0002685) (E), and leukocyte proliferation (GO:0070661) (F) were analyzed. The bar plots (bottom panels) showing log2 fold change of altered genes in these pathways.

Fig. S8

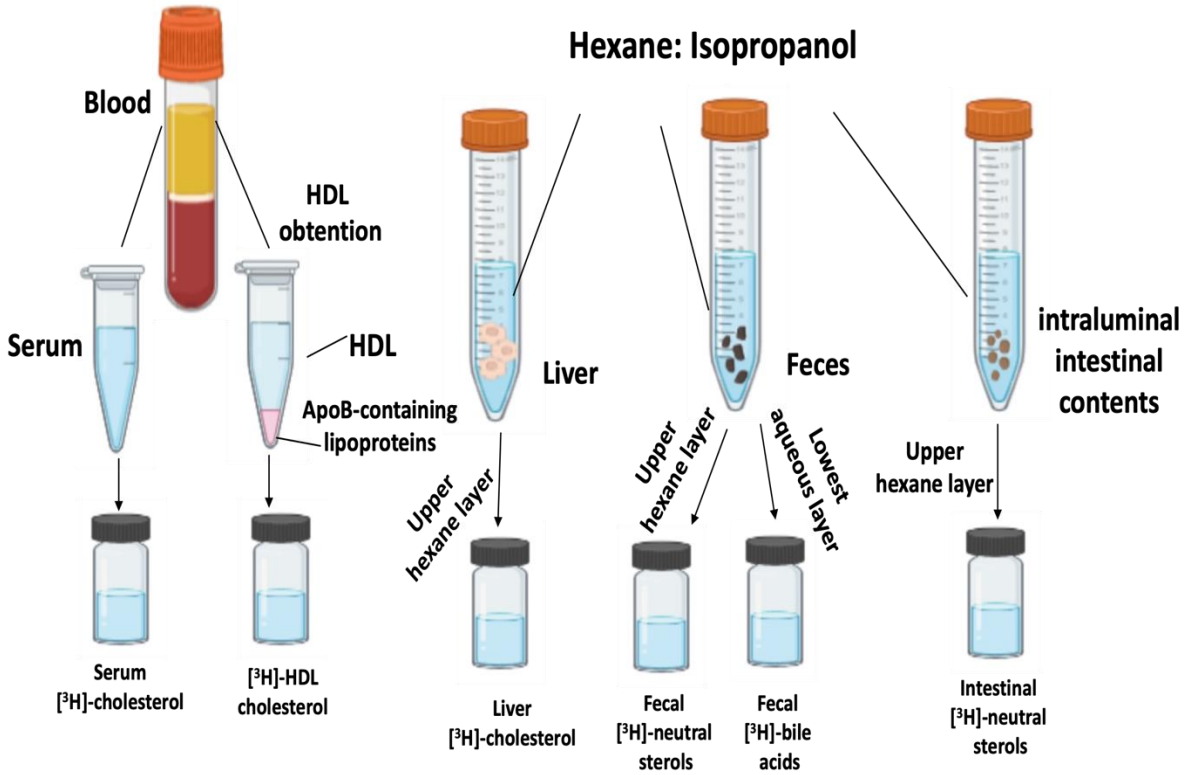

Fig. S8. Schematic of the quantification for radiolabeled cholesterol. [^{3}H]-cholesterol was measured in serum and HDL after precipitating ApoB-containing lipoproteins. Liver, feces and intestinal lipids were extracted with hexane–isopropanol and partitioned against Na_2SO_4. Liver [^{3}H]-radioactivity was determined in the upper layer, which contains the [^{3}H]-cholesterol. In the feces extract, the amount of [^{3}H]-radioactivity was determined in the upper layer (neutral sterols) and the lowest layer (bile acids). In the intestinal contents, [^{3}H]-radioactivity was determined in the upper layer.

Fig. S9

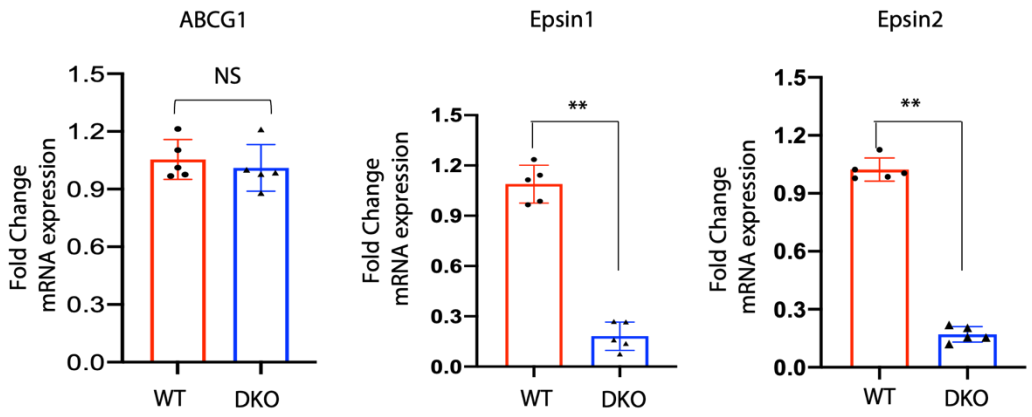

Fig. S9. Gene expression levels of indicated genes in WT and DKO macrophage. Peritoneal macrophages were isolated from WT (n=5) and DKO (n=5) mice. Total RNA was extracted and mRNA levels of ABCG1, Epsin1, and Epsin2 were measured (NS=no significant difference, ** WT vs DKO group, n=5, P<0.01). Data are presented as mean ± SD and analyzed using an unpaired Student's t-test.

Fig. S10

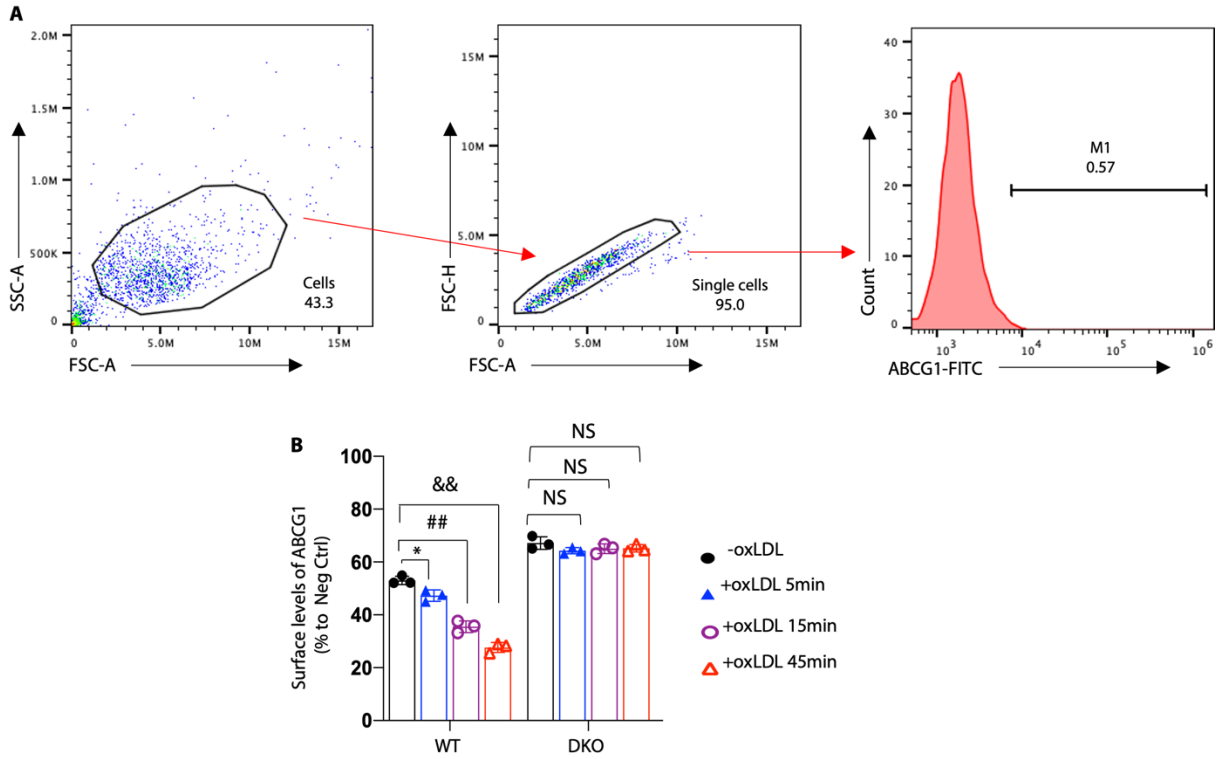

Fig. S10. Gating strategy used in the flow cytometric evaluation for Fig. 6C. (**A**) Macrophages isolated from WT and DKO mice were incubated in lipid-deficient medium and treated with LXR agonist for 24h followed by treatment with or without 100 μg/mL oxLDL for 5min, 15min, and 45min, and then stained with ABCG1. Surface levels of ABCG1 were assessed by flow cytometry. The major macrophage population was selected in forward versus side scatter plots and single cell determination was performed by FSC-H vs FSC-A. Isotype controls were gated in the histogram as M1 for the negative control of experimental groups. (**B**) Statistical analysis is presented for Fig. 6C. At least three independent experiments were performed for statistical analysis (*-oxLDL vs +oxLDL 5min, $P<0.05$; $^{\#\#}$-oxLDL vs +oxLDL 15min, $P<0.01$; $^{\&\&}$-oxLDL vs +oxLDL 45min, $P<0.01$). Data are presented as mean ± SD and analyzed using one-way ANOVA.

Fig. S11

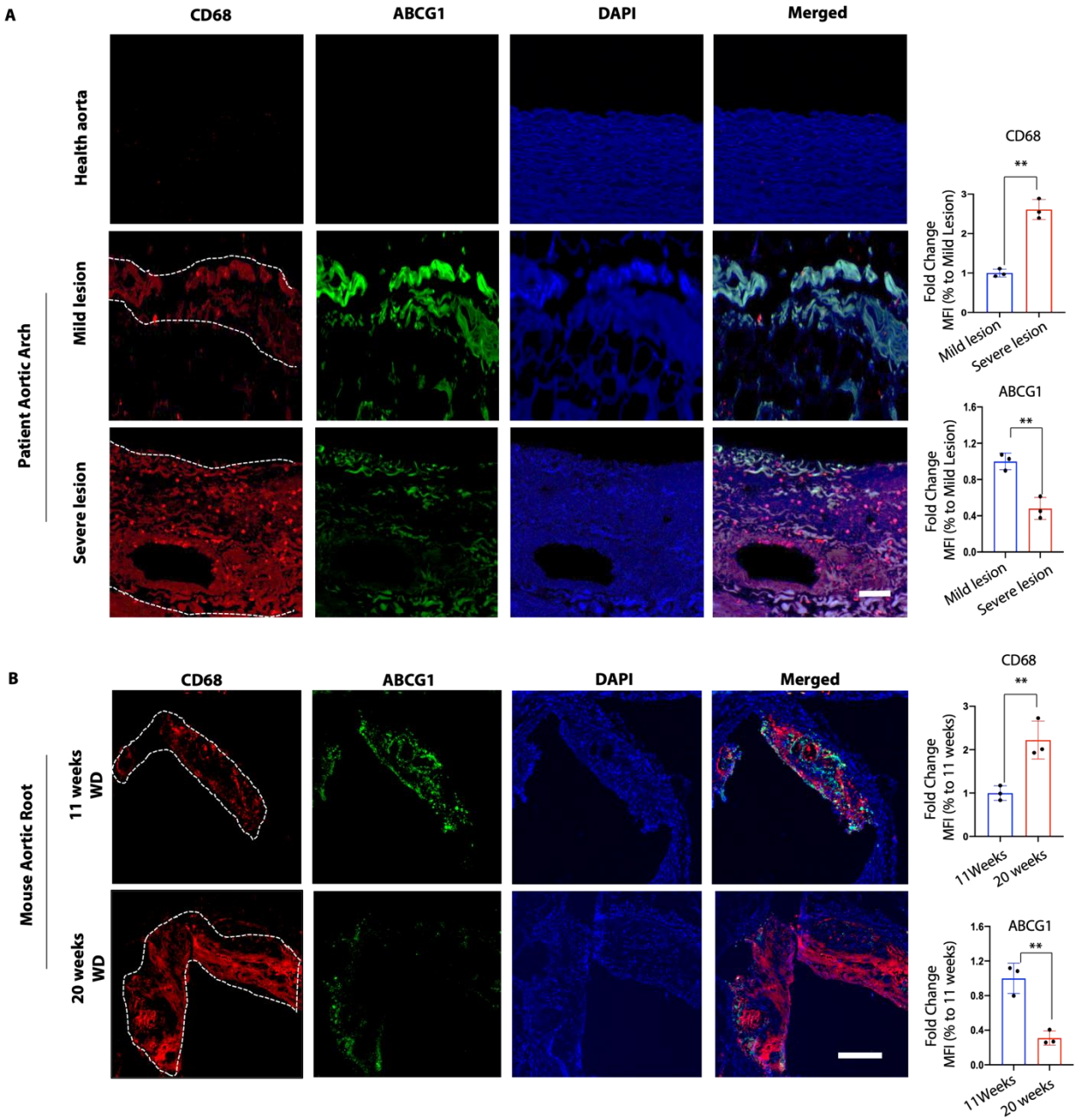

1427

1428

1429

1430

Fig. S11. The expression of ABCG1 decreased with progression of atherosclerotic lesions in humans and mice. (**A-B**) Immunostaining of CD68 (red), ABCG1(green) and DAPI (blue) of human patient aortic arch sections (A, n=3) and mouse aortic root sections (B, n=3) in early and advanced stage of atherosclerosis （white dashed line outlined in CD68). Mean fluorescence intensity (MFI), **Mild vs Severe lesion, P<0.01, scale bar, A=50μm, B=200μm. Data are presented as mean ± SD and were analyzed using an unpaired Student's t-test.

Fig. S12

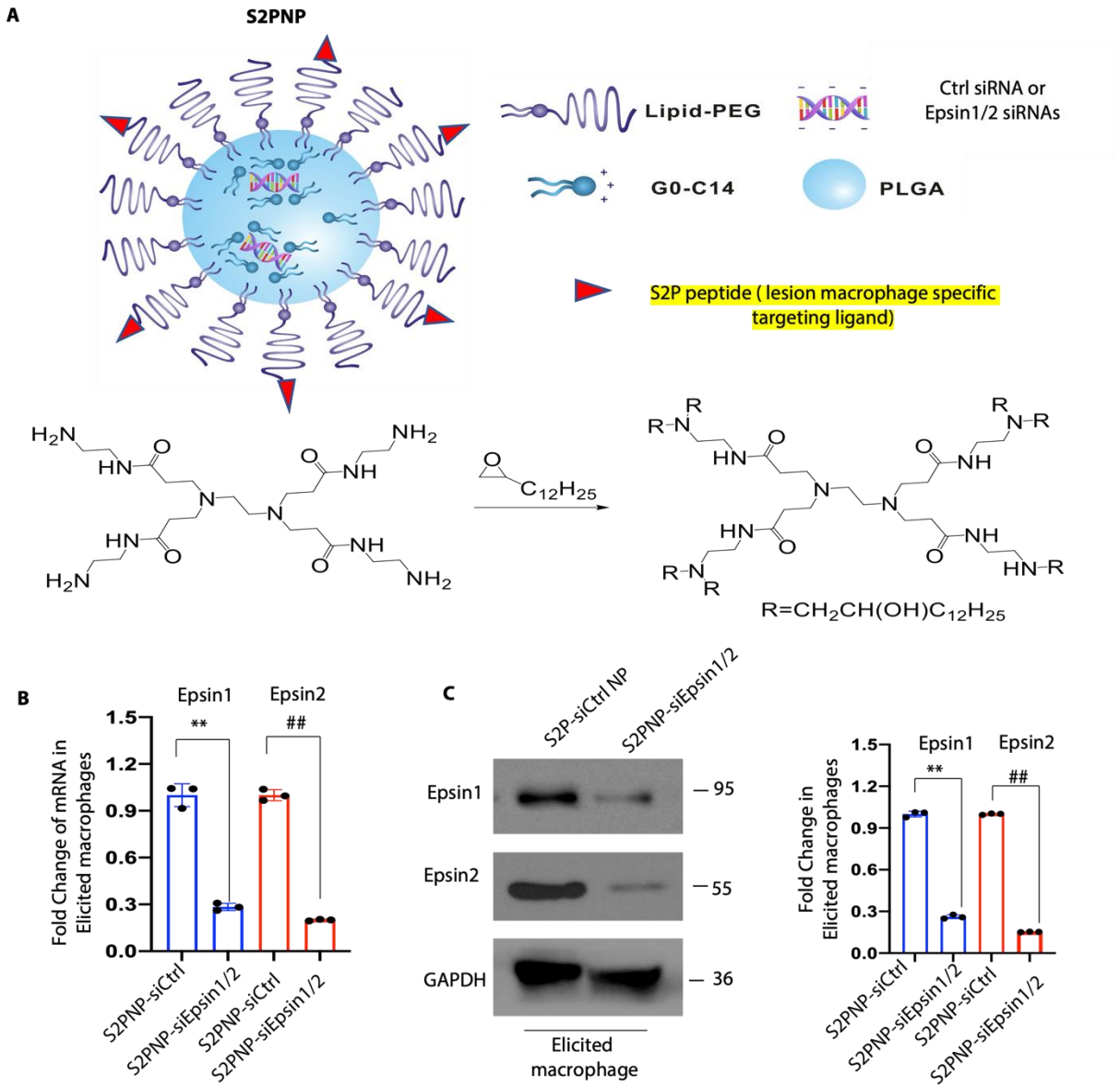
A
S2PNP
Lipid-PEG
Ctrl siRNA or
Epsin1/2 siRNAs
G0-C14
PLGA
S2P peptide (lesion macrophage specific targeting ligand)
R=CH2CH(OH)C12H25
B
Epsin1
Epsin2
Fold Change of mRNA in Elicited macrophages
S2PNP-siCtrl
S2PNP-siEpsin1/2
C
S2P-siCtrl NP
S2PNP-siEpsin1/2
Epsin1
Epsin2
GAPDH
95
55
36
Elicited macrophage
Fold Change in Elicited macrophages

Fig. S12. Characterization and silencing efficacy of S2P-conjugated siEpsin1/2 NPs. (**A**) Schematic of the targeted hybrid siRNA NP platform composed of a lipid-PEG shell with a lesion macrophage specific targeting ligand, S2P peptide, and a PLGA core. (**B-C**) Macrophages from WT mice were treated with S2PNP-siCtrl or S2PNP-siEpsin1/2 for 24h, RNA and proteins were isolated, qRT-PCR (B) and western blot (C) was performed to check the expression of Epsin 1 and 2 levels (n=3), **S2PNP-siCtrl vs S2PNP-siEpsin1/2 for Epsin1 expression, $P<0.01$; ##S2PNP-siCtrl vs S2PNP-siEpsin1/2 for Epsin2 expression, $P<0.01$. Data are presented as mean ± SD and analyzed using an unpaired Student's t-test.

Fig. S13

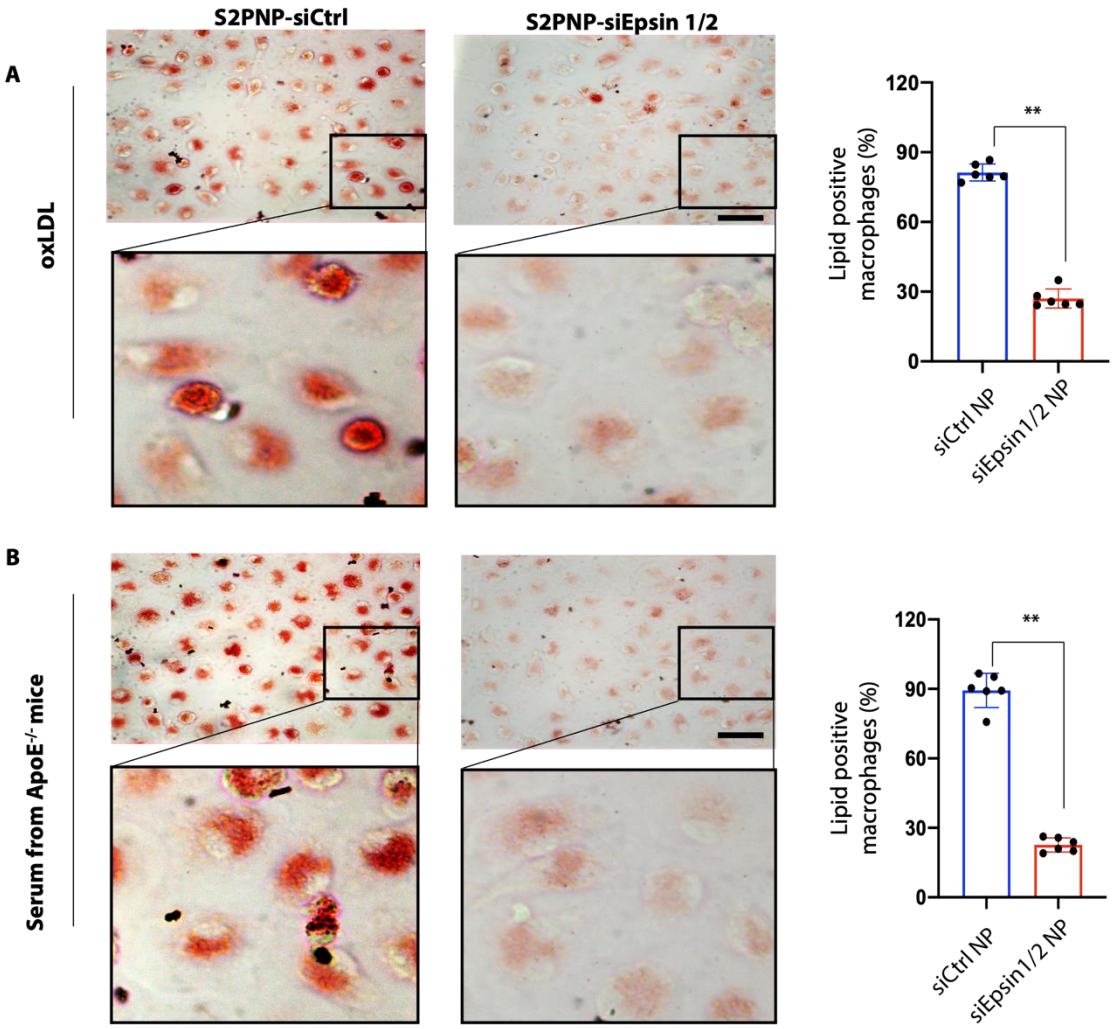

1455

1456 **Fig. S13. S2PNP-siEpsin1/2 treated macrophages show reduced foam cell formation**. (**A-B**)
1457 Macrophages isolated from ApoE$^{-/-}$ mice were incubated in lipid-deficient medium and treated
1458 with S2PNP-siCtrl or S2PNP-siEpsin1/2 for 48h, follow with treatment of 100 μg/mL oxLDL (A)
1459 or serum (B) collected from ApoE$^{-/-}$ mice fed a WD for 8 weeks. ORO staining was performed (**
1460 S2PNP-siCtrl vs S2PNP-siEpsin1/2 group, n=6, P<0.01, scale bar=50μm). Data are presented as
1461 mean ± SD and analyzed using an unpaired Student's t-test.

1462

Fig. S14

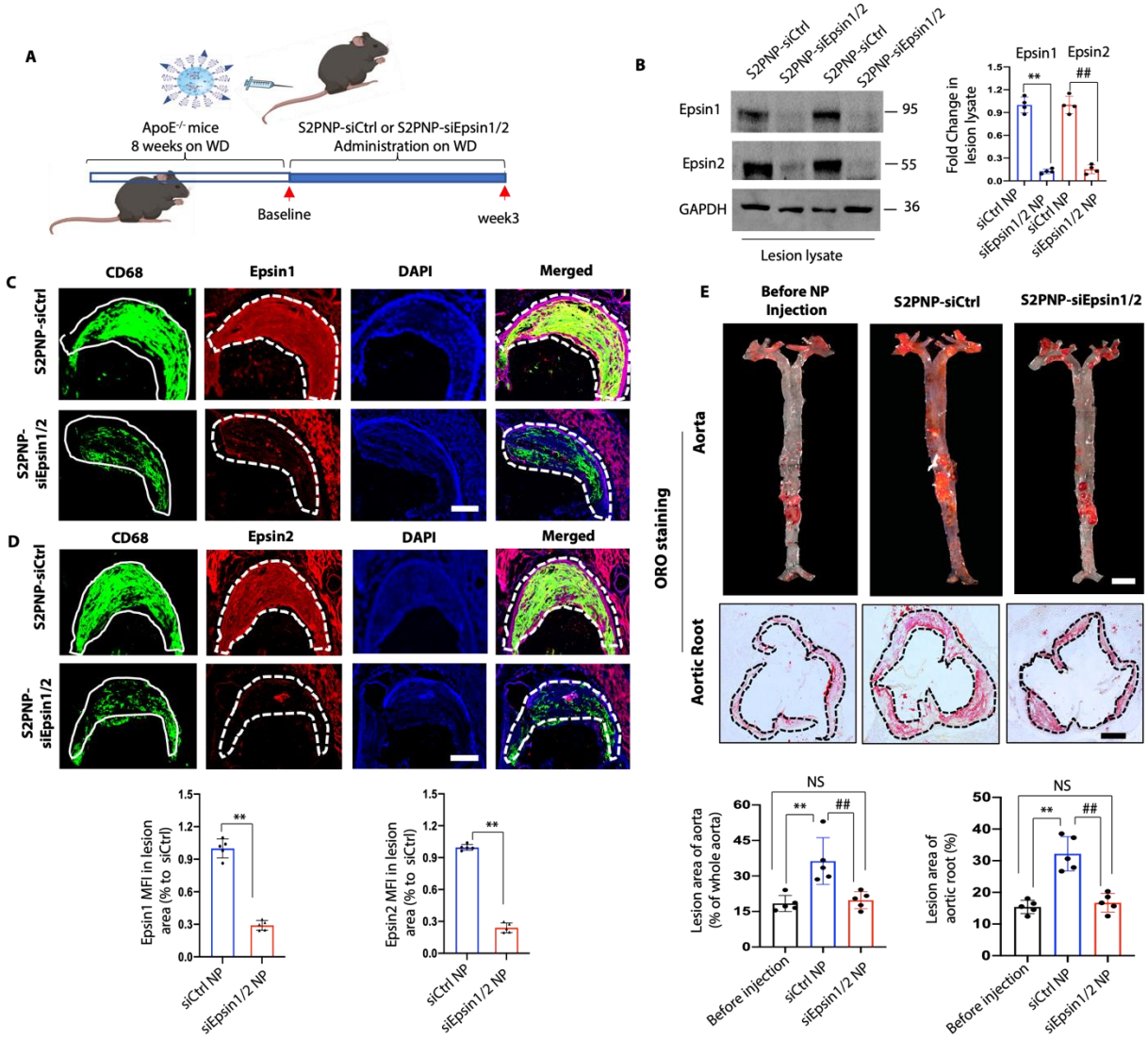
A
ApoE-/- mice
8 weeks on WD
S2PNP-siCtrl or S2PNP-siEpsin1/2
Administration on WD
Baseline
week3
B
S2PNP-siCtrl
S2PNP-siEpsin1/2
S2PNP-siCtrl
S2PNP-siEpsin1/2
Epsin1
Epsin2
GAPDH
95
55
36
Lesion lysate
Epsin1
Epsin2
Fold Change in lesion lysate
siCtrl NP
siEpsin1/2 NP
siCtrl NP
siEpsin1/2 NP
C
CD68
Epsin1
DAPI
Merged
S2PNP-siCtrl
S2PNP-siEpsin1/2
D
CD68
Epsin2
DAPI
Merged
S2PNP-siCtrl
S2PNP-siEpsin1/2
Epsin1 MFI in lesion area (% to siCtrl)
Epsin2 MFI in lesion area (% to siCtrl)
siCtrl NP
siEpsin1/2 NP
E
Before NP Injection
S2PNP-siCtrl
S2PNP-siEpsin1/2
ORO staining
Aorta
Aortic Root
Lesion area of aorta (% of whole aorta)
Lesion area of aortic root (%)
NS
Before injection
siCtrl NP
siEpsin1/2 NP

Fig. S14. S2PNP-siEpsin1/2 inhibits lesion formation and macrophage accumulation in early stage of atherosclerosis. (**A**) ApoE$^{-/-}$ mice were fed a WD for 8 weeks followed by treatment with S2PNP-siCtrl or S2PNP-siEpsin1/2 for 3 weeks (2 doses per week). (**B**) WB of Epsin 1 and 2 after treatment with S2PNP-siCtrl or S2PNP-siEpsin1/2 NPs using lesional lysates from the aortas (n=4 times, **S2PNP-siCtrl vs S2PNP-siEpsin1/2 for Epsin1, P<0.01; ##S2PNP-siCtrl vs S2PNP-siEpsin1/2 for Epsin2, P<0.01). (**C-D**) Aortic roots from S2PNP-siCtrl treated ApoE$^{-/-}$ or S2PNP-siEpsin1/2 siRNA treated ApoE$^{-/-}$ mice were stained with the macrophage marker CD68 (solid white line) and Epsin1 or Epsin2 (dashed white line), Epsin 1 and 2 mean fluorescence intensity (MFI) were analyzed (n=5, **S2PNP-siCtrl vs S2PNP-siEpsin1/2 for Epsin1, P<0.01, scale bars=500 μm). Data from B-D are presented as mean ± SD and analyzed using an unpaired Student's t-test. (**E**) *En face* ORO staining of aortas (upper panel) and aortic root sections (lower panel) of hearts from baseline, S2PNP-siCtrl or S2PNP-siEpsin1/2 treated ApoE$^{-/-}$ mice fed a WD. Lesion area was analyzed using one-way ANOVA (n=5, **S2PNP-siCtrl vs baseline, P<0.01, ##S2PNP-siCtrl vs S2PNP-siEpsin1/2 group P<0.01, Scale bar; aorta=5mm, aortic root=500μm). Data from E are presented as mean ± SD and were analyzed using one-way ANOVA.

Fig. S15

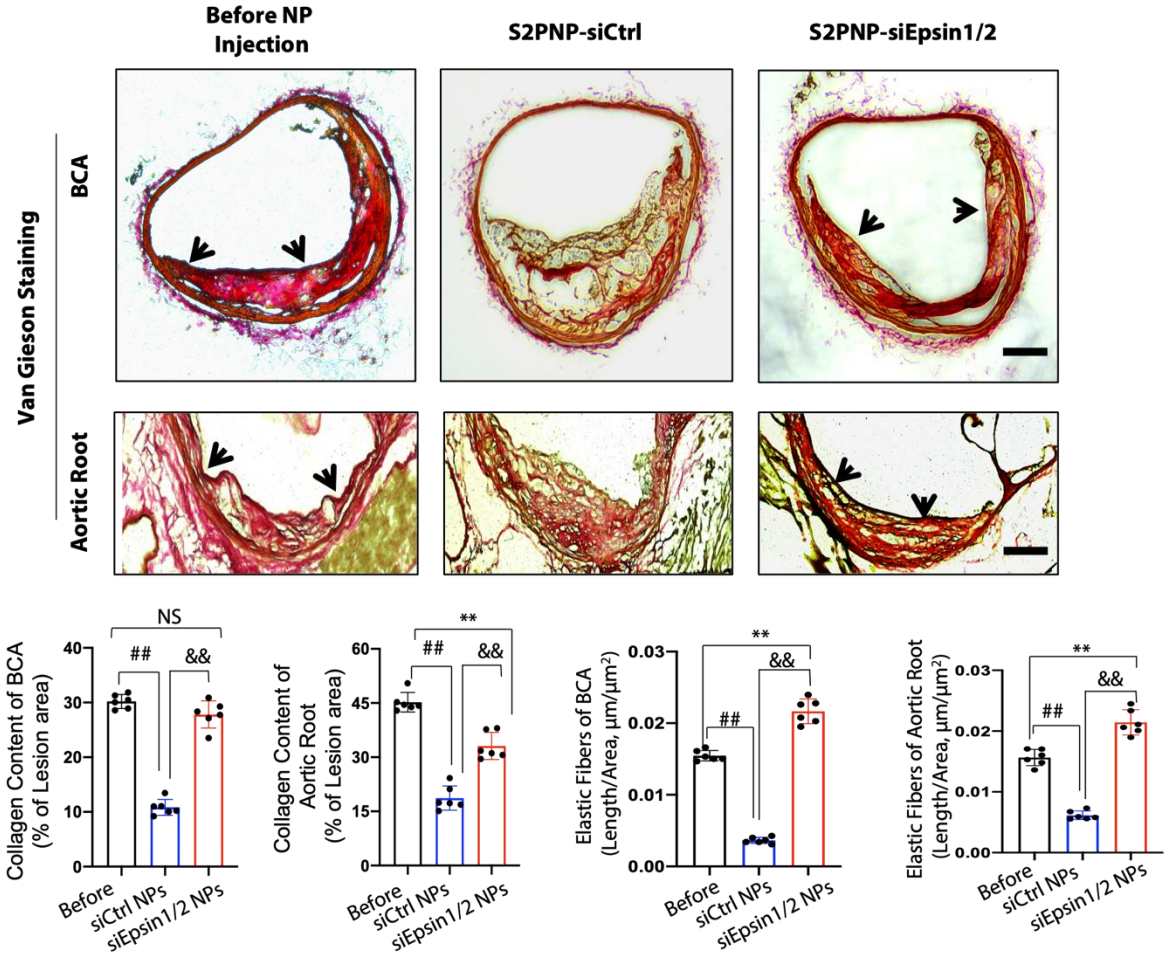
Before NP Injection
S2PNP-siCtrl
S2PNP-siEpsin1/2
Van Gieson Staining
BCA
Aortic Root
Collagen Content of BCA (% of Lesion area)
Collagen Content of Aortic Root (% of Lesion area)
Elastic Fibers of BCA (Length/Area, μm/μm²)
Elastic Fibers of Aortic Root (Length/Area, μm/μm²)
NS
**
##
&&
Before
siCtrl NPs
siEpsin1/2 NPs

Fig. S15. Silencing lesional macrophage Epsin1/2 by S2PNP-siEpsin1/2 NP-treatment stabilized plaques in a progression model of atherosclerosis. ApoE$^{-/-}$ mice fed a WD for 17 weeks followed by treatment with S2PNP-siCtrl or S2PNP-siEpsin1/2 for 3 weeks (two doses per week). Van Gieson's staining of brachiocephalic artery (BCA) (upper panel) and aortic root (lower panel) sections from baseline, S2PNP-siCtrl-, or S2PNP-siEpsin1/2-treated ApoE$^{-/-}$ mice was performed (arrows indicate the elastic fibers, n=6, **baseline vs S2PNP-siEpsin1/2 group, P<0.01; ##baseline vs S2PNP-siCtrl group, P<0.01; &&S2PNP-siCtrl vs S2PNP-siEpsin1/2 group, P<0.01, scale bar=250 μm). Data are presented as mean ± SD and were analyzed using one-way ANOVA.

Fig. S16

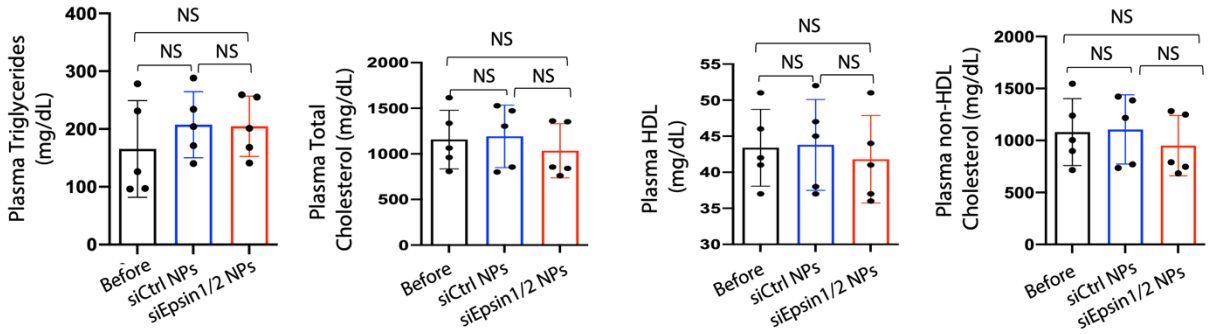

Fig. S16. Delivery of S2PNP-siEpsin1/2 does not change cholesterol and triglyceride levels of ApoE$^{-/-}$ mice fed a WD. Plasma from ApoE$^{-/-}$ mice fed a WD for 17 weeks (before NP injection), followed by an additional 3 weeks of treatment with S2PNP-siCtrl or S2PNP-siEspsin1/2, showed no alteration in triglyceride, cholesterol, HDL and non-HDL (LDL/VLDL) cholesterol levels (n=5; NS, no significant difference). Data are presented as mean ± SD and were analyzed using a one-way ANOVA.

Fig. S17

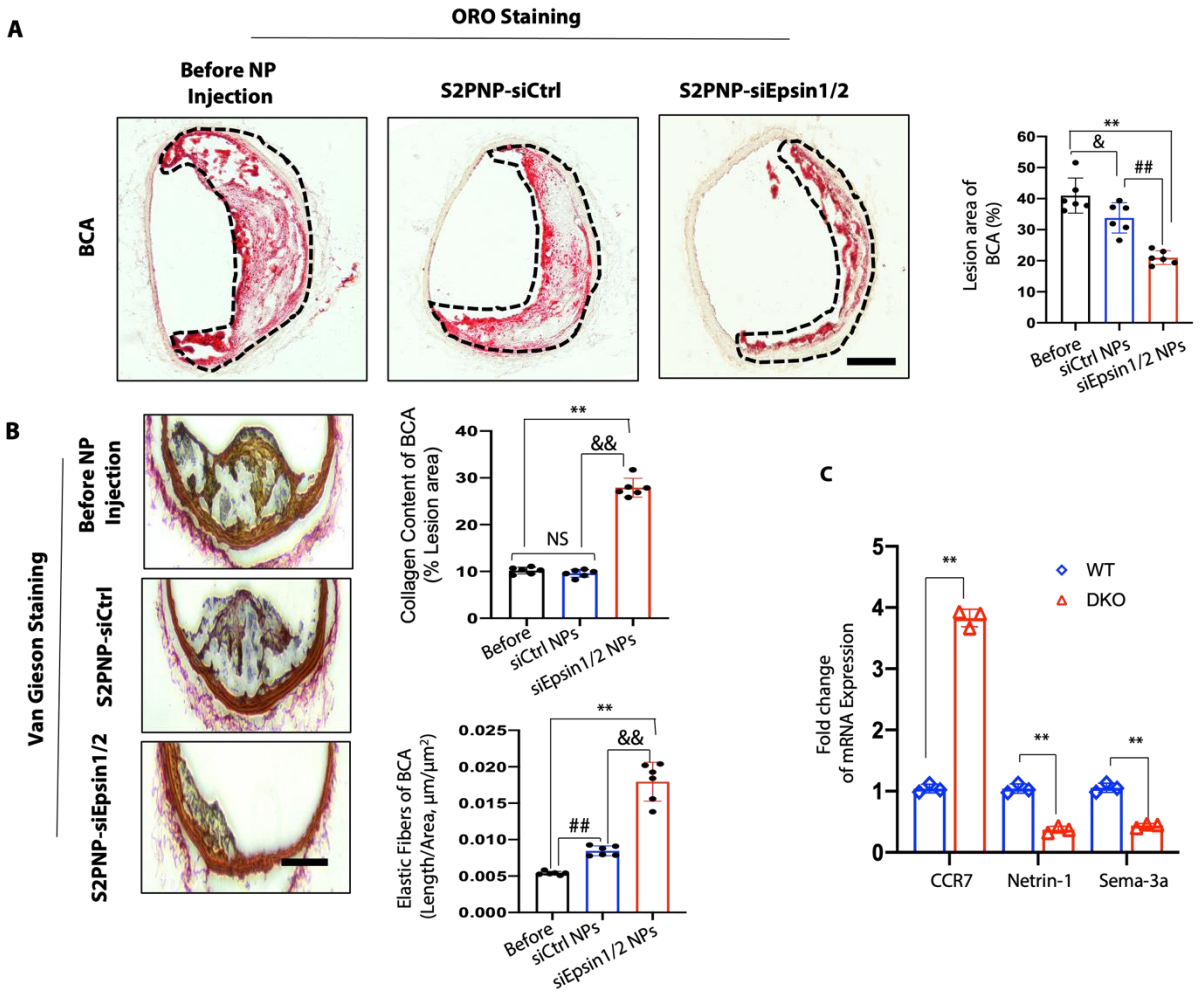
A
ORO Staining
Before NP Injection
S2PNP-siCtrl
S2PNP-siEpsin1/2
BCA
Lesion area of BCA (%)
Before
siCtrl NPs
siEpsin1/2 NPs
B
Van Gieson Staining
Before NP Injection
S2PNP-siCtrl
S2PNP-siEpsin1/2
Collagen Content of BCA (% Lesion area)
Elastic Fibers of BCA (Length/Area, μm/μm²)
NS
C
WT
DKO
Fold change of mRNA Expression
CCR7
Netrin-1
Sema-3a

Fig. S17. Silencing macrophage Epsin1/2 by S2PNP-siEpsin1/2 NPs reduces lesion size in a regression model of atherosclerosis. (**A**) ORO staining of BCA sections in baseline, S2PNP-siCtrl or S2PNP-siEpsin1/2 treated PCSK9-mice was performed and lesions were indicated (dash lines) (n=6, **Baseline vs S2PNP-siEpsin1/2 group, P<0.01; $^{\&}$Baseline vs S2PNP-siCtrl group, P<0.05; $^{\#\#}$S2PNP-siEpsin1/2 vs S2PNP-siCtrl group, P<0.01; scale bar=500μm). (**B**) Van Gieson's staining of BCA sections from above three groups was performed (n=6, **Baseline vs S2PNP-siEpsin1/2 group, P<0.01; $^{\#\#}$Baseline vs S2PNP-siCtrl group, P<0.01; $^{\&\&}$S2PNP-siEpsin1/2 vs S2PNP-siCtrl, P<0.01; scale bar=500μm). Data in A and B are presented as mean ± SD and analyzed using one-way ANOVA. (**C**) qRT-PCR analysis to confirm expression of the indicated genes (n=3, **DKO vs WT group, P<0.01). Data are presented as mean ± SD and analyzed using an unpaired Student's t-test.

Fig. S18

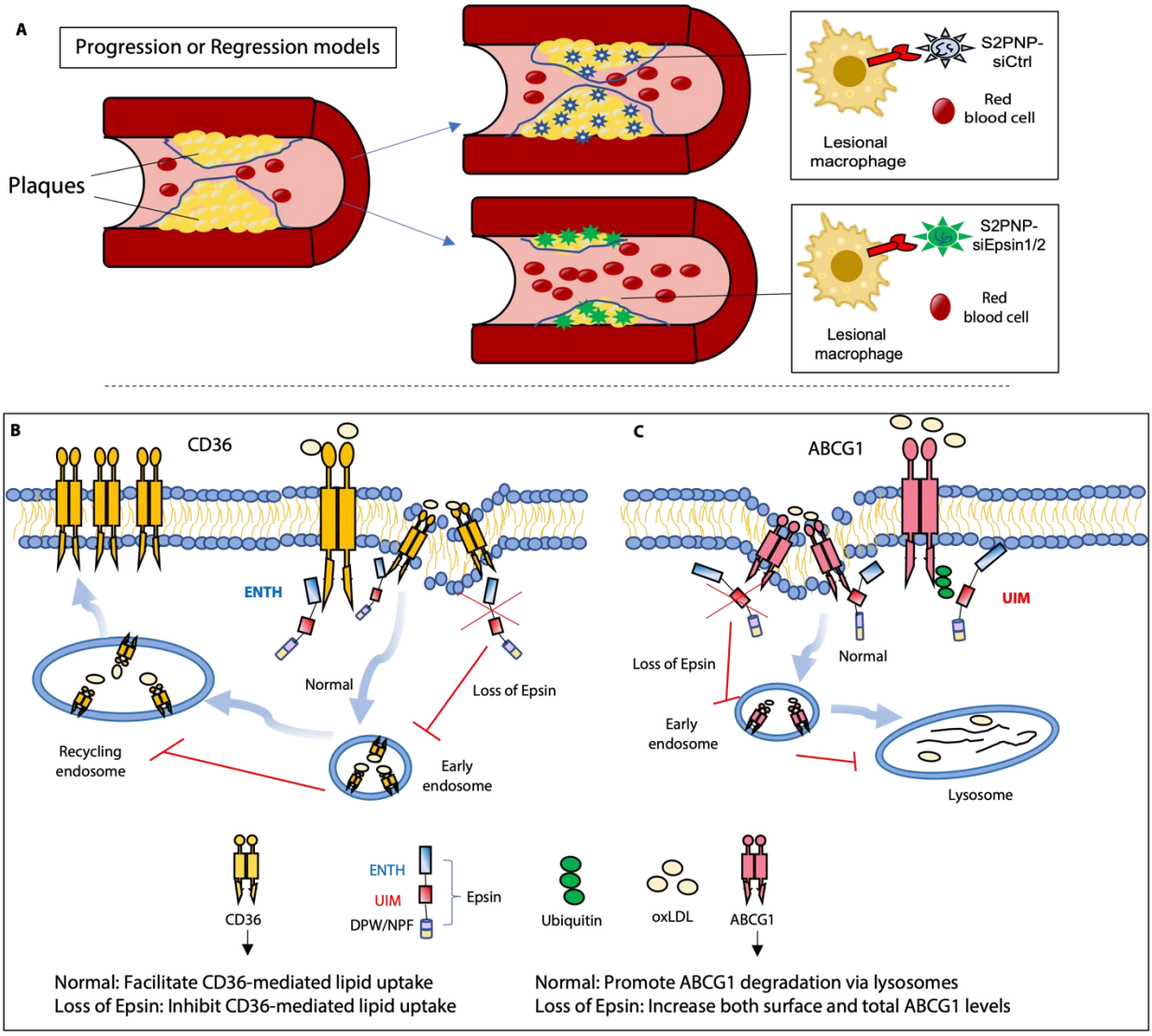
A
Progression or Regression models
Plaques
S2PNP-siCtrl
Red blood cell
Lesional macrophage
S2PNP-siEpsin1/2
Red blood cell
Lesional macrophage
B
CD36
ENTH
Normal
Loss of Epsin
Recycling endosome
Early endosome
C
ABCG1
UIM
Loss of Epsin
Normal
Early endosome
Lysosome
CD36
ENTH
UIM
DPW/NPF
Epsin
Ubiquitin
oxLDL
ABCG1
Normal: Facilitate CD36-mediated lipid uptake
Loss of Epsin: Inhibit CD36-mediated lipid uptake
Normal: Promote ABCG1 degradation via lysosomes
Loss of Epsin: Increase both surface and total ABCG1 levels

Fig. S18. Summary schematic diagram of the study. (A) In the progression model of atherosclerosis, the plaque size and lesions increase in the artery on western diet feeding. The delivery of S2PNP-siEpsin1/2 significantly slowed the progression of atherosclerosis compared to S2PNP-siCtrl group. In the regression model of atherosclerosis, plaque size and lesion area were dramatically reduced with the intravenously injection of S2PNP-siEpsin1/2. (**B-C**). Under the stimuli of oxLDL, Epsin binds to CD36 and ABCG1 through Epsin ENTH and Epsin UIM domains, respectively. In B, Epsin facilitates CD36-mideated lipid uptake via recycling endosomes. The loss of Epsin impairs the internalization of CD36, which results in reduced lipid uptake. While in C, Epsin promotes endocytic degradation of ABCG1via lysosomes, which leads to reduced total and surface level of ABCG1.

1562 **Table S1. List of reagents and animal models**

REAGENT or RESOURCE	SOURCE	Note
Primary Antibodies		
Rabbit polyclonal anti-Epsin1	Home made	N/A
Rabbit polyclonal anti-Epsin2	Abcam	Cat# ab74942
Rabbit polyclonal anti-Epsin2	Home made	N/A
Rat monoclonal Anti-mouse /SR-B3CD36	R & D System	Cat# MAB2519,
Rabbit monoclonal anti-CD36	Invitrogen	Cat# VL3153825
Mouse monoclonal anti-GAPDH	Santa Cruz Biotechnology	Cat# F118, sc166545
Mouse monoclonal anti-ubiquitin	Cytoskeleton, Inc	Cat# AUB01
Rabbit polyclonal anti-ABCA1	Novus Biologicals	NB400-105SS
Rabbit polyclonal anti-ABCG1	Novus Biologicals	NB400-132B,
Rabbit monoclonal anti-ABCG1	Invitrogen	Cat# VK3126422
Goat polyclonal anti mouse LDLR	R & D System	Cat# AF2255
Rat monoclonal Anti-mouse SRA1	R & D System	Cat# MAB1797
Monoclonal anti-Flag	Sigma-Aldrich	Cat# F3165
Rat monoclonal anti-F4/80	Santa Cruz Biotechnology	Cat# sc59171
F4/80 monoclonal antibody, APC	ThermoFisher Scientific	Cat# MF48005
Anti-mouse F4/80-Alexa Fluro 488	Invitrogen/eBioscience	Cat# 2126068
Goat polyclonal anti-EEA1	Santa Cruz Biotechnology	Cat# B1813, sc6415
Mouse monoclonal anti-Rab11	Santa Cruz Biotechnology	Cat# H0919, sc166912
Mouse monoclonal anti-Lamp1	Santa Cruz Biotechnology	Cat#F1609, sc18821
Rabbit polyclonal anti-CD68	Santa Cruz Biotechnology	Cat# sc9139
Anti-Actin, α-Smooth Muscle - Cy3™ antibody, Mouse monoclonal α-SMA	Sigma-Aldrich	Cat# C6198
Rat-anti Mouse CD31	BD Pharmingen	Cat# 550274
Goat monoclonal P-selectin	Santa Cruz Biotechnology	Cat# G1411, sc6943

Mouse monoclonal E-selectin	Santa Cruz Biotechnology	Cat# sc137054
Goat polyclonal ICAM-1	Santa Cruz Biotechnology	Cat# sc1511
Mouse monoclonal VCAM-1	Santa Cruz Biotechnology	Cat# sc13160
Alexa Fluor Conjugated Second Antibodies		
Goat anti-rabbit 647	Invitrogen	Cat# A-21244
Goat anti-rat 647	Invitrogen	Cat# A-21247
Donkey anti-mouse 594	Invitrogen	Cat# A-21203
Donkey anti-rabbit 594	Invitrogen	Cat# A-21207
Donkey anti-rat 594	Invitrogen	Cat# A-21209
Donkey anti-rat 488	Invitrogen	Cat# A-21208
Donkey anti-mouse 488	Invitrogen	Cat# A-21202
Donkey anti-rabbit 488	Invitrogen	Cat# A-21206
Biological Samples		
Atherosclerosis patient's arch samples	Maine Medical Center (MRC)BioBank, Maine	N/A
Normal population's arch samples	Maine Medical Center (MRC)BioBank, Maine	N/A
Mouse aortic roots and hearts	This study	N/A
Mouse serum	This study	N/A
Chemicals, Peptides, and Recombinant Proteins		
Oil Red O (ORO)	AMRESCO	Cat# 0684-100G
Hematoxylin and Eosin stain kit	Vector Laboratories	Cat# H-3502
Oxidized LDL (ox-LDL)	Athens Research and Technology	Cat#12-16-120412-ox
Acetylated LDL (Ac-LDL)	Invitrogen	Cat#2300941
Low Density Lipoprotein from Human Plasma, oxidized, DiI conjugate (DiI-OxLDL)	ThermoFisher Scientific	Cat# L34358
TopFluor Cholesterol	Avanti Polar Lipids,Inc	Cat# 810255p

MG132	Sigma-Aldrich	Cat# M7449
N-Ethylmaleimide (NEM)	Alfa Aesar	Cat# 40526
Brewer Thioglycollate Medium	Sigma-Aldrich	Cat#124k0115
Bodipy 493/503	Invitrogen	Cat# D3922
SlowFade mount with DAPI	Invitrogen	Cat# 1896320
M-CSF mouse	Prospec	Cat# cyt-439-b
Protein inhibitor cocktail	TargetMol	Cat# C0001
Phalloidin-iFluor 594 reagent	Abcam	Cat# ab176751
Liver x receptor agonist (LXR T0901317)	Apexbio Tech LLC	Cat#A2249
Mouse seroblock FCR	Bio-Rad	Cat# BuF041B
Phosphotungstic acid hydrate	ACROS	Cat#A0417659
[1,2-^{3}H]-Cholesterol	PerkinElmer	Cat# NET139001MC
Liquid scintillation fluid OPTI-Flour	PerkinElmer	Cat# 47-20081
Apoprotein A-I (ApoA1)	Sigma-Aldrich	Cat# A0722
High density lipoprotein (HDL)	Sigma-Aldrich	Cat# L8039
Hexane	ThermoFisher Scientific	Cat# 610070040
Isopropanol, molecular biology grade	ThermoFisher Scientific	Cat# T036181000CS
Cholesterol acyltransferase (ACAT) inhibitor	Sigma-Aldrich	Cat# S9318-5mg
Lipofectamine 2000 transfection reagent	Invitrogen	Cat#11668027
Lipofectamine LTX	Invitrogen	Cat# A12621
ImageiT™ signal enhancer	Invitrogen	Cat# 136933
Qiagen RNeasy Mini Kit	Qiagen	Cat# 74106
RNase-free DNAse 1	New England Biolabs	Cat# M0303S
SuperScript III First-Strand Synthesis SuperMix	ThermoFisher Scientific	Cat# 18080400
SYPR Green PCR Master Mix reagent	GeneCopoeia	Cat# QP001-01
Aqueous Mounting Medium	R & D Systems	Cat# CTS011

Protein A/G plus agarose	Santa Cruz Biotechnology	Cat# Sc-2003
EZ-Link Sulfo-NHS-LC-Biotin	ThermoFisher Scientific	Cat# 21335
Neutravidin Beads	ThermoFisher Scientific	Cat# 29200
S2P-peptide (CRTLTVRKC)	GLS Biochem Systems Inc	Cat# 625358
DSPE-PEG-Mal (MW, 3.4 kDa)	Nanocs Inc.	Cat# PG2-DSML-3k
Cationic ethylenediamine core-poly(amidoamine) (PAMAM) dendrimer generation 0 (G0)	Sigma-Aldrich	Cat# 412368
Ester-terminated PLGA	DURECT Corporation	Cat# B6013-2
Amaxa™ Mouse macrophage nucleofector kit	Lonza	Cat# VPA-1009
Recombinant DNA		
pcDNA	Kai Song et al, 2021	N/A
Flag-Epsin1^{WT}	Yunzhou Dong et al, 2020	N/A
Flag-Epsin1$^{\Delta UIM}$	Yunzhou Dong et al, 2020	N/A
Flag-Epsin1$^{\Delta ENTH}$	Yunzhou Dong et al, 2021	N/A
CD36-bio-His: CMV plasmid	Addgene	Cat# 52025
ABCG1-pCSdest: SP6 plasmid	Addgene	Cat# 53952
Commercial Assays		
BAC-protein concentration measurement kit	Thermo Fisher Scientific	Cat# 23225
SuperSignal™ West Pico Chemiluminescent Substrate	Thermo Fisher Scientific	Cat#: 34080
Experimental Models: Organisms/Strains		
ApoE$^{-/-}$ atherosclerosis mouse model	Jackson Laboratory	Cat# 008525
Epsin mutant mouse model	This study	N/A
LysM-Cre deleter mice	This study	Cat# 004781
ABCG1^{fl} mouse model	This study	Cat# 027954
Experimental Models: Cell Lines		

HEK-293T	ATCC	CRL-3216
Virus Strain		
rAAV8-D377Y-mPCSK9	Boston Children's Hospital Viral Core Facility	N/A
Deposited Data		
N/A		
Oligonucleotides		
Epsin1:	This study	N/A
Forward: 5'-CTACCAACGTCCATTGCGGT-3'		
Reverse: 5'-GCAGCGATGAGGTCGACATT-3'		
Epsin2:	This study	N/A
Forward: 5'-TCTATCAGACGGCAGATGAAAAAC-3'		
Reverse: 5'-GTCATTGGAGGTGGCCTCC-3'		
IL-6	This study	N/A
Forward: 5'-AGTCCGGAGAGGAGACTTCA-3'		
Reverse: 5'-TTCCACGATTTCCCAGAG-3'		
IL-1beta	This study	N/A
Forward: 5'-GAAGAAGAGCCCATCCTCTG-3'		
Reverse: 5'-TCATCTCGGAGCCTGTAGTG-3'		
TNF-alpha	This study	N/A
Forward: 5'-ATGAGAAGTTCCCAAATGGC-3'		
Reverse: 5'-CTCCACTTGGTGGTTTGCTA-3'		
MCP-1	This study	N/A
Forward: 5'-GAAGGAATGGGTCCAGACAT-3'		
Reverse: 5'-ACGGGTCAACTTCACATTCA-3'		
iNOS	This study	N/A
Forward: 5'-CCCTTCCGAAGTTTCTGGCAGC-3'		
Reverse: 5'-GGCTGTCAGAGCCTCGTGGCTTTGG-3'		
IL-10	This study	N/A
Forward: 5'-CCCAGAAATCAAGGAGCATT-3'		

Reverse:5'-TCACTCTTCACCTGCTCCAC-3'		
Arg1	This study	N/A
Forward: 5'-CAGTGGCTTTAACCTTGGCT-3' Reverse: 5'-GTCAGTCCCTGGCTTATGGT-3'		
ABCG1	This study	N/A
Forward: 5'-CCGATGTCCCCTTTCAGATCA-3' Reverse: 5'-AGCAGCGAACAGCACAAAAC-3'		
ABCA1	This study	N/A
Forward: 5'-GTGGGCTCCTCCCTGTTTTT-3' Reverse: 5'-TCTGAGAAACACTGTCCTCCTTTT-3'		
CD36	This study	N/A
Forward: 5'-GCTGTCAGGCGTCAGGATAA-3' Reverse: 5'-CACATTTCAGAAGGCAGCAACT-3'		
CCR7	This study	N/A
Forward: 5'- CATGGACCCAGGTGTGCTT-3' Reverse: 5'- CATGAGAGGCAGGAACCAGG-3'		
Netrin-1	This study	N/A
Forward: 5- GGAGGAACCGGAAGACTGTG-3' Reverse: 5- GTCCTCGGCATTACCCAACA-3'		
Sema 3a	This study	N/A
Forward: 5'- ACGCACCATGGCACCG-3' Reverse: 5'- GTGCTAGGCCAGTATATCTCTCTG-3'		
Beta-actin	This study	N/A
Forward: 5'- TTACTGCTCTGGCTCCTAGCA-3' Reverse: 5'-CCACCGATCCACACAGAGTAC-3'		
Mouse Epsin1 siRNA sequence	This study	N/A
GAACUGGAGGCACGUCUACAAUU		
Mouse Epsin2 siRNA sequence	This study	N/A
GCAGUGCCGUGAGAACAUCUUUU		
Mouse control luciferase siRNA sequence	This study	N/A

CUUACGCUGAGUACUUCGA dT dT		
Software and Algorithms		
Image J	NIH website: https://imagej.nih.gov/ij/	N/A
GraphPad Prism	GraphPad software company: https://www.graphpad.com/sci entific-software/prism/	N/A
BioRender	BioRender http://app.biorender.com	N/A
Zeiss Zen lite	https://www.zeiss.com/microscopy/us/products/microscope-software/zen-lite.html	N/A